Estimating Uncertainty in Multiple Fibre Reconstructions

Kiran Kumar Seunarine

A dissertation submitted in partial fulfillment
of the requirements for the degree of
Doctor of Philosophy
of
University College London.

Department of Computer Science
University College London

2011

I, Kiran Kumar Seunarine, confirm that the work presented in this thesis is my own. Where information has been derived from other sources, I confirm that this has been indicated in the thesis.

Abstract

Diffusion magnetic resonance imaging (MRI) is a technique that allows us to probe the microstructure of materials. The standard technique in diffusion MRI is diffusion tensor imaging (DTI). However, DTI can only model a single fibre orientation and fails in regions of complex microstructure. Multiple-fibre algorithms aim to overcome this limitation of DTI, but there remain many questions about which multiple-fibre algorithms are most promising and how best to exploit them in tractography.

This work focuses on exploring the potential of multiple-fibre reconstructions and preparing them for transfer to the clinical arena. We provide a standardised framework for comparing multiple-fibre algorithms and use it for a robust comparison of standard algorithms, such as persistent angular structure (PAS) MRI, spherical deconvolution (SD), maximum entropy SD (MESD), constrained SD (CSD) and QBall. An output of this framework is the parameter settings of the algorithms that maximise the consistency of reconstructions. We show that non-linear algorithms, and CSD in particular, provide the most consistent reconstructions.

Next, we investigate features of the reconstructions that can be exploited to improve tractography. We show that the peak shapes of multiple-fibre reconstructions can be used to predict anisotropy in the uncertainty of fibre-orientation estimates. We design an experiment that exploits this information in the probabilistic index of connectivity (PICo) tractography algorithm. We then compare PICo tractography results using information about peak shape and sharpness to estimate uncertainty with PICo results using only the peak sharpness to estimate uncertainty and show structured differences. The final contribution of this work is a robust algorithm for calibrating PICo that overcomes some of the limitations of the original algorithm. We finish with some early exploratory work that aims to estimate the distribution of fibre-orientations in a voxel using features of the reconstruction.

Acknowledgements

This thesis would not have been possible without the help and support of many people. First and foremost I would like to thank my supervisor, Professor Daniel Alexander. Not only did he give me the opportunity to undertake a PhD, first through admission to the MRes CVIPGS programme and then by taking me on as one of his PhD students, he provided a great deal of help and guidance throughout. Without his support I would not have been able to do this work. Words cannot express my gratitude to him.

I am grateful to the EPSRC for funding my studies and providing funds for attending conferences, both in the UK and abroad.

I would like to thank my friends at UCL, both past and present, for their encouragement and help. Not only were they happy to help with any problems I might be experiencing, they also reminded me that there is more to life than work. I am particularly grateful to Matt Hall for providing many hours of useful discussion on various aspects of diffusion MRI and proof-reading drafts of my thesis. I am also grateful to Phil Cook for his help, especially towards the beginning of my studies.

I would also like to thank my family for their love and support. My achievements are in no small part due to their encouragement. In particular I would like to thank my father Vishwanath, for his love, inspiration and unfaltering guidance, which encouraged me to aim for a career in research. Finally, I would like to thank Ai Wern Chung. She helped in so many ways, from reading drafts of my thesis to keeping me company while I was writing up.

Contents

List of Figures

List of Tables

Chapter 1

Introduction

Diffusion magnetic resonance imaging (MRI) is a powerful tool that allows us to probe the microstructure of materials, such as the fibrous white-matter of the brain, *in-vivo* by observing bulk dispersion of particles that are subject to Brownian motion. In medical diffusion MRI these particles are usually water molecules due to their abundance in biological tissue. On a molecular level, water molecules undergo random motion due to thermal fluctuations. If unhindered, the water molecules can diffuse freely in any direction. However, barriers placed into the path of the water molecules restrict the mobility of the molecules in the direction perpendicular to the barrier. For example, the white-matter of the brain consists of fibrous axons that connect different functional regions. Water molecules diffusing through this microstructure can move more freely in the direction of the fibres than across them. Voxels used in *in-vivo* human brain imaging are typically of the order of 2 mm cubed, which is several orders of magnitude larger than the size of the cells, so there are many barriers that can hinder diffusion within a voxel. We therefore observe the mass average dispersion pattern, although this still provides information about the nature of the underlying microstructure, such as the distribution of fibre orientations.

One major clinical application of diffusion MRI is stroke imaging [1, 2]. Regions affected by stroke appear hyperintense on diffusion-weighted images, which suggests a reduction in water mobility. The mechanisms for this reduction are unclear but a likely factor is cell swelling. When white-matter axons swell, the space between the axons reduces and the dispersion of water molecules becomes more hindered. The subtle changes to microstructure that can be observed by diffusion MRI occur before the changes that can be seen on structural images. This allows clinicians to determine the full extent of the affected regions soon after the stroke occurs and leads to an improved management and treatment of the stroke.

The standard method of diffusion MRI is diffusion tensor imaging (DTI), introduced by Basser et al [3] in 1994. DTI represents the dispersion of water through diffusion using a simple model known as the diffusion tensor. This model assumes zero-mean trivariate Gaussian displacements. The diffusion tensor provides us with several useful pieces of information. Firstly, the diffusion tensor offers scalar indices, such as mean diffusivity (MD) and fractional anisotropy (FA), which are commonly used as measures of white-matter integrity. MD measures the overall dispersion of water molecules regardless of any orientational preference; FA describes the degree of directionality of diffusion (i.e. how much the degree of dispersion depends on direction). Damage to tissue microstructure removes some barriers to diffusion, which allows water molecules to disperse more freely. This results in an increase in MD and decrease in FA. For example, Klingberg et al [4] show the FA to correlate positively with reading performance in brain regions associated with reading for both healthy and dyslexic adults. In [5], Douaud et al show differences in white-matter microstructure between patients with Huntington's disease and normal controls using DTI.

Another useful piece of information recovered by DTI is an estimate of the local orientation in white-matter from the direction of greatest dispersion. White-matter pathways are often several centimetres in length so stretch over many voxels. By following local fibre-orientation estimates from voxel to voxel through an image, tractography algorithms recover the global paths of white-matter tracts through the brain. One major application of tractography is anatomical connectivity mapping. In [6], Draganski et al use tractography to investigate the connectivity of the cortico-basal ganglia circuits. The technique also has several clinical applications, including neurosurgical planning [7] and evaluation [8]. In neurosurgical planning tractography can be used to determine the location of important white-matter pathways, such as those involved in motor function, that are close to an area being resected so that these tracts can be spared. Tractography is also used post-surgery to investigate whether white-matter pathways have been preserved or any reorganisation of functional connections has occurred.

The main limitation of DTI is that it can only recover a single fibre orientation in each voxel. A typical image voxel is several orders of magnitude larger than the size of the white-matter axons being imaged. Therefore, many voxels contain contributions from several fibre populations. The diffusion tensor model often fails in these situations and tractography breaks down, missing connections or even suggesting spurious ones. This has resulted in a new class of methods that aim to recover all fibre orientations in the voxel. These are known as multiple-fibre reconstruction algorithms. Various studies [9, 10] have shown that these methods improve tractography in regions where crossing-fibre configurations are encountered.

Tractography has a great deal of potential to improve clinical outcomes. However, there remain some significant issues that limit its use in practise. Regions of complex microstructure can lead to incomplete segmentations or even an inability to recover tracts. For example, in cases where the temporal lobe is resected, such as surgical treatment of temporal-lobe epilepsy [11], the optic radiation must be avoided, since damage to this pathway can lead to permenent visual defects [12]. The optic radiation is not distinct from other white-matter in structural scans and therefore tractography of this structure can be of great benefit to the surgeon. However, tractography of the optic radiations is problematic around the anterior portion of Meyer's loop [13, 14]. The fibre pathway curves sharply at this point which, when combined with limited spatial resolution and noise in the data, may lead to poor segmentations. Several other tracts also intersect near this point, leading to a complex crossing arrangement that further complicates the problem. Therefore, the single fibre-orientation estimate provided by the diffusion tensor will be insufficient to track accurately through this region. Multiple-fibre algorithms can capture more of the complexity of this structure, which in turn will potentially lead to improved tractography results.

1.1 Problem statement

Multiple-fibre reconstruction algorithms offer a great deal of useful information about diffusion in voxels containing complex fibre configurations. However, questions about how best to interpret and exploit this information must be answered before the methods can be transferred to the clinical environment. Although multiple-fibre methods have been used in tractography, it is still unclear how best to integrate them fully. Fibre-orientation estimates are just one piece of information that can be extracted using these methods; other information may improve the ability of tractography to navigate through complex microstructure. In addition to this, the information recovered can be used to develop indices that may potentially be more sensitive to changes in microstructure than those from DTI.

The goals of this work are to determine which multiple-fibre reconstruction algorithms provide the most useful information about the microstructure and to adapt tractography to utilise this information. In this work we do not develop new multiple-fibre algorithms. Instead, we investigate methods for exploiting more of the information recovered by exisiting techniques.

1.2 Contributions

This work makes the following contributions:

- a taxonomy of multiple-fibre reconstruction algorithms.
- a rigorous comparison of different multiple-fibre reconstruction algorithms.
- a standardised framework for comparing multiple-fibre algorithms. This framework is based on the procedure for optimising algorithms used by [15].
- a new and faster implementation of the persistent angular structure MRI (PASMRI) multiple-fibre reconstruction algorithm, using the spherical deconvolution filter defined in [16].
- a method for exploiting the peak shapes of multiple-fibre reconstructions to provide information about anisotropy in uncertainty.
- We integrate the method for exploiting peak shapes into the probabilistic index of connectivity (PICo) tractography algorithm that is implemented the Camino toolkit.
- a robust calibration algorithm for creating a mapping between uncertainty and peak shape.
- early exploratory work on modelling the true distribution of fibre-orientations in each voxel. Specifically, we use the sub-voxel model of Gilani et al [17] to predict the true fibre-distribution from the reconstruction.

1.3 Thesis Overview

Chapter 2 introduces the principles behind diffusion MRI along with an overview of a basic diffusion-weighted MRI sequence. We then describe diffusion tensor imaging. Finally, we describe both deterministic tractography and probabilistic tractography algorithms.

In chapter 3, we outline the current state-of-the-art multiple-fibre reconstruction techniques. We introduce the multiple-fibre problem and describe the main multiple-fibre reconstruction algorithms as well as methods used to regularise these methods. We go on to outline some of the comparisons that have been performed. Finally, we describe how the tractography algorithms discussed in chapter 2 have been extended to exploit multiple-fibre reconstructions. This chapter appears in "Diffusion MRI: from quantitative measurement to in vivo neuroanatomy", edited by H. Johansen-Berg and T. E. J. Behrens [18].

The first algorithmic contribution of this work is detailed in chapter 4, where we compare some of the multi-fibre reconstruction algorithms. Multi-fibre reconstruction algorithms can be categorised into two groups: linear and non-linear. Linear methods involve a simple matrix multiplication; non-linear methods use a non-linear optimisation procedure such as the Levenberg-Marquardt algorithm. Non-linear methods, such as PAS-MRI [15, 16] offer a potential improvement in terms of the precision of fibre-orientation estimation, but are very computationally expensive. In comparison, the linear reconstruction methods are computationally inexpensive and can be used on a standard desktop. These methods have yet to be compared to each other using a single framework. We perform a comparison of the main linear multi-fibre reconstruction algorithms, as well as a few of the non-linear algorithms, described in chapter 3. We synthesise crossing-fibre data with a range of angles between the fibre populations, which allows us to calculate the accuracy and precision of all of the methods. The framework also finds the settings of the parameters for each method that maximises the consistency of the fibre-orientation estimates. Part of this work is in Proc. ISMRM [19].

Chapter 5 provides the second major contribution of this thesis. In this chapter we hypothesise that the functions output by multiple-fibre reconstructions contain much more information about the true fibre orientations than just the peak orientations. We show that the shape of the peaks reflect the local spread of fibres and, in particular, that the peak anisotropy (i.e. how elliptical the peak cross section is) reflects local fibre bending or fanning. We go on to construct a new general framework for PICo with multiple-fibre reconstructions, extending Parker and Alexander's method [10], that exploits the information encoded in the peak shape. Specifically, we develop a calibration procedure that provides a mapping between peak shape and uncertainty that can be used with the Camino implementation of PICo. Specifically, we develop a calibration procedure that provides a mapping between peak shape and uncertainty that can be used with the Camino implementation of PICo. The aim of this work is not to develop a method for resolving fibre-crossings, rather we attempt to exploit the information recovered by existing algorithms to improve tractography. The technique described here is published in the Proc. MMBIA [20].

The third major contribution of this work will be introduced in Chapter 6. We provide a more robust calibration procedure for exploiting the peak anisotropy from multiple-fibre reconstructions. The algorithm presented overcomes some limitations of the procedure described in chapter 5. Finally, we show some proof-of-concept work on predicting the true distribution of fibre-orientations using features of a reconstruction. The proof-of-concept section of this chapter is in Proc. ISMRM [21].

Chapter 7 concludes this work with a discussion and details of future work.

Chapter 2

Magnetic Resonance Imaging (MRI) and diffusion MRI

This chapter provides a general overview of some of the basic principles of MRI and in particular diffusion MRI. We start by introducing the concept of a spin and how they produce a signal that can be measured. From there, we show how to sensitize MRI to diffusion of water molecules. We finish by introducing Diffusion Tensor Imaging (DTI), which is the standard method for modelling diffusion, along with some useful scalar indices derived from it.

2.1 An overview of MRI

MRI is based on the principles of nuclear magnetic resonance of nuclei. That is, we manipulate the proton ‘spins’ to form images. This is necessarily a quantum mechanical process, but because we observe this on the macro scale some classical ideas are useful. It is important to remember that ‘spin’ is a quantum mechanical concept. Nucleons do not literally spin in the classical sense but they do possess angular momentum and therefore behave as if they are spinning. In medical MRI, the atom of interest is usually the hydrogen atom due the abundance of water in the body. The nucleus of a hydrogen atom has a single positively-charged proton. This combination of angular momentum and charge results in the nucleus having a local magnetic field with dipolar geometry. The axis of the dipolar field (called the moment of the spin) is normally randomly oriented (see figure 2.1a). However, as with any magnet, the spins attempt to align themselves with any external magnetic field. In MRI, a powerful magnetic field is provided by a superconducting magnet and is known as the B_0 field.

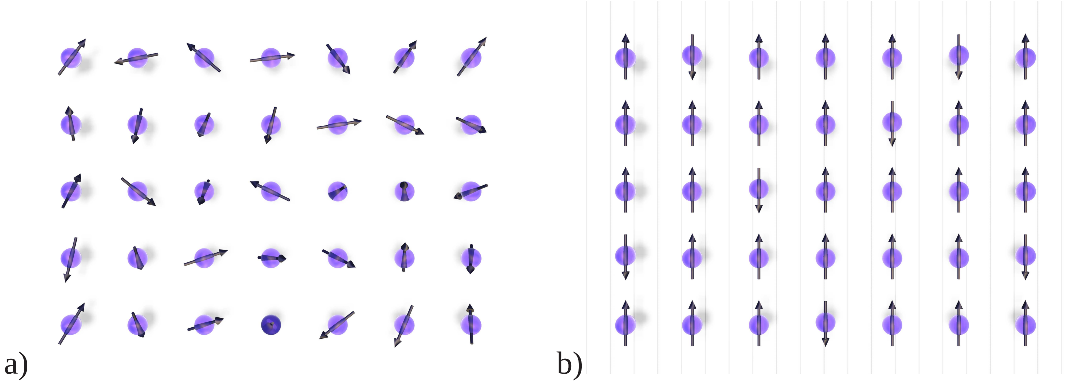

Figure 2.1: A group of spins a) before and b) after a magnetic field is applied.

Unlike conventional magnets, spins may align themselves either with or against the external magnetic field depending on the energy level they are in (figure 2.1b). Elements with an odd atomic number have several energy levels [22]. In the case of a hydrogen nucleus there are two energy levels: a low energy level parallel to the applied field and a high energy level anti-parallel to it. Spins constantly interchange between these two states, but the ensemble average in each state remains constant. The number of spins in each state is given by Boltzmann's equation:

$$N^{+}/N^{-} = \exp^{-\Delta E/kT} \tag{2.1}$$

where N^{+} and N^{-} are the number of spins in the high and low energy states respectively, ΔE is the energy separation of the states, $k = 1.38\times10^{-23} J/K$ is the Boltzmann constant and T is the temperature. At room temperature, there are about 5% more spins in the low energy state than the high energy state. This differential results in a slight magnetic field, which we call the magnetisation vector $\mathbf{M}_0$.

When the nucleus is exposed to $\mathbf{B}_0$, it experiences precession. If the spin axis is not aligned with the applied field, the spin axis will precess around it. An illustration of a spin precessing is shown in figure 2.2. The angular frequency ω of precession is given by the Larmor equation,

$$\omega = \gamma \mathbf{B}_0, \tag{2.2}$$

where γ is the gyromagnetic ratio, a value that is unique for every nucleus type. Note that the frequency of precession is dependent on both the strength of the magnetic field and the nucleus being observed.

While the spins are aligned with the $\mathbf{B}_0$ field no signal is observed. Energy is

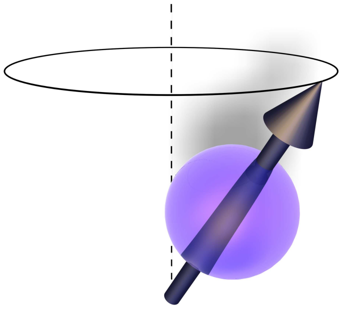

Figure 2.2: A precessing spin. The dotted line shows the $\mathbf{B}_0$ field and the solid circle plots the path of precession.

introduced to the spins using an radio frequency (RF) pulse. The RF pulse is an oscillating magnetic field called the $\mathbf{B}_1$ field. The frequency of RF required to excite a nucleus is the same as the precession frequency of the nucleus given by eqn 2.1. As energy is introduced, the magnetization vector, $\mathbf{M}_0$, is pushed towards the transverse plane. This is illustrated in figure 2.3. The left panel shows the path of $\mathbf{M}_0$ from a fixed frame of reference, called the laboratory frame of reference. The motion is often simplified (see right panel) by describing the motion relative to a reference point that is rotating at the same frequency as the spin precession. The duration and strength of the RF pulse affects the flip angle of the $\mathbf{M}_0$. Specifically, the flip angle α_f is defined as

$$\alpha_f = \gamma \mathbf{B}_1 t_p, \tag{2.3}$$

where t_p is the duration of the RF pulse. The flip angle, α_f, can be controlled by changing either the strength of the RF or the duration of its application. When the $\mathbf{M}_0$ is flipped towards the transverse plane a signal can be observed. This signal will be at the same frequency as the spin precession. In a simple acquisition a 90° pulse is applied, which flips $\mathbf{M}_0$ into the transverse plane.

As soon as the $\mathbf{B}_1$ is removed, the nuclei gradually relax back to their resting state and the signal attenuates. This is known as the free-induction decay (FID). Figure 2.4 illustrates a FID. There are several mechanisms that result in the loss of signal. The first is T1 (longitudinal; spin-lattice) relaxation. As the spins lose energy they return to their

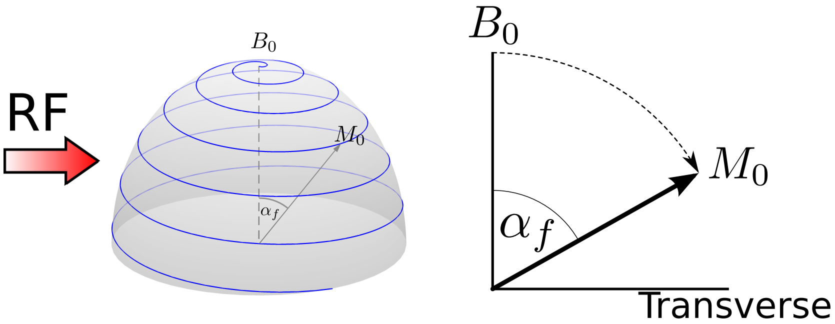

Figure 2.3: Path of the magnetization vector, M_0, as RF is applied in (left) laboratory frame and (right) rotating frame.

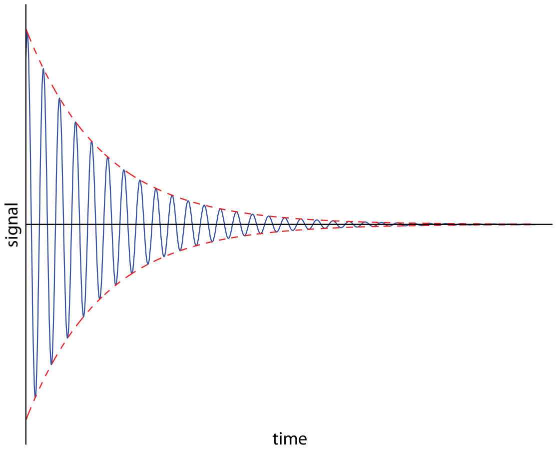

Figure 2.4: Free induction decay (FID) of signal after the application of the RF is removed.

resting state and the magnitude of the z-component of M_0 increases. The other is T2 (transverse; spin-spin) relaxation, which occurs when the phase of a spin is affected by other spins within a local area. This results in a dephasing of the spins which reduces the transverse magnitude of M_0.

The scanner is unable to make use of the FID, since much of the signal has been lost by the time it is being read by the receiver coils. Instead, we observe an echo of the net magnetisation. For example, a spin echo occurs when out of phase spins are brought back into phase. As mentioned above, T2 relaxation occurs due to spin-spin relaxation. However, in practise, the signal decay due to T2 effects is faster than expected. This is due to inhomogeneities in the B_0 field. Although we are unable to do anything about the random dephasing due to T2 decay, we are able to correct for field inhomogeneities

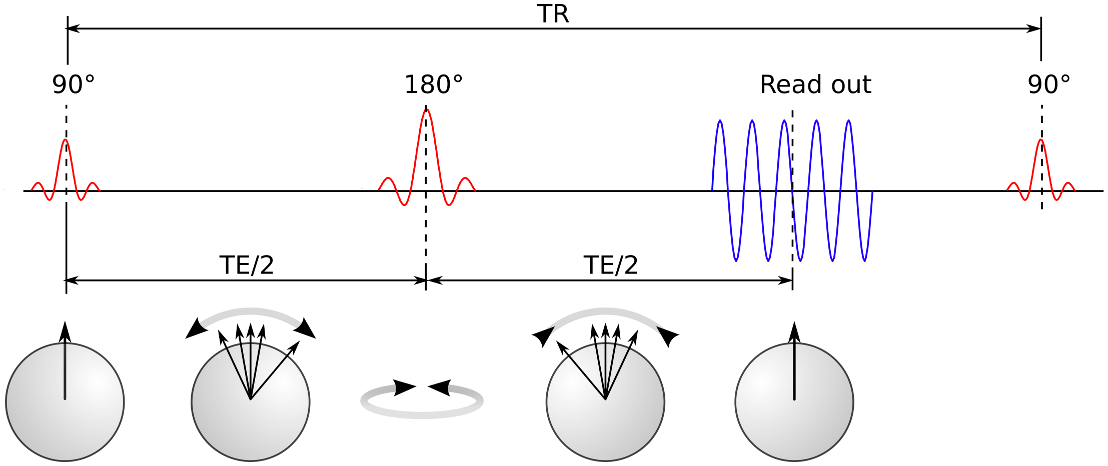

Figure 2.5: Illustration of a spin-echo pulse sequence. After the $90°$ pulse, the spins are initially in phase but begin to dephase over time. The $180°$ pulse reverses the phase of the spins. The spins continue to dephase in the same direction, which brings them back into phase. This forms an echo, after which the spins start to dephase again.

by applying another RF pulse that brings the spins back into phase, resulting in a spin-echo. Figure 2.5 illustrates a basic spin-echo sequence. In this sequence, the $90°$ pulse is applied as usual and the spins are allowed to dephase. After some time, TE/2, a $180°$ pulse is applied. This pulse reverses the phase of the spins, although they continue to dephase in the same direction. The spins then start to come back into phase until they form an echo at the timepoint TE, before dephasing again. We measure the signal at the echo.

In order to obtain an image it is necessary to determine the spatial location of the spins providing the signal. This is achieved by applying magnetic gradients (i.e. by varying the stength of the magnetic field spatially). These gradients are used to alter the phase and frequency of the spins depending on their precise location within the scanner and hence encode the spatial location in the signals. The final step in image formation is to convert the frequency and phase information to a spatial image via a Fourier transform [23].

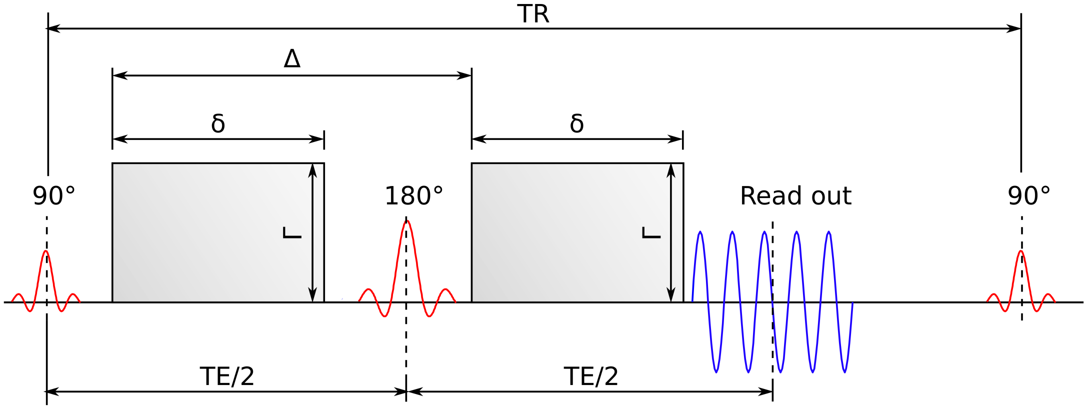

Figure 2.6: Illustration of pulsed-gradient spin-echo sequence [24]. Diffusion-weighting gradients (grey blocks) are inserted either side of the $180°$ pulse of the spin-echo sequence to sensitise the protocol to diffusion processes.

2.2 Diffusion-weighted Imaging and the Reconstruction Problem

In the previous section we introduced the spin-echo imaging scheme. This scheme can be extended to capture information about the diffusion of water molecules by applying a diffusion-weighted field gradient either side of the $180°$ pulse. These gradients are separate to those used in image formation. Figure 2.6 illustrates the diffusion-weighted pulse sequence, known as the pulsed-gradient spin-echo sequence (PGSE) [24]. The amount of diffusion weighting is controlled by varying the gradient strength Γ, duration δ, orientation, and the time between the onsets of the two gradient pulses Δ. The direction in space in which the magnetic field strength of this gradient changes is referred to as the “gradient direction”.

Figure 2.7 illustrates how spins are affected by the diffusion-weighted gradients. In this sequence, the first diffusion-weighted gradient alters the phase of the spins along the gradient direction. The second diffusion-weighted gradient is after the $180°$ pulse and effectively applies the opposite phase encoding to the first gradient. If the spins do not diffuse to a different position along the gradient direction during the interval between the diffusion weighted blocks (second row), the second gradient will cancel out the effects of the first gradient and restore the spins to their original phase; the signal will be exactly the same as a T2-weighted signal. However, if the spins move

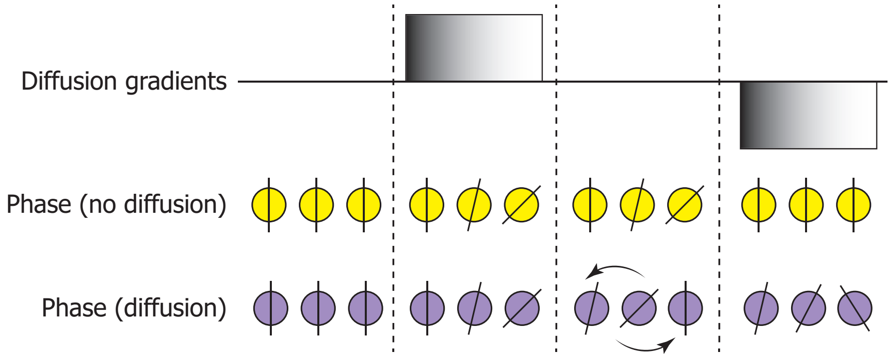

Figure 2.7: Illustration showing how magnetic gradients capture diffusion. The top row shows the gradients. The second row shows the effect of the diffusion gradients on the phase of static spins and the third row shows their effect on the phase of diffusing spins. Each column shows a single time point.

to a different position in the gradient (third row), the spins will not be brought back into phase and signal will be attenuated because the net magnetization is reduced. It is worth noting that we do not observe the diffusion of individual spins. Instead, we observe the average diffusion properties of the mass ensemble of the spins within an image voxel.

2.2.1 Diffusion and the Apparent Diffusion Coefficient (ADC)

Einstein [25] showed that, given a sufficiently large number of freely diffusing particles, the distribution of the particle displacements in a given time will be Gaussian. Since the displacements of freely diffusing particles are directly proportional to the diffusion time, a constant of diffusivity (known as the diffusion coefficient) can be calculated. In diffusion MRI, we can estimate the diffusion coeffient of freely diffusing particles from observations of the displacement over a given time.

When diffusion is observed in a sample however, the microstructure of biological tissue provides many barriers to diffusion, so the water molecules do not experience free diffusion. Estimates of the diffusion coefficient will be affected by this underlying microstructure. Specifically, the diffusion coefficient of water in tissue will appear lower than that of freely diffusing water. This lower coefficient is referred to as the apparent diffusion coefficient (ADC) [26]. The ADC provides useful information about the underlying microstructure.

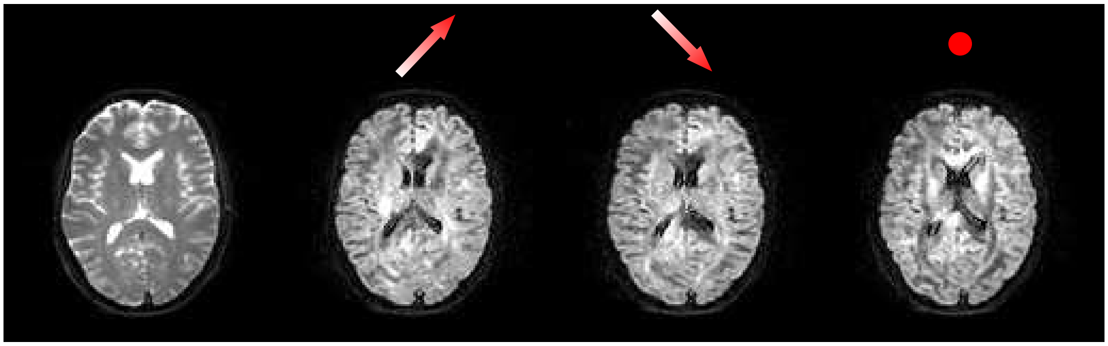

Figure 2.8: Examples of unweighted $A^{\star}(0)$ image (left) and diffusion-weighted images for a single slice of human brain data. The arrow above each diffusion-weighted image indicates the direction of the gradient.

The ADC is measured in a single direction. When the microstructure has no preferential direction over the space of an image voxel, the probability of a water molecule displacing a given amount is the same in every direction; the scatter pattern of water molecules is isotropic. In this case, the value of the ADC will be the same in every direction. However, if the microstructure being imaged is directionally dependent, the value of the ADC will change depending on the gradient direction. For example, the scatter pattern of water molecules in white-matter will be anisotropic and reflect the underlying orientation of the white-matter. The directional dependence of the ADC can be removed by averaging the measure over three orthogonal directions.

2.2.2 The Reconstruction Problem

In the previous section, we discussed how microstructure affects diffusivity. In this section we provide a bit more detail and outline the reconstruction problem. The displacement of particles in 3D is called the scatter pattern, p. The features of p provide a rich source of information about the underlying microstructure, such as the orientation of white-matter fibres. One of the main technical goals of diffusion MRI, referred to as the reconstruction problem, is to recover the scatter pattern of diffusing water from a set of measurements $A(\mathbf{q}_i)$, $i = 1, ..., N$. Figure 2.8 shows examples of images with different diffusion gradient directions for a single slice of human brain data. There are clear difference between the images and we can see structured regions where white-matter is oriented in the same direction as the gradients. These regions are shown as dark grey areas on the images. An unweighted image is provided on the left for comparison.

One simple model (the $\mathbf{q}$-space model) of the relationship between the measured signal and the scatter pattern is

$$A(\mathbf{q}) = (A^\star(\mathbf{0})^{-1} A^\star(\mathbf{q})) = \int_{\mathbb{R}^3} p(\mathbf{x}) \cos(\mathbf{q} \cdot \mathbf{x}) \mathrm{d}\mathbf{x}, \qquad (2.4)$$

where $\mathbf{q}$ is a *wavevector* in q-space, $A^\star(\mathbf{q})$ is a measurement prior to normalisation, $A^\star(\mathbf{0})$ is a measurement at $\mathbf{q} = 0$ for normalisation, and $A(\mathbf{q})$ is the normalised measurement. For a derivation of equation 2.4 see [27]. The wavevector depends on the length, strength and orientation of the gradient pulses during the measurement sequence and the diffusion time t on the pulse length and separation. For pulsed-gradient spin-echo measurements, for example, $\mathbf{q} = \gamma\delta\Gamma$ and $t = \Delta - \frac{\delta}{3}$. Often we separate $\mathbf{q}$ into a scalar wavenumber $|\mathbf{q}|$ and a diffusion encoding direction $\hat{\mathbf{q}} = \mathbf{q}/|\mathbf{q}|$, which is the direction of the magnetic field gradient in the diffusion-weighted pulses. The b-value summarizes both diffusion time and wavenumber $b = t|\mathbf{q}|^2$. The $\mathbf{q}$-space model in equation 2.4 assumes the displacements of diffusing particles is negligible during the application of the diffusion gradients compared with their displacements during the time between gradient onsets, i.e. $\delta << \Delta$. Often that assumption is violated in practice although the $\mathbf{q}$-space model still provides a useful approximation. Other models, such as the Gaussian Phase Distribution [28] or Callaghan's matrix method [29] provide more accurate but complex approximations.

2.3 Diffusion Tensor Imaging

Diffusion Tensor Imaging [3] assumes that the scatter pattern, p, is a zero mean trivariate Gaussian distribution, i.e.

$$p(\mathbf{x}) = ((4\pi t)^3 \det(\mathbf{D}))^{-\frac{1}{2}} \exp\left(\frac{\mathbf{x}^T \mathbf{D}^{-1} \mathbf{x}}{4t}\right), \qquad (2.5)$$

where $\mathbf{D}$ is the diffusion tensor and t is the diffusion time. Substituting (2.5) into (2.4) gives

$$A(\mathbf{q}) = \exp(-t\mathbf{q}^T \mathbf{D} \mathbf{q}). \qquad (2.6)$$

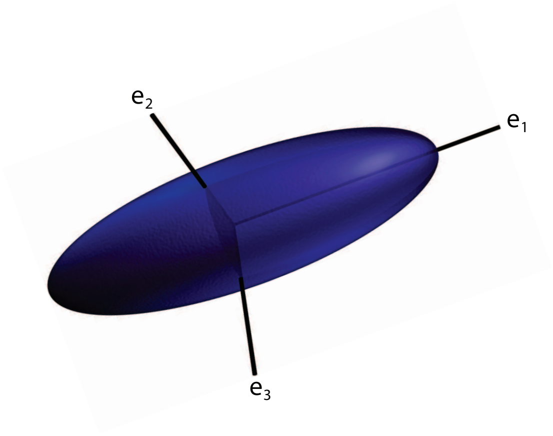

Figure 2.9: Illustration of a diffusion tensor ellipsoid including its three eigenvectors.

The diffusion tensor, $\mathbf{D}$, is a symmetric 3×3 matrix. It has six free parameters which are estimated using a minimum of six normalised measurements, $A(\mathbf{q})$. Thus, DTI requires at least seven $A^{\star}(\mathbf{q})$ including an unweighted (T2) measurement, $A^{\star}(0)$, for normalisation. Figure 2.9 shows an illustration of a tensor represented as a diffusion ellipsoid. The principal eigenvector of the tensor, $\mathbf{e}_1$ provides us with an estimate of the dominant fibre orientation, which we use in tractography. The eigenvalues, λ_1, λ_2 and λ_3, of the tensor provide useful information about the shape of the tensor which are used to calculate various scalar measures (see section 2.3.1, below).

The shape of the diffusion tensor depends on the underlying microstructure. Figure 2.10 shows diffusion tensor ellipsoids for a slice of human brain data. In white-matter bundles, the tensor elongated in the direction of the white-matter (figure 2.10, top left). In regions of grey matter and CSF there is no preferred orientation so the diffusion tensor is approximately isotropic (middle), although the eigenvalues of the tensor will be larger in CSF, which reflects increased diffusivity in free-water compared to dense tissue. Finally, the tensor cannot model multiple fibre orientations, so in regions containing two fibre populations the ellipsoid takes on an oblate shape (bottom).

2.3.1 Scalar Indices

Several statistics are commonly obtained from the diffusion tensor. The two most common measures are mean diffusivity (MD) and fractional anisotropy (FA). Mean diffusivity is a measure of the overall amount of diffusion in a voxel, i.e.

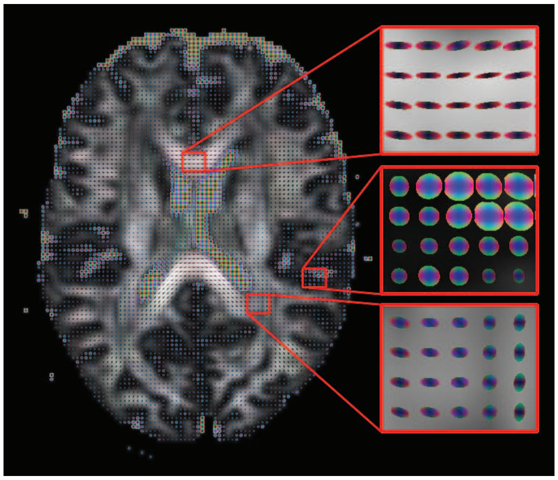

Figure 2.10: Example of DTI for a slice of brain data. The glyphs showing the shape of the tensor are overlaid onto a fractional anisotropy map (see section 2.3.1).

$$\bar{\lambda} = \frac{Tr(\mathbf{D})}{3}. \tag{2.7}$$

Figure 2.11a shows an example of an MD image. In this image, dark regions are areas where there is low diffusivity; light regions indicate high diffusivity. Diffusion is restricted in both grey- and white-matter, so both of these tissues are displayed as grey regions and there is little contrast. Diffusion in cerebral-spinal fluid (CSF) is far less restricted and therefore displayed as white regions.

The fractional anisotropy (FA) of the diffusion tensor describes how much it deviates from a sphere. Specifically, it is the normalised standard deviation of the eigenvectors of $\mathbf{D}$,

$$\mathrm{FA} = \left(\frac{3}{2}\sum_{i=1}^{3}(\lambda_i - \bar{\lambda})^2\right)^{1/2} \left(\sum_{i=1}^{3}\lambda_i^2\right)^{-1/2} \tag{2.8}$$

In regions of deep white-matter, where the diffusion of water molecules is restricted by the microstructure of the axons, we expect very sharp diffusion tensors which have a high FA. Conversely, in grey-matter and cerebral spinal fluid (CSF), where there is no microstructure, or it has no preferential direction on the scale of an image voxel, we expect spherical tensors and a low FA. Figure 2.11b shows an example FA image. The light areas of the image are areas of high anisotropy (i.e. fibrous white-matter) and dark areas are areas of low anisotropy (such as grey matter). Directional

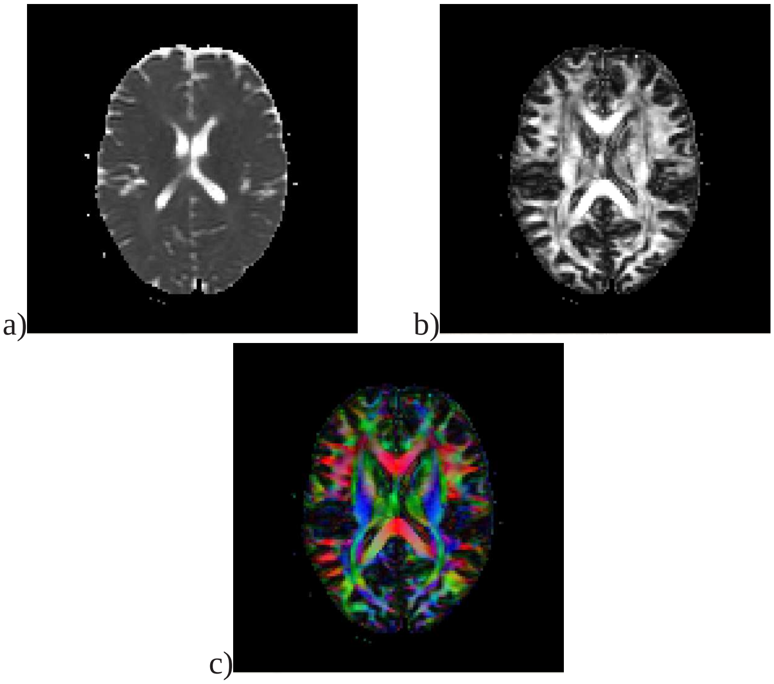

Figure 2.11: a) Mean Diffusivity, b) Fractional Anisotropy and c) color coded Fractional Anisotropy (red=left/right, green=anterior/posterior, blue=superior/inferior) images from a DTI reconstruction of human brain data.

information can be shown by colour coding the image; one approach is to multiply the FA with the absolute value of the principal eigenvector of $\mathbf{D}$ to get the RGB components of the pixel [30]. The result of colour coding the FA image is shown in figure 2.11c. In this image, red shows left-right diffusion; green shows anterior-posterior diffusion and blue shows superior-inferior diffusion.

2.3.2 Fitting

A standard approach for calculating the diffusion tensor is to fit to the log measurements using a least squares fit. Taking the log of the measurements yields a linear relationship, i.e.

$$\log(A) = -b\mathbf{D}. \tag{2.9}$$

However, better results can be obtained by fitting directly to the measurements (e.g. [31]) since the error distribution will be closer to normal than for the log fit. In addition, constraints can be placed on the diffusion tensor when fitting directly to $A(\mathbf{q})$ to improve the stability of the fitting procedure. For example, the tensor can be made

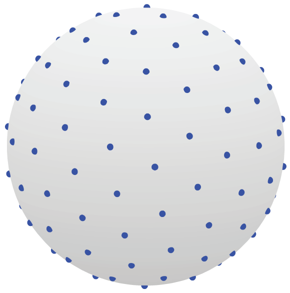

Figure 2.12: Illustration of a spherical acquisition sampling of $\mathbf{q}$-space.

cylindrically symmetric ($\lambda_1 = \lambda_2$ or $\lambda_2 = \lambda_3$) by setting $\mathbf{D} = v\mathbf{e}\mathbf{e}^T + B\mathbf{I}$ [32], where $\mathbf{e}$ is the principal eigenvector of the diffusion tensor and $\mathbf{I}$ is the identity tensor.

2.3.3 Acquisition Requirements

Although it is possible to calculate the diffusion tensor from just seven measurements, in practise many more are often used to reduce the effects of noise. The standard approach is to make N measurements with non-zero wavenumbers $\mathbf{q}_i$, $i = 1, ..., N$. The gradient directions $\hat{\mathbf{q}}_i$ are unique and distributed uniformly over the surface of a sphere (see figure 2.12). In addition to this, a further M measurements are made with $\mathbf{q} = \mathbf{0}$. This type of acquisition scheme is known as a “spherical acquisition scheme” [33] since the $\mathbf{q}_i$ all lie on a sphere in $\mathbf{q}$-space. It is worth noting that the length scales measured can be adjusted by altering the radius of the sphere on which $\mathbf{q}_i$ lie. Thus, the results depend on the radius of the sphere. This is true for all the methods that use the spherical sampling scheme. Although spherical acquisition schemes are the most common, the $\mathbf{q}_i$ do not need to be distributed on the surface of a sphere. It is possible that another acquisition scheme may improve the results of all the reconstruction algorithms.

2.3.4 Limitations

The Gaussian model used by DTI can only model a single fibre orientation. In many voxels, the signal departs from this Gaussian assumption. For example, many voxels contain signal contributions from several fibre populations. Since the diffusion tensor can only model one peak, DTI provides limited and potentially misleading information in these voxels. We describe this problem in more detail in the following chapter.

2.4 Tractography

Tractography uses information about the orientations of the fibre populations present in each voxel to estimate the paths of fibre bundles through the brain. Figure 2.13 shows paths (also called streamlines) generated using tractography to visualise the cortico-spinal tracts of a brain. There are several applications for tractography. First, tractography can be used to determine the connectivity of the brain [34, 35]. The information about the paths of the white matter bundles can also be used in neurosurgical planning [7] and to assess the impact that surgery has on white matter tracts [8]. For example, tumours can displace white-matter pathways by several centimetres. It is necessary to determine the new locations of these pathways prior to surgery to avoid damage to these structures. In terms of evaluation, the degree to which specific white-matter tracts have been spared and white-matter reorganisation can be investigated, as well as their effect on clinical scores.

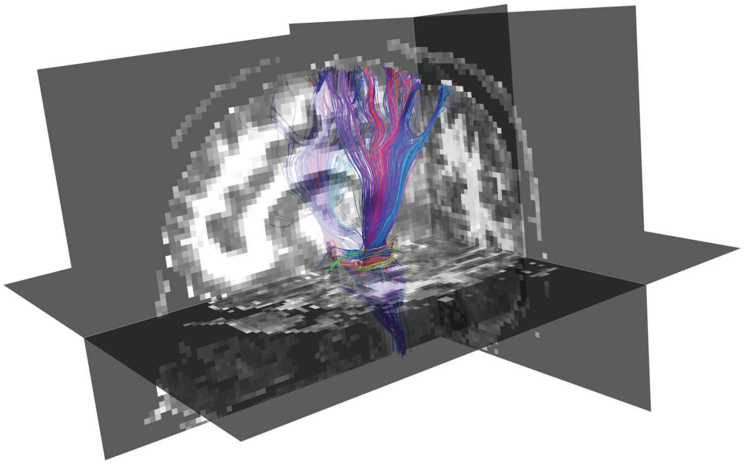

Figure 2.13: An example of tractography.

There are two types of tractography algorithm, deterministic and probabilistic. We describe both types in the following sections.

2.4.1 Deterministic Tractography

Deterministic tractography uses estimates of fibre-orientations in each voxel (such as the principal eigenvector of the diffusion tensor) to propagate a path through the brain. The path starts at a seed point and then propagates from point to point until some termination condition is satisfied. Figure 2.14 illustrates the process. Paths estimated using deterministic tractography are binary; two points are either connected or not connected. Also, the streamlines generated using this method can be erratic. Several factors cause this, including noise and patient motion [36]. In some deterministic tractography algorithms, the fibre-orientation estimates are interpolated to ensure that the streamlines are smooth, for example [37]. Some algorithms attempt to improve results by imposing constraints such as limiting the curvature of the path.

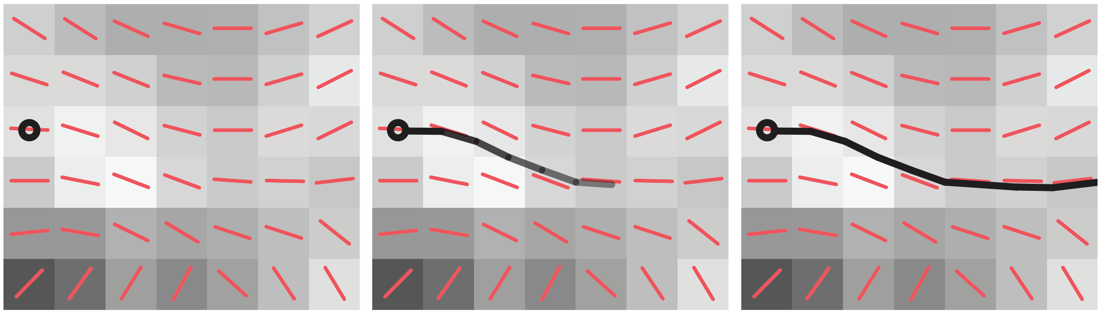

Figure 2.14: Illustration of basic streamline tractography. The seedpoint is indicated by the circle.

Mori et al [38] describe the FACT algorithm, which is an extension to the streamline approach. Here, they adjust the step size depending upon the continuity of the local fibre-orientation estimates. Where adjacent fibres are well-aligned a large step is taken; when there is no continuity between adjacent fibre-orientation estimates a small step is taken. This variable step size attempts to prevent the streamline from deviating from the true trajectory of the white-matter, for example at points of high curvature or when the streamline is close to a boundary.

More recently, Weinstein et al [39] have introduced the Tensor Deflection (TEND) tractography algorithm. This algorithm uses the entire diffusion tensor to calculate the appropriate deflection, as opposed to just the principal eigenvector. Therefore, this method uses the diffusion tensor as the true PDF of the underlying fibre distributions. In voxels where the anisotropy is high, the streamline follows the principal eigenvector of the diffusion tensor. However, as the diffusion tensor becomes more isotropic, the path of the streamline is deflected less.

2.4.2 Probabilistic Tractography

The main limitations of all deterministic tractography algorithms are that they do not account for uncertainty in the fibre-orientation estimates and are also unable to recover some complex structures such as fannings. These limitations have lead to the development of probabilistic algorithms. Probabilistic tractography [40, 41, 42] uses models of uncertainty in fibre-orientation estimates, along with standard streamline tractography, to calculate the probability of voxels being connected to a seed voxel. The procedure runs N streamline tracking processes from each seed point. For each streamline, each fibre-orientation estimate is randomly sampled from a probability density function (PDF) that models the distribution of fibre orientations in each voxel. The index of connectivity $\Phi(\mathbf{v})$ is then

$$\Phi(\mathbf{v}) = \lim_{N \to \infty} \Phi(\mathbf{v}, N) \approx \frac{\mu(\mathbf{v}, N)}{N}, \tag{2.10}$$

where $\mu(\mathbf{v}, N)$ is the number of occasions at which voxel $\mathbf{v}$ is crossed by a streamline. Figure 2.15 illustrates the steps of the probabilistic tractography algorithm. Figure 2.16 [34] shows the connection probability from a seed voxel in the lateral geniculate nucleus over three slices of a brain dataset.

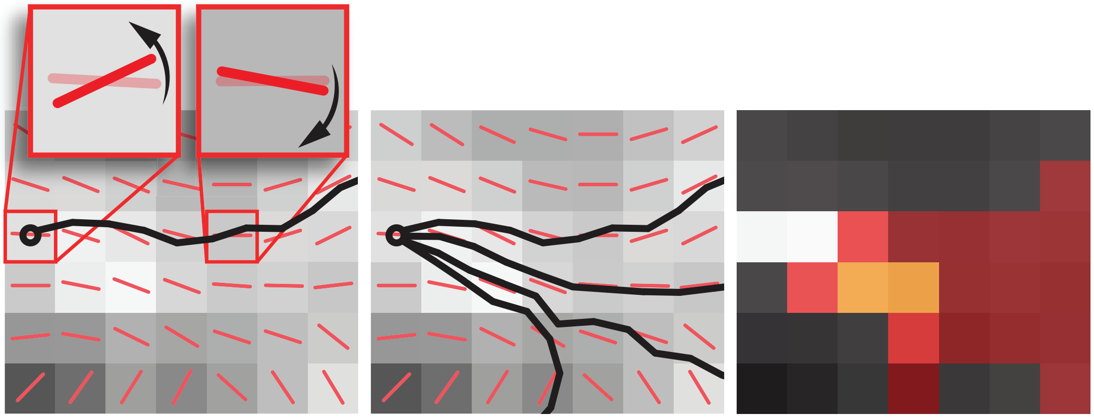

Figure 2.15: Main steps of probabilistic tractography algorithm. A streamline is propagated from the seed point (indicated by the circle), perturbing the fibre-orientation estimate at each step according to some uncertainty estimate (left). This process is repeated multiple times and provides us with a set of streamlines (centre). The connectivity index is then the proportion of streamlines that pass through each voxel (left).

Several alternative methods for modelling the uncertainty of fibre-orientation estimates have been developed. These fall into three main categories; calibration-based, bootstrap and Bayesian estimates.

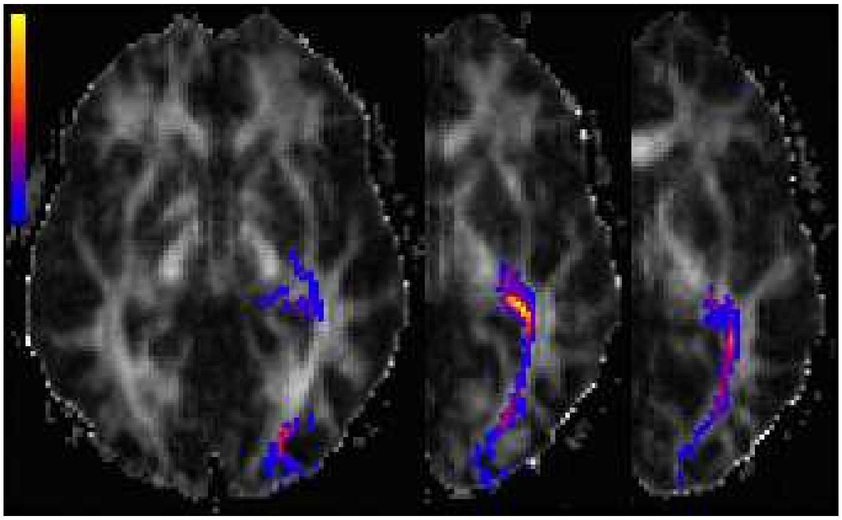

Figure 2.16: An example of probabilistic tractography. The images show the connection probabillity from a seed voxel in the lateral geniculate nucleus. Taken from [34]

2.4.2.1 Calibration-based Estimates of Uncertainty

Calibration-based methods use some feature of the reconstruction to estimate the uncertainty of the corresponding fibre-orientation estimate. Parker et al [40, 10, 43], Cook et al [36] and Lazar et al [41] all use a calibration approach to estimating uncertainty. They construct a mapping from some rotationally invariant feature of the diffusion to the variance of the fibre-orientation estimate using simulations. In the simplest algorithm [40], for example, Parker et al create a population of deflection angles between a known fibre direction and an estimate reconstructed by fitting the diffusion tensor (DT) to noisy synthetic data. They model the deflection angles with a Gaussian distribution and repeat for several levels of anisotropy in the synthetic data. Finally, they fit a linear model of the relationship between the FA and the variance of the Gaussian model, which they use to predict the variance in each voxel during tractography.

Cook et al [36] use calibrated PICo with more standard spherical distributions such as the Watson and Bingham distributions [44] instead of Parker et al's Gaussian to model fibre-orientation uncertainty. They evaluate their method using synthetic data and within PICo tractography tasks on brain data. They show that both the Watson and Bingham distributions are better for modelling the uncertainty of fibre-orientation estimates than Parker et al's Gaussian model. In particular, the Bingham model captures anisotropy in the uncertainty.

2.4.2.2 Bootstrap Estimates of Uncertainty

Jones et al [45, 46], Lazar [47] and Haroon et al [48] use statistical bootstrap techniques to obtain samples of the fibre-orientation estimate distribution. The basic technique, developed by Jones et al [45] uses conventional bootstrap method to predict uncertainty. First, they acquire 8 repeats of diffusion weighted brain data. Then, for each voxel, the bootstrap method is employed to generate bootstrap data. The principal eigenvector of each bootstrap sample yields a population of fibre-orientation estimates in each voxel, which can be used directly in the probabilistic tractography algorithm.

One inherent problem with the basic technique described in [45] is that multiple acquisitions are required. Jones et al [46] overcome this limitation using the Wild bootstrap technique [49]. The wild bootstrap technique involves modifying the residuals of a diffusion tensor fit, and then re-fitting the diffusion tensor. The bootstrap estimates of fibre-orientation can then be used in the same was as the estimates from the conventional bootstrap.

2.4.2.3 Bayesian Estimates of Uncertainty

Behrens et al [50] and Hosey et al [51] use Markov Chain Monte Carlo (MCMC) to sample the posterior distribution of the parameters of a diffusion model (including fibre orientation) directly. Behrens et al [50] use a model which consists of an isotropic component and a highly anisotropic component to form a “ball and stick” model (see section 3.3.2 for details). They estimate parameters for this model, including the fibre orientation, using Monte Carlo simulation. These parameters are then used directly in the probabilistic tractography algorithm as samples of the distribution of orientations.

Friman et al [52] also use a Bayesian approach to estimate uncertainty, but they avoid the usage of MCMC by fixing some of the parameter in their model of diffusion and then integrating over the unit sphere. As a result, this method is faster than those of [50] and [51]. However, the constrained model is an over-simplification of the diffusion process.

2.5 Conclusion

In this section we provided a basic introduction to MRI and how it is extended to capture diffusion processes. We then described the problem of estimating features of the scatter pattern given a set of measurements, as well as a popular reconstruction algorithm (DTI) that assumes a simple Gaussian model of the scatter pattern. Finally, we show how tractography algorithms use estimates of fibre-orientation to estimate the paths of white-matter tracts through the brain. However, there are many complex white-matter configurations in the brain and many, if not all, white-matter tracts will include regions of complex microstructure. Therefore, incorporating multiple-fibre reconstruction algorithms is desirable. In the next chapter we introduce the main multiple fibre algorithms as well as some of the approaches to using them in tractography.

Chapter 3

Multiple Fibre Reconstruction Techniques

3.1 Introduction

The previous chapter introduces diffusion tensor imaging (DTI). The technique has become popular because it provides two unique insights into tissue microstructure: it quantifies diffusion anisotropy, which is a useful index of white matter integrity, and provides an estimate of the principal direction of axon fibres, which enables tractography. Powerful though it is, DTI has several limitations. One key limitation is that it can only recover a single fibre orientation in each voxel and fails at fibre crossings. This limitation is a major obstacle for tractography and connectivity mapping. However, it is not a limitation of diffusion MRI in general, but merely the modelling assumptions that DTI makes. This chapter covers a variety of alternative models and algorithms that aim to recover more detailed information about the orientations of fibres from diffusion MRI measurements and, in particular, to resolve the orientations of crossing fibres. We start the chapter in section 3.2 with a conceptual overview of the limitations of DTI and the problems that crossing fibres and other complex fibre configurations present. Sections 3.3 and 3.4 outline the key methods for modelling and resolving multiple fibres. We summarize the pros and cons of each method at the end of section 3.4. Section 3.5 discusses specific information we can extract from the output of the algorithms in sections 3.3 and 3.4 such as multiple dominant-orientations and indices of anisotropy or complexity. Section 3.7 discusses applications, in particular, to improve tractography and connectivity mapping. This chapter is based on work published in [18] in 2009.

The algorithms selected were the most commonly used at the time of writing.

3.2 Multiple Fibres: What's all the fuss about?

In white matter, the configuration of axon fibres has a big effect on the shape of p. White matter axons are tiny compared to typical MRI voxels. Axon radii are in the range [0.1,10] μm, whereas voxels typically have sides in the range [1,5] mm. Voxels therefore contain hundreds of thousands of axon fibres, which can adopt a wide range of often complex configurations. Some configurations produce Gaussian-like scattering, but others can produce p with highly non-ellipsoidal contours. When p departs significantly from the Gaussian model, the DT contains very little useful information and can be actively misleading. Figure 3.1 shows some relatively simple configurations of axons within single image voxels together with an illustration of the scatter pattern we expect within each. We depict the scatter as distributions of displacements from one starting position, although in a real diffusion MRI experiment, the initial positions are approximately uniformly distributed over the voxel. Figure 3.1 also shows the DT that gives the best approximation of each p and the principal direction of each DT, which is the estimate of the dominant fibre orientation for each configuration. The last two columns show an object called the fibre orientation distribution and the directional variation of the diffusion signal, both of which we explain below.

When the fibres are all straight and parallel (row 1 of figure 3.1), p is highly anisotropic and elongated in the fibre direction. The DT reflects the shape of p, since p has approximately ellipsoidal contours, and the principal direction gives a good estimate of the single fibre orientation. The second and third rows show more complex configurations in which the fibres are fanning and bending, within a plane, respectively. In both cases, p and the corresponding DT are less anisotropic than for the straight parallel fibres. In particular, the largest eigenvalue becomes smaller and the middle eigenvalue is larger. In the straight parallel fibres example, molecules tend to move in the vertical direction in the figure, wherever they are in the voxel. In the bending example, however, movement depends on location within the voxel. Molecules at the bottom of the voxel tend to move along an axis about 30° to the vertical, while those in the middle tend to move along the vertical axis and at the top along an axis 30° the other side of the vertical. The scatter pattern for the whole voxel contains contributions from

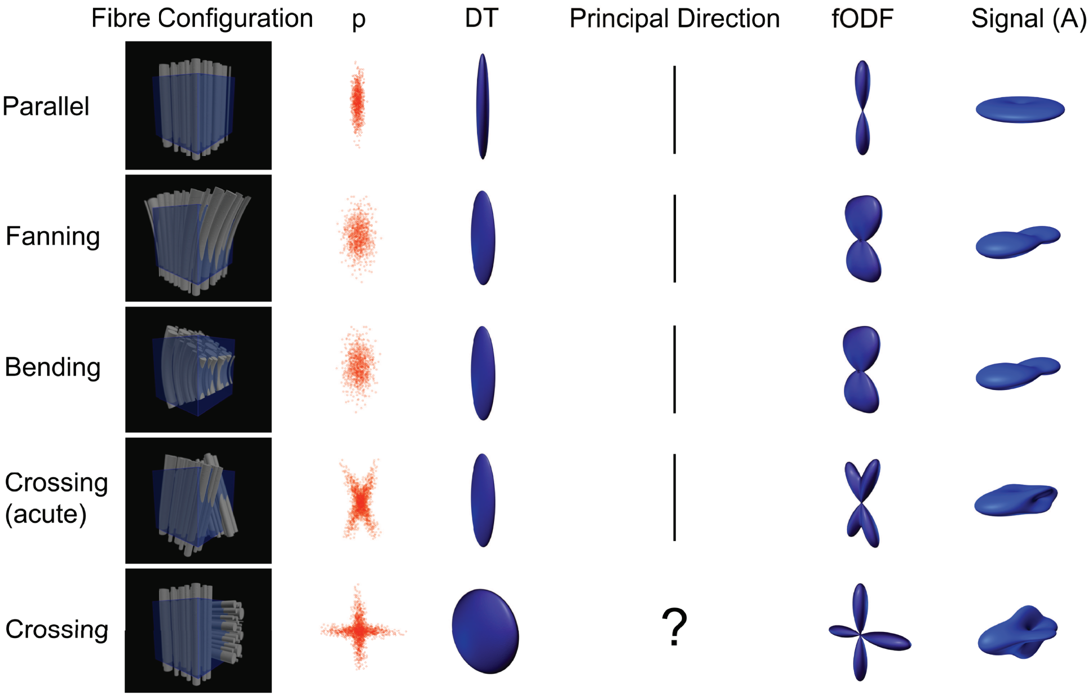

Figure 3.1: Illustration of various simple configurations of axon fibres that arise frequently in brain-image voxels (first column). The second column shows the kind of scatter pattern we expect from each of the fibre configurations in the first column. The third column shows the best-fit DT, the fourth shows the principal direction of the DT and the fifth shows the fibre orientation distribution function (fODF) for each configuration. The sixth column shows the directional variation of the diffusion-weighted signal for fixed diffusion weighting. In the last row, the DT is perfectly oblate so the principal direction in undefined. In practice, noise will cause the principal direction to have random orientation in the plane of the two crossing fibres.

all areas; on average, we see more horizontal scattering than in the straight parallel fibres configuration. Note, however, that the bending does not affect the displacements in and out of the bending plane, so the smallest eigenvalue of the DT remains the same as the straight parallel fibres and the DT is intermediate between prolate and oblate. The fanning configuration produces an identical DT to the bending configuration in a similar way. For both the fanning and bending configuration, the principal direction is unchanged from the straight parallel fibres configuration. The principal direction now provides a good estimate of the mean fibre direction, but does not reflect the full complexity of the configuration. The shape of the DT may convey some information about the configuration, but it is difficult to separate the effects of the configuration of fibres from other effects, such as fibre size and density and contributions from other tissue types. Moreover, the fanning and bending configurations are indistinguishable given only the DT.

The last two rows in figure 3.1 show crossing fibre configurations. The fourth row shows an oblique crossing. Although p for the oblique crossing is different to the fanning and bending configurations and clearly has non-ellipsoidal shape, the best-fit DT is identical to the fanning and bending configurations. The principal direction is now actively misleading, as the mean fibre direction does not correspond to the direction of any fibre in the voxel. The orthogonal crossing produces p with cross-shaped contours that reflect the multiple fibre orientations. The DT cannot capture this contour shape and the closest Gaussian approximation to p is a perfectly oblate DT, which contains none of the useful directional information in the true p.

For comparison, the fifth column in figure 3.1 shows the distribution of fibre orientations within each configuration. This object will be important later in this chapter and we shall refer to it as the fibre orientation distribution function (fODF). The fODF quantifies the fraction of fibre portions (note that fibres may vary in orientation along their length) within a voxel with each orientation. Mathematically, the fODF is a probability distribution on the sphere, as each point on the sphere corresponds to a unique orientation. For example, the simplest configuration in figure 3.1 is the straight parallel fibres in the first row. This configuration has only one fibre orientation, since the orientation of all the fibres is the same and does not vary along the fibre lengths. The fODF is therefore zero for any orientation other than vertically upwards and has a sharp

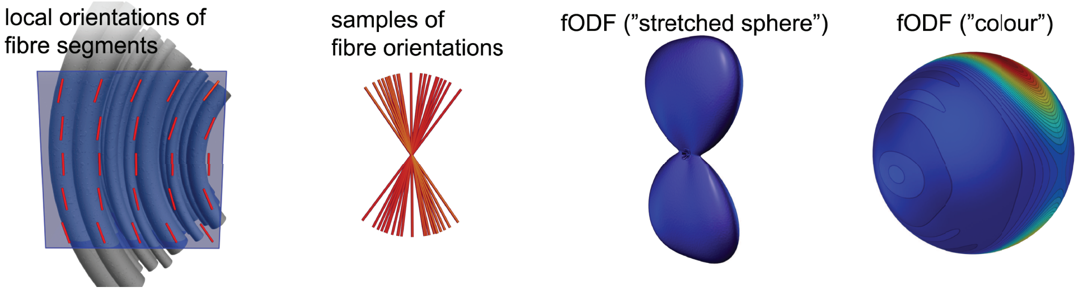

Figure 3.2: Illustration of the fibre-orientation distribution function in a voxel containing bending fibres. The fibre orientation depends on location in the voxel (left). The fODF captures the set of orientations from all positions with the voxel. Centre-left shows the set of orientations drawn on the bending configuration on the left panel. The two images on the right show different representations of the fODF. The first method (centre right) scales the radius of the sphere by the value of the fODF. The second method uses a colour map to represent the fODF; hot colours indicate high values of the fODF.

spike in the upward direction. (The pictures in figure 3.1 exaggerate the widths of the peak for visibility.) Other configurations have less trivial fODFs. Figure 3.2 shows an illustration for the bending configuration in row 3 of figure 3.1. Each fibre has a range of orientations from up and left at the bottom of the voxel, to vertically up at the centre and up and right at the top. Each orientation contributes to the fODF so the fODF is non-zero for a range of orientations in the plane of the bending, but, for this idealized bending example, zero everywhere else. The fODF therefore has the shape of a shovel or paddle head. (Again, the figure exaggerates the width of the shovel for visualization.) Figure 3.2 uses two visual representations for functions on spheres to illustrate the fODF. The first ("stretched sphere") stretches the radius of the sphere by the value of the function; the second ("colour") uses colour to reflect the value of the function in each direction. In the stretched-sphere representation, peaks of the shape reflect the most common fibre directions. In the colour representation, hot colours indicate high values and appear in the most common directions.

Spherical acquisition protocols became standard for DTI because they reduce the dependence of anisotropy and fibre-orientation estimates on true fibre-orientation (see [53]). These protocols acquire diffusion weighted measurements with fixed diffusion weighting (b-value) but varying direction. The measurement therefore depends only on orientation and thus is a function of the sphere like the fODF. Figure 3.1 also shows how the measurement varies as a function of direction for each configuration. The measurement function is very different to the fODF. For simple configurations (rows 1-3) the measurement is small where the fODF is large, since more diffusion in the mean direction causes more signal attenuation. However, the last two rows reveal a more complex relationship between the two functions. In the orthogonal crossing-fibre configuration, the signal has local maxima in the fibre directions whereas in the oblique crossing configuration neither the local maxima or minima of the signal are in the fibre directions. Diffusion tensor imaging protocols typically sample this measurement function in 30-100 directions (see [53]). These sets of measurements capture enough of the directional variation of the diffusion weighted signal potentially to provide the angular resolution to resolve crossing fibres. Early experiments [54, 55] compare these spherical measurement functions with what we would expect if p were Gaussian. Results show clear departures from the Gaussian consistently in known fibre-crossing regions. These observations motivated the development of a variety of techniques for resolving multiple fibre orientations and capturing complex fibre configurations. Some of these techniques use more flexible models than DTI, such as multi-tensor models, to separate contributions from distinct fibre populations; we cover these methods in section 3.3. Other non-parametric techniques aim to estimate the full distribution of fibre orientations, i.e. the fODF, in each voxel. Some of this latter class, including Diffusion Spectrum Imaging, QBall Imaging and Persistent Angular Structure MRI, use the directional structure of p to reflect the fODF. Others, such as spherical deconvolution methods, combine modelling and non-parametric approaches to reconstruct the fODF more directly. Section 3.4 covers non-parametric approaches.

3.3 Model-based Approaches

This section looks at model-based approaches that resolve fibre-crossings by modelling distinct fibre populations separately.

3.3.1 The Multi-Tensor Model

The multi-tensor model is a simple generalization of DTI, which replaces the Gaussian model for p with a mixture of n Gaussian densities. The model assumes the voxel

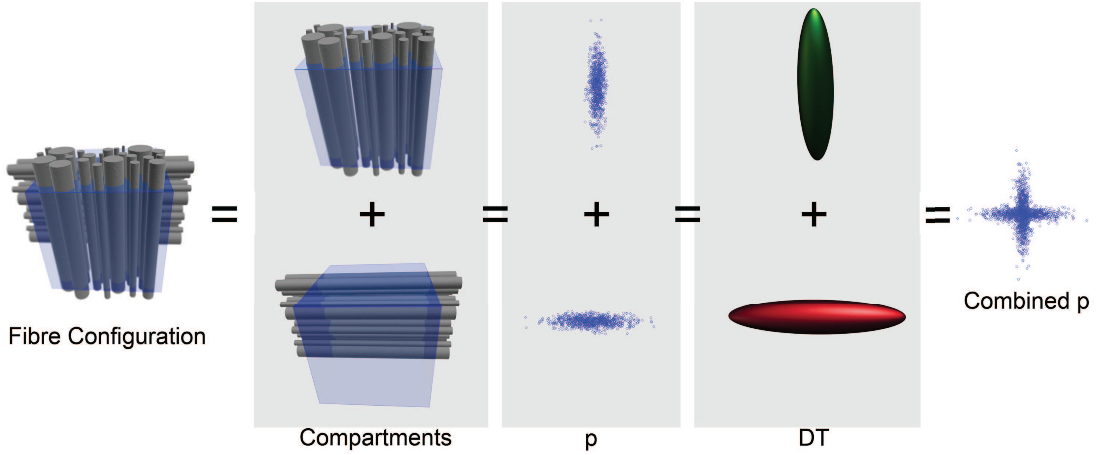

Figure 3.3: Illustration of a multi-compartment model for a crossing fibre-configuration (first panel). In this example, the fibre configuration can be split into two compartments (second panel), which each have their own p (third panel). Each compartment is modelled by a separate DT (fourth panel). When the DTs are combined, they model the complete p for crossing.

contains n distinct groups or “populations” of fibres and that diffusing molecules stay within only one population (no exchange between populations). The approach models each population by a separate DT. Figure 3.3) illustrates the idea for $n = 2$ and the crossing configuration in the last row of figure 3.1. The p for the whole voxel is the sum of the Gaussians that each DT represents weighted by the fraction of the volume that each population occupies. We can write this mathematically as

$$p(\mathbf{x}) = \sum_{i=1}^{n} a_i G(\mathbf{x}; \mathbf{D}_i, t), \tag{3.1}$$

where each $a_i \in [0, 1]$ is the volume fraction of the i-th fibre population and $\sum_i a_i = 1$, $G(\cdot; \mathbf{D}, t)$ is the Gaussian function with zero mean and covariance $2\mathbf{D}t$, t is the diffusion time and $\mathbf{x}$ is a displacement.

In multi-tensor approaches, we estimate the parameters of the model for p, i.e. $a_1, ..., a_n$ and $\mathbf{D}_1, ..., \mathbf{D}_n$, from a set of diffusion-weighted measurements. With the model in equation 3.1, we can write the normalized diffusion-weighted signal

$$A(\mathbf{q}) = \sum_{i=1}^{n} a_i \exp(-t\mathbf{q}^T \mathbf{D}_i \mathbf{q}), \tag{3.2}$$

For spherical acquisition schemes, both t and $|\mathbf{q}|$ are fixed (so b is fixed) and only the gradient direction varies among measurements, so we could rewrite equation 3.2

$$A(\hat{\mathbf{q}}) = \sum_{i=1}^{n} a_i \exp(-b\hat{\mathbf{q}}\mathbf{D}_i\hat{\mathbf{q}}). \tag{3.3}$$

Although spherical acquisition schemes are common for fitting multi-tensor models, b may vary among measurements and $\mathbf{q}$ and t may even vary independently.

The multi-tensor model assumes that the number, n, of distinct fibre populations is known. Practical considerations, such as the number of measurements and the measurement noise level, limit the number of orientations the method can resolve reliably and most work uses a maximum n of 2. When $n = 1$, the model is exactly that used in DTI.

Unlike the DT model, the parameters, $\mathbf{D}_1, ..., \mathbf{D}_n$ of the multi-tensor model cannot be expressed as a linear function of the measurements so the model fitting requires non-linear optimization. Once fitted, the principal eigenvector of each $\mathbf{D}_i$ provides a separate fibre-orientation estimate.

Figure 3.4 visualizes the full two-tensor model in each voxel of an axial slice of human brain data. The brain data consists of 60 diffusion-weighted images with $b = 1200\,\mathrm{s\,mm^{-2}}$ and unique evenly distributed gradient directions and one $b = 0$ image for normalization. The image size is $128 \times 128 \times 60$ with isotropic voxels that are approximately $2 \times 2 \times 2\,\mathrm{mm}^3$ in size. Glyphs showing contours of p are overlaid onto a fractional anisotropy (FA) map from the one-tensor model (i.e. DTI). The figure shows one- and two-tensor models for two regions of interest. Panels 3.4a and 3.4b show a region of fibre crossing where several fibres intersect, including the superior fronto-occipital fasciculus and the corpus callosum. In figure 3.4a, the two-tensor models reveal multiple directions, but DTI (figure 3.4b) fits oblate single tensors that fail to reveal any useful direction information. Figures 3.4c and 3.4d highlight the limitation of the two-tensor model. The region has a single dominant fibre orientation which the single tensor recovers very well. The two-tensor model can become unstable when only one population is present and produce spurious results. We have emphasized this in figure 3.4c by showing both DTs in each voxel without using the weightings a_1 and a_2. The fitted volume fractions of the DTs less well aligned with the fibre direction tend to be small, but the figure reveals greater deviation of the dominant direction from the fibre direction than the single-tensor model in figure 3.4d.

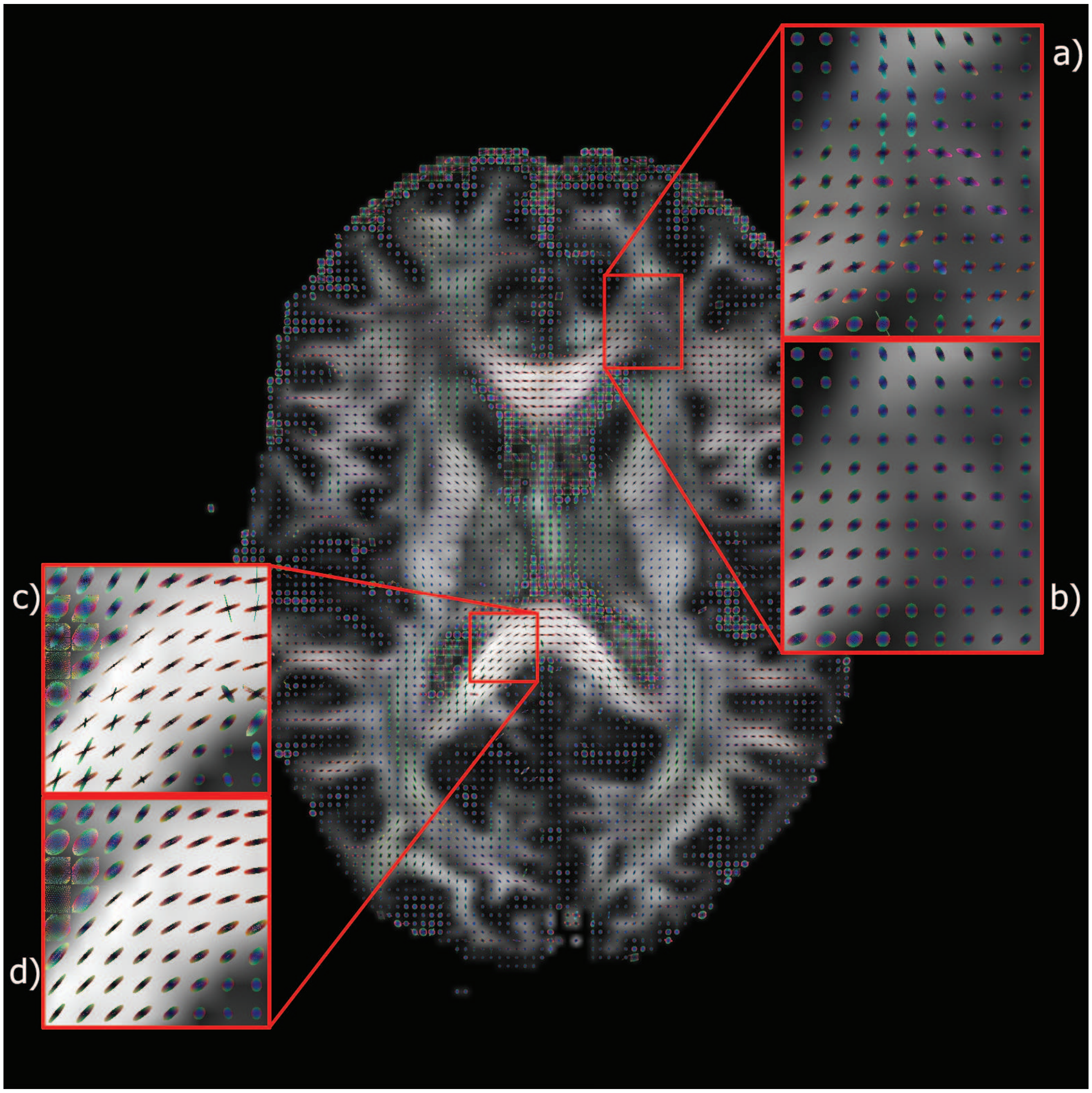

Figure 3.4: Two-tensor models fitted in each voxel of an axial slice of a normal human brain dataset. The model is the full 13-parameter two-tensor model in every voxel. Ellipsoidal contours of p from both tensors are overlaid on a standard FA map. Inset images a and b show two- and one-tensor models respectively for a crossing-fibre region. c and d show two- and one-tensor models respectively for a region of the corpus callosum which has a single fibre-population.

3.3.2 Limitations, Refinements and Special Cases

The general form of equation 3.1 accommodates a wide range of special cases with different constraints on the n DTs. For $n = 2$, the full tensor has 13 free parameters: the six components of each DT and one for the volume fraction a_1 and a_2 (since $a_2 = 1 - a_1$). The large number of parameters is one cause of the instability we highlight in figure 3.4. Constraints on the model can reduce complexity and help stabilize the fitting procedure. For example, in the multi-tensor model, we can enforce positive definiteness using the Cholesky decomposition, as in [56], or cylindrical symmetry on the component DTs, as in [57], or fix the DT eigenvalues, as in [58]. Spatial regularization techniques also help overcome the fitting problem by ensuring voxel-to-voxel coherence, see [56, 59].

A particularly simple model with the form of equation 3.1 is Behrens' ball-and-stick model. The ball and stick model [50, 51] assumes that water molecules belong to one of two populations: a restricted population of water molecules in and around fibres with scatter pattern p_r and a free population that does not interact with fibres and has scatter pattern p_f. Behrens et al [50] use an isotropic Gaussian model for p_f. They use a Gaussian model for p_r in which the DT has only one non-zero eigenvalue so that particles move only in the fibre direction. The ball and stick model extends naturally to multiple-fibres by including multiple "sticks" in the model.

The ball and stick model is deliberately over-simplified. Several related models are similar in separating free and restricted compartments, but use more expressive models for the components. Kaden et al [60] model diffusion in a similar way to the ball and stick model, but replace the "stick" components with distributions of sticks to capture less-trivial fODF structure that fanning or bending might produce. Assaf et al's Composite hindered and restricted model of diffusion (CHARMED) [61] models p_r with an analytical model for diffusion restricted to a cylinder [62] and p_f with an anisotropic Gaussian model (the "hindered" diffusion in the extra-cellular space).

The choice of n presents a model-selection problem: in voxels with only one fibre orientation, we lose accuracy by fitting a model with $n \geq 2$. For example, figure 3.4c shows that the two-tensor model provides poorer estimates of the single fibre-orientation in the corpus callosum than the one-tensor model. Ideally, we would fit a one-tensor model in voxels with one fibre population, a two-tensor model in those with two populations, and so on. The statistics literature is extensive on model selection and we will not review it here other than to mention some approaches used specifically for choosing the number of fibres in diffusion MRI. Parker and Alexander [43] use the spherical-harmonic voxel-classification algorithm proposed in [55] to classify voxels as isotropic, one-fibre or two-fibre, but the method does not extend naturally above $n = 2$. Tuch [58] thresholds the correlation of the measurements with their predictions from the $n = 1$ model in each voxel separately to decide whether to use $n = 1$ or $n = 2$. Behrens et al [9] use a Bayesian approach.

3.3.3 Acquisition Requirements

Alexander and Barker [57] recommend, based on simulations, using a spherical acquisition with b in the range $2200 - 2800\,\mathrm{s\,mm}^{-2}$ when acquiring data in 64 gradient directions. With these settings the two-tensor model resolves 60° crossings consistently but consistently does not resolve 30° crossings with SNR of 16).

3.4 Non-Parametric Algorithms

The model-based techniques in the previous section recover a finite number of dominant fibre-orientations and do not naturally distinguish, for example, fanning or bending configurations from parallel fibre populations. The motivation for all the methods in this section is to estimate the fODF from diffusion MRI measurements, which provides more insight into the underlying configuration. We call the methods in this section non-parametric because they do not rely solely on parametric models of p, but try instead to reconstruct the fODF without placing modelling constraints on its form.

This section covers a variety of methods that reconstruct different functions of the sphere and use them as estimates of the fODF. Diffusion spectrum imaging (DSI) and QBall imaging reconstruct a function called the diffusion orientation distribution function (dODF). The DOT algorithm and the original PASMRI algorithm recover slightly different functions that contain similar information to the dODF. Spherical deconvolution methods recover a more direct estimate of the fODF. We begin this section by considering these different objects and how they relate to the fODF.

Like the fODF, the dODF is a probability distribution on the sphere. The dODF is the probability that a diffusing water molecule moves in a particular direction. That

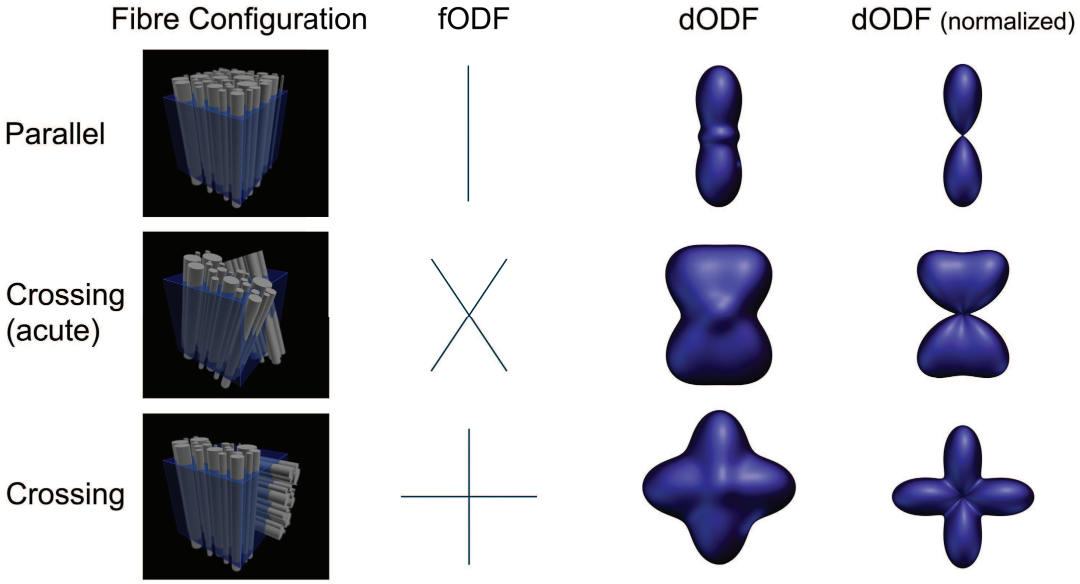

Figure 3.5: Illustration of ODFs for several simple white-matter configurations. The second column shows the fODF for each configuration. The third and fourth columns show the dODF and normalized dODF respectively for each white-matter configuration. The normalized dODF is rescaled so that its minimum value becomes zero. This emphasizes the directional structure of the dODF without affecting peak directions.

probability is not the same as the fraction of fibres with that orientation. Figure 3.5 compares the fODF and the dODF for various axon fibre configurations. An immediate qualitative difference between the fODF and the dODF is that the dODF is a smoother, less spiky function. Consider the straight parallel fibres configuration. As discussed in section 3.2, the fODF is zero apart from a single spike in the fibre direction. The dODF is much broader, although the peak is still in the fibre direction. Although water molecules are most likely to move in the fibre direction, moves in other directions, even perpendicular to the fibres, are still common. Axon fibres have finite inner diameter so accommodate perpendicular moves, as does the extra-cellular space, which also contains diffusing water that contributes to the signal. Thus the dODF is non-zero for all directions, even for the sharpest possible fODF. However, the broad structure of the two functions is similar; in particular, the peaks are in similar directions.

The model-based approaches of the previous section do not recover an estimator of the fODF directly, although we might consider the set of principal directions as an fODF estimate that is non-zero only in a finite set of directions. Probabilistic tractography techniques (see section 2.4) often use the uncertainty on discrete fibre-orientation estimates as an estimate of the fODF. The distinction between the uncertainty of discrete fibre orientation estimates and the fODF is subtle but important. We shall refer to the former as the uncertainty ODF (uODF), as it is also a probability distribution on the sphere. The uODF in one direction is the probability that, under the assumption the voxel contains n distinct fibre populations, one of those populations is in that direction. That probability is not the same as the fraction of fibres with a particular orientation, which is the fODF. Like the dODF, however, the uODF has similar structure to the fODF and provides a useful estimate.

3.4.1 Diffusion Spectrum Imaging

Diffusion Spectrum Imaging (DSI) [63, 64] attempts to measure p directly and makes no assumptions about tissue microstructure or the shape of p. For an idealized pulse sequence with infinitesimally short gradient pulses, p for diffusion time t is the Fourier transform (FT) of the measurement function A with pulse separation t (see section 2.2.2). For this idealized pulse sequence, A depends only on wave vector $\mathbf{q}$, which is a vector in 3D space that we can control by varying the gradient strength and orientation (see [65]). Diffusion spectrum imaging acquires measurements for each of a grid of wavevectors. This configuration of samples allows us to use a fast Fourier transform (FFT), which provides a similar grid of samples of the FT of the measurement function, i.e. p. Thus, DSI samples A on a grid of $\mathbf{q}$ and the FFT provides samples of p on a grid of displacements $\mathbf{x}$. The first two panels of figure 3.6 illustrate this step.

The acquisition scheme for DSI is very different to the spherical acquisition schemes we have considered up to now. For spherical acquisition $|\mathbf{q}|$, and thus b, is fixed so all wavevectors are equidistant from the point $\mathbf{q} = 0$ and lie on a sphere in $\mathbf{q}$-space. The grid sampling scheme in DSI typically samples the whole interior of a sphere in a regular grid of samples; figure 3.7 compares the two schemes.

The discrete representation of p we get from the FFT is not directly useful for estimating the fODF, since it is a function of 3D space. The dODF comes from a simple projection of p onto the sphere. The value of the dODF for each orientation is the sum of p at all points on a line through the origin with that orientation (see figure 3.7, third panel). More formally, the dODF ϕ of p is [64]:

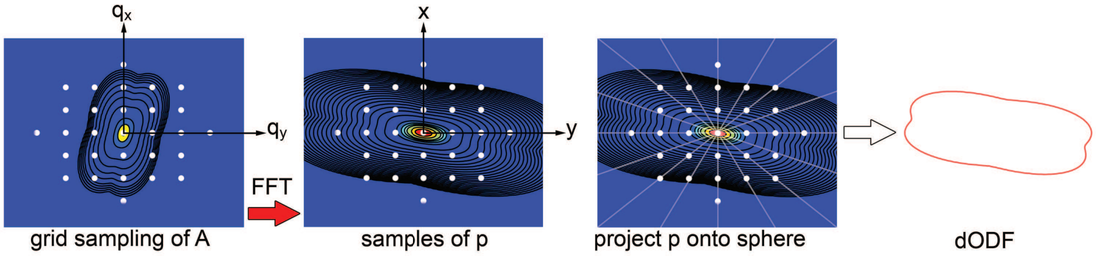

Figure 3.6: 2D illustration of estimating the dODF using DSI. The left panel shows the measurement function as a function of $\mathbf{q}$ The white spots show the values of $\mathbf{q}$ at which we acquire a measurement $A(\mathbf{q})$ and have a grid formation. The second panel shows p, which is the FT of A, together with the grid formation of displacement vectors at which the FFT provides a value of p. To obtain the dODF (right), we interpolate the grid of samples of p and integrate along radial lines through the origin, as the third panel depicts.

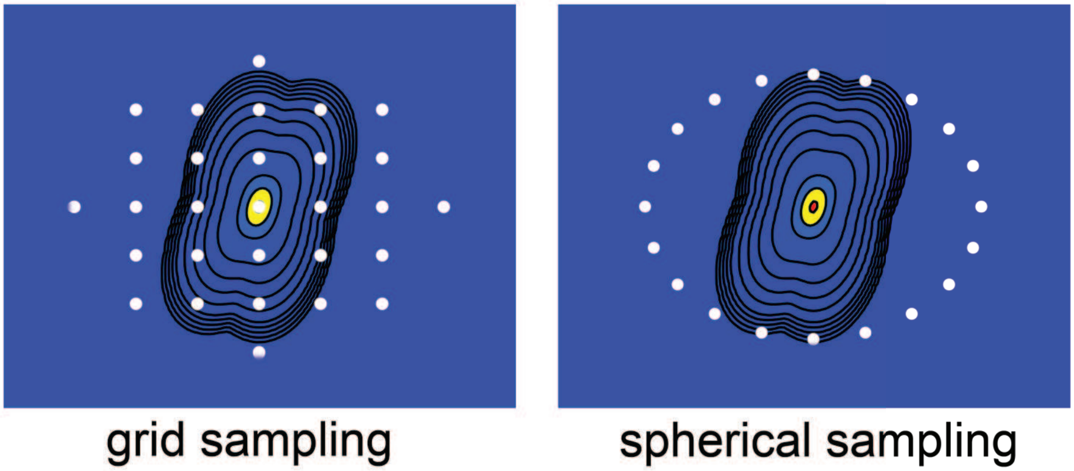

Figure 3.7: 2D illustration of a grid sampling (left) and a spherical acquisition (right) for sampling $\mathbf{q}$-space.

$$\phi(\hat{\mathbf{x}}) = \int_0^\infty p(\alpha\hat{\mathbf{x}})\mathrm{d}\alpha \tag{3.4}$$

where $\hat{\mathbf{x}}$ is a unit vector in direction of $\mathbf{x}$. Diffusion spectrum imaging usually computes $\phi(\hat{\mathbf{x}})$ for each of a finite set of directions $\hat{\mathbf{x}}$ by taking steps along the line in direction $\hat{\mathbf{x}}$, interpolating the discrete p to estimate its value at each step and summing the values over all steps.

3.4.1.1 Limitations

The major limitation of DSI is the acquisition requirements. To cover the required 3D grid of points in $\mathbf{q}$-space typically requires an order of magnitude more measurements than typical DTI spherical acquisition schemes acquire. Standard protocols typically acquire 500-1000 measurements. In practice, image resolution must decrease to acquire so many measurements in tolerable time.

A further limitation is reliance on the FT. The Fourier relationship between p and A relies on infinitely short pulses. In practise pulses are not infinitely short and have length close to the diffusion time so depart significantly from the assumptions of the technique. The effect is considerable blurring of p and the derived dODF, although strong peak directions are not affected a great deal.

3.4.1.2 Acquisition Requirements

In the original work [63], Wedeen et al use an acquisition with 500 values of $\mathbf{q}$ and a maximum b-value of $20,000\,\mathrm{s\,mm^{-2}}$. In [66], Kuo et al attempt to optimize the acquisition scheme for DSI. They recommend a maximum b-value of $6500\,\mathrm{s\,mm^{-2}}$ if the number of $\mathbf{q}$ is 515 and a maximum b-value of $4000\,\mathrm{s\,mm^{-2}}$ with 203 measurements.

3.4.2 QBall Imaging

QBall imaging (QBall) [67, 68] approximates the dODF that DSI estimates using measurements from a spherical acquisition scheme. Acquisition requirements are therefore more manageable than DSI although the approximation of the dODF introduces some blurring, which may reduce angular resolution and precision of peak directions.

The approximation of the dODF comes from a transform called the Funk Radon Transform (FRT). The FRT is a transformation of spherical functions that maps one function of the sphere to another. The FRT of a spherical function f at a point $\hat{\mathbf{x}}$ on the

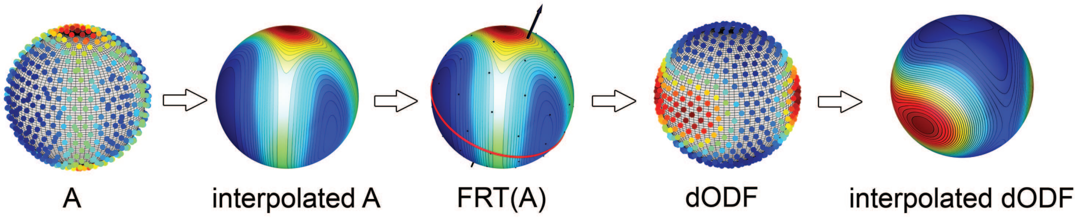

Figure 3.8: Steps of the QBall Algorithm. We start (left) with samples of A at fixed $|\mathbf{q}|$ with various different directions. We interpolate on the sphere to approximate the continuous A at fixed $|\mathbf{q}|$ (panel 2). To sample the dODF in one direction, we sum the interpolated A around the perpendicular equator (panel 3). We repeat the procedure in various directions to obtain many samples of the dODF (panel 4). Finally, we may interpolate to approximate the continuous dODF. In this figure points on the sphere indicate a sampled function; solid shading of the sphere indicates a continuous function.”

sphere is the integral of f over the great circle $\mathcal{C}(\hat{\mathbf{x}})$ that lies in the plane perpendicular to $\hat{\mathbf{x}}$ through the origin. The QBall approximation of the dODF is simply the FRT of the measurement function on a shell in $\mathbf{q}$-space (like those shown in figure 3.1). Mathematically, we can write this

$$\phi(\hat{\mathbf{x}}) = \int_{\mathcal{C}(\hat{\mathbf{x}})} A(\mathbf{q}) \mathrm{d}\hat{\mathbf{q}}, \tag{3.5}$$

where $\hat{\mathbf{q}} = \mathbf{q}/|\mathbf{q}|$. Figure 3.8 illustrates the procedure.

In the absence of noise, the approximation of ϕ becomes closer as the fixed $|\mathbf{q}|$ or b-value of the measurements increases [64]. However, in practise, noise becomes more significant as $|\mathbf{q}|$ increases and a good balance needs to be found, [69] studies the trade-off in simulation.

The steps of the original QBall algorithm are

- Interpolate the discrete set of measurements on the sphere in $\mathbf{q}$-space to estimate the measurement at each point on each contour $\mathcal{C}(\hat{\mathbf{x}})$.

- Compute FRT by summing interpolated measurements on even steps around $\mathcal{C}(\hat{\mathbf{x}})$ to get samples of the dODF.

- If required, interpolate the dODF samples with a linear basis for spherical functions. This means we represent ϕ as a linear combination of a set of simple functions that can be combined to approximate more complex functions:

$$\phi(\hat{\mathbf{x}}) = \sum_k \beta_k \theta_k(\hat{\mathbf{x}}), \tag{3.6}$$

where θ_k are the basis functions and β_k are the weights.

These steps can be combined to a single matrix multiplication, which makes the QBall algorithm computationally light. Tuch's original implementation [67] uses radial basis functions to interpolate A and represent ϕ. Appendix B provides a slightly different, but general implementation for any linear basis [69].

Figure 3.9 shows dODFs reconstructed using Tuch's original QBall algorithm in each voxel of the same slice as figure 3.4. For each glyph, we normalize the range of the dODF to [0,1] to emphasize shape, as Tuch suggests in [64]. Figure 3.9a shows that the dODFs have single peaks along the expected fibre directions in the corpus callosum. In the fibre-crossing region, figure 3.9b, the dODF shapes reflect the orientations of the crossing fibres but may not have separate peaks in each direction because the functions are too smooth. However, the b-value in this dataset is lower than optimal for resolving two fibre directions using QBall [64, 69].

3.4.2.1 Limitations and Refinements

Later work [70, 71, 72] use spherical harmonics in place of the radial basis function for θ, which gives a more compact representation of ϕ and avoids numerical computations as the FRT has analytic form if A in equation 3.5 is a linear combination of spherical harmonic functions.

A related method called the Diffusion Orientation Transform (DOT) [73] calculates a variant of the dODF. The DOT is a single contour of p at fixed radius R_0. The single contour of p is distinct from the dODF, which has contributions from all contours. In practice, for sensible choices of $|\mathbf{q}|$ and R_0, the two functions appear similar.

3.4.2.2 Acquisition Requirements

In [67], Tuch uses an acquisition with 252 gradient directions at a $b = 4000\,\mathrm{s\,mm^{-2}}$. Kuo et al [16] recommend using a b of $3000\,\mathrm{s\,mm^{-2}}$ with 493 gradient directions and $2500\,\mathrm{s\,mm^{-2}}$ with 253 directions. More recently, Tournier et al [74] show that QBall with 80 gradient directions at $b = 4000\,\mathrm{s\,mm^{-2}}$ when SNR=95 can resolve 45° crossings consistently but not 30° crossings using data acquired from the phantom of Lin et

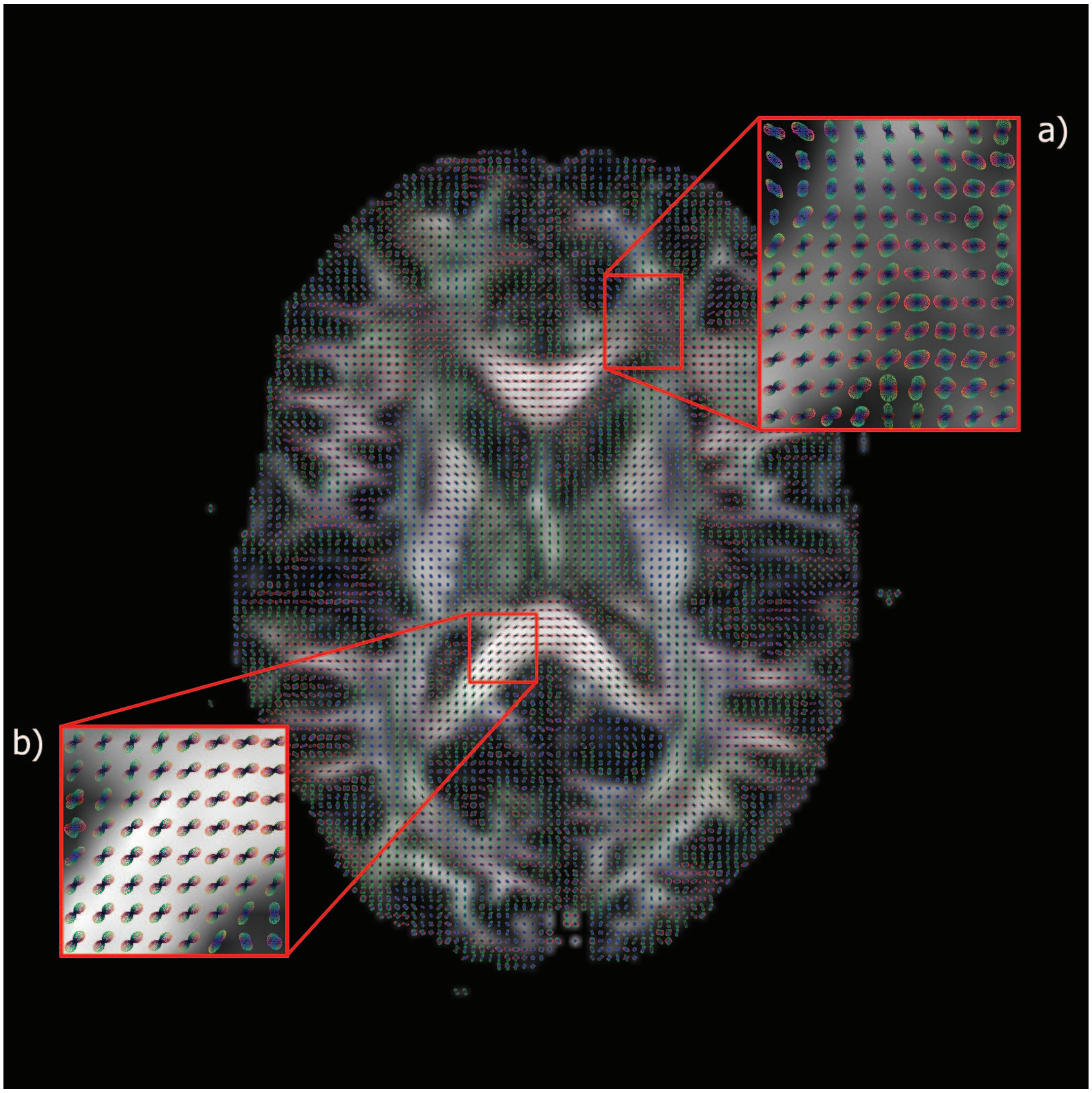

Figure 3.9: Spherical harmonic QBall dODFs in slice used in figure 3.4. The dODFs are overlaid on a standard FA map. The regions of interest show dODFs for the same crossing-fibre region (a) and single-fibre region (b) in figure 3.4.

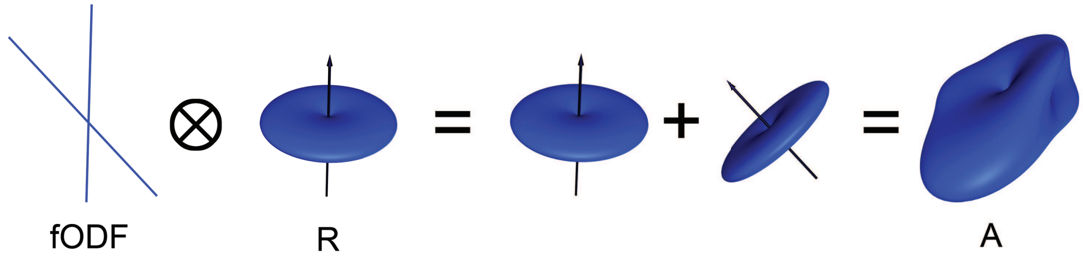

Figure 3.10: Spherical Deconvolution. The response function R convolved with the fODF, f, gives the observed A. In the simple example, the convolution becomes a sum for two directions as f is zero for all others.

al [75]. Alexander [69] shows in simulation that, at SNR=16 with 54 gradient directions, QBall gives best performance with b in the range $2000 - 2500\,\mathrm{s\,mm^{-2}}$. At these settings the method resolves two-fibre crossings consistently if the separation angle is 85° or above. The method requires an increase in SNR to 24 or gradient directions to 100 to resolve three orthogonal fibres consistently.

3.4.3 Spherical Deconvolution

Spherical Deconvolution (SD) was originally proposed by Anderson [76] and independently by Tournier et al [77] to recover the fODF directly, rather than some other function with similar structure. The key idea is to consider the set of measurements as the sum of measurements we would get from a fibre population with each orientation weighted by the fraction of fibres with that orientation. Mathematically, each measurement is then a convolution of the measurements $R(\mathbf{q};\hat{\mathbf{x}})$ for a single fibre population with orientation $\hat{\mathbf{x}}$ with the fODF, f,

$$A(\mathbf{q}) = \int f(\hat{\mathbf{x}})R(\mathbf{q};\hat{\mathbf{x}})\mathrm{d}\hat{\mathbf{x}}, \tag{3.7}$$

where f is the fibre orientation distribution. Figure 3.10 shows a simple example for a voxel containing fibres with two orientations only. In the example, f is non-zero in only two orientations, so A is the sum of R rotated for each of those orientations. In general, however, A will contain contributions for R rotated to all directions $\hat{\mathbf{x}}$.

Spherical Deconvolution aims to recover f by deconvolving the measurements with R. The procedure requires a model for diffusion in a fibre population to obtain R. Reference [76] models diffusion within fibres in a similar way to Behrens' ball and stick model (see section 3.3.2), i.e., p is a Gaussian but water molecules move only in the fibre direction. With this model, $R(\mathbf{q};\hat{\mathbf{x}}) = \exp(-td(\mathbf{q}\cdot\hat{\mathbf{x}})^2)$, where t is the diffusion time and d is the diffusivity. Tournier et al [77] derive their response function directly from brain data by calculating the average signal from the most anisotropic voxels. With a model for the response function, the deconvolution step reduces to a single matrix multiplication if we use a linear basis to represent f. Appendix C outlines a general implementation for any linear basis.

3.4.3.1 Limitations and Refinements

A major limitation of Spherical Deconvolution [59, 50] is its susceptibility to noise, which often results in spurious peaks in the recovered fODF. Figure 3.11 illustrates this problem. Each panel in the figure shows an fODF recovered from data synthesized from the ideal fODF in figure 3.10 after adding a small amount of noise (SNR=20 at $b = 0$). The first panel in figure 3.11 shows the fODF using the basic algorithm in appendix C. Several regularization techniques have been developed to avoid the spurious peaks in the fODF that the basic algorithm produces. Tournier's original method [77] uses low-pass filtering by downweighting higher-order terms in the spherical harmonic representation of f. This reduces spurious peaks, but also reduces angular resolution, see figures 3.11 and 3.12b. More recent versions [78] use Tikhonov regularization [79], which removes spurious peaks and negative lobes in f while retaining high angular resolution (figure 3.11, panel 3). The technique is referred to as Constrained Spherical Deconvolution (CSD) or, if the fODF is over-defined, super-resolved CSD. Alexander [16] uses a maximum entropy representation for f that is naturally positive definite; see next section.

Figure 3.12 shows reconstructed fODFs using no filtering (3.12a), low-pass filtering (3.12b), and super-resolved CSD (3.12c). The unfiltered algorithm output is very noisy; the regularizations to produce more reasonable fODFs. In particular, super-resolved CSD produces FODs with sharp peaks and appears to have a good angular resolution.

Another limitation is the assumption that R is the same for all fibre populations. However, fibre-populations have different cell sizes, densities, permeability and packing configurations. Recent advances [60, 80] relax this assumption to some extent.

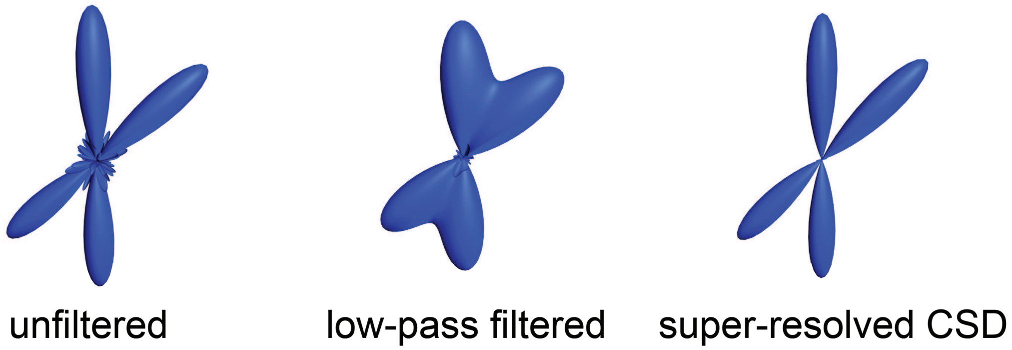

Figure 3.11: Examples of the output of various Spherical Deconvolution algorithms. The unfiltered fODF has many spurious peaks. Downweighting high-order terms in the spherical harmonic basis reduces spurious peaks at the cost of angular resolution (centre). Super-resolution CSD (right) avoids spurious peaks while retaining angular resolution.

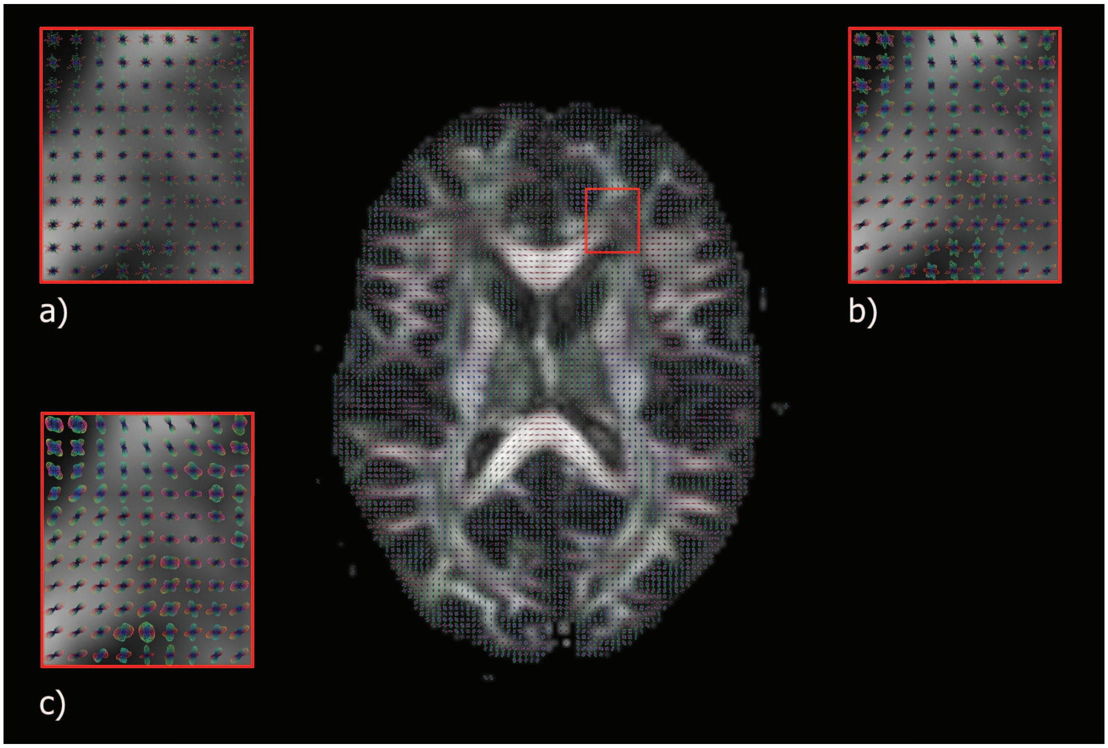

Figure 3.12: Spherical Deconvolution fODFs in the slice used in figure 3.4 using a) no regularization, b) low-pass filtering, c) super-resolution CSD. The main image shows fODFs from super-resolved cSD.

3.4.3.2 Acquisition Requirements

Tournier et al [77] use 60 gradient directions with $b = 3000\,\mathrm{s\,mm^{-2}}$, an SNR of 30 and NEX of 3. Simulations show that Spherical Deconvolution can resolve crossings at angles down to 40° with these settings although consistency is not clear. On phantom data [74] with 80 directions, $b = 4000\,\mathrm{s\,mm^{-2}}$ and SNR of 95, super-constrained Spherical Deconvolution resolves 30° crossings consistently.

3.4.4 Persistent Angular Structure (PAS) MRI

Jansons and Alexander's PASMRI algorithm [15] computes yet another function of the sphere called the persistent angular structure (PAS), which, like the dODF or DOT, is a projection of p onto the sphere designed to have similar structure to the fODF. The idea behind the PAS is to find a function that captures the angular structure of p that persists in all contours. Formally, the PAS is the function $\tilde{p}$ of the sphere that, when embedded in three-dimensional space on a sphere of radius r, has a Fourier transform that best fits the normalized measurements.

In the original algorithm, Jansons and Alexander derive a maximum entropy parameterization of $\tilde{p}$:

$$\tilde{p}(\hat{\mathbf{x}}) = \exp\left(\lambda_0 + \sum_{j=1}^{N} \lambda_j \cos(r\mathbf{q}_j \cdot \hat{\mathbf{x}})\right), \tag{3.8}$$

where the parameter r controls the smoothness of $\tilde{p}$ and a non-linear optimization fits the parameters λ_j, $j = 0, ..., N$ to fit $\tilde{p}$ to the measurements. This parametrization provides a representation for the PAS function that is optimal in the sense that it imposes the least information of its own on the recovered estimate. Alternative implementations [16, 19] replace the maximum entropy representation with more familiar linear basis representations such as spherical harmonics. Although linear bases make recovering the PAS much quicker, they are less able to capture its true shape. In particular, the maximum entropy representation is naturally positive definite, like $\tilde{p}$ and the fODF, and can represent very spiky functions that smooth linear bases cannot.

Figure 3.13 shows the recovered PAS in each voxel of the same brain slice used previously. The PAS functions have much sharper peaks and appear more consistent with each other in fibre-crossing regions (figure 3.13a) than the output of other methods we have covered. However, the computation time for the algorithm is significantly

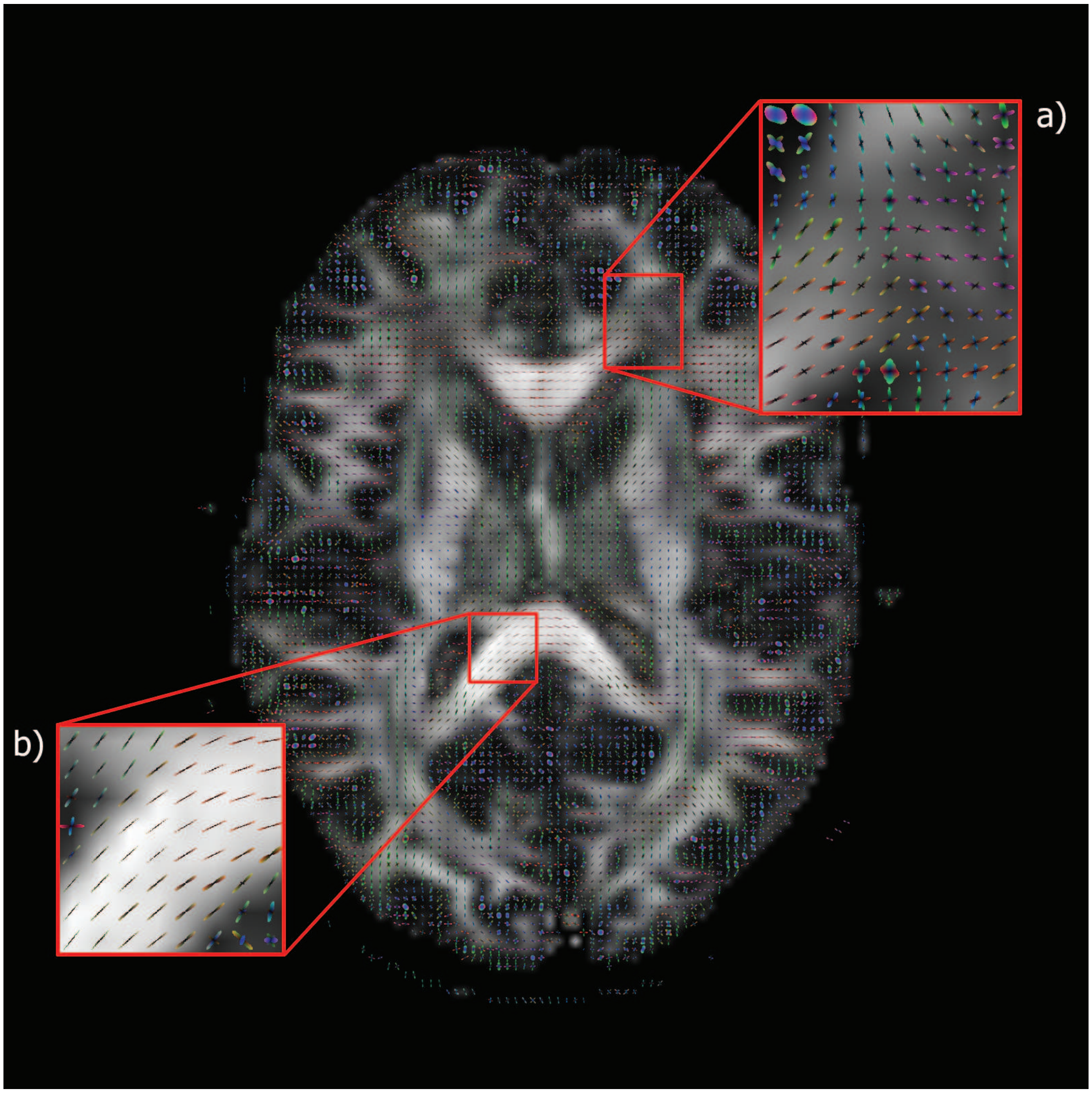

Figure 3.13: PASMRI on the slice used in figure 3.4. The regions of interest show the reconstructions for the same crossing-fibre region (a) and single-fibre region (b) in figure 3.4.

higher.

3.4.4.1 Limitations and Refinements

Like the dODF or DOT, the PAS is a property of p rather than the true fODF. Furthermore, in common with those methods, the precise relationship between $\tilde{p}$ and the fODF is unclear. Spherical Deconvolution methods have a theoretical advantage that their output relates directly to the fODF, which is the quantity of interest. However, [16, 19] show theoretical similarities between PASMRI and Sperical Deconvolution. In particular, the PAS is simply a deconvolution using the response function $R(\mathbf{q}; \hat{\mathbf{x}}) = r^{-2} \cos(r\mathbf{q} \cdot \hat{\mathbf{x}})$. We can replace the maximum entropy parameterization of θ with a linear basis to recover a linear representation of the PAS using exactly the deconvolution implementation in Appendix C. More interestingly, we can implement Spherical Deconvolution using the maximum entropy representation developed for PASMRI, as in [16]. Although the maximum entropy representation increases the computation time of Spherical Deconvolution considerably, it allows recovered fODFs to be guaranteed positive and have very spiky shapes with the potential to better capture the true fODF of coherent white-matter.

Non-linear optimization and numerical integration make the PASMRI algorithm much slower than deconvolution and QBall as implemented above [69]. However, recent work [81] optimizes the PASMRI algorithm to produce dramatic reductions in computation time that make the procedure more manageable.

3.4.4.2 Acquisition Requirements

Alexander [69] shows in simulation that at SNR=16 with 54 gradient directions, PASMRI gives the best performance when b is in the range $1500 - 2000\,\mathrm{s\,mm^{-2}}$. With these settings the method resolves two-fibre crossings consistently if the separation angle is 60° or above. The method recovers two or three orthogonal crossings consistently with the number of gradient directions as low as 30 at SNR=16.

3.5 Derived Information

The methods in section 3.4 output spherical functions that can be used directly for qualitative analysis but require further processing to extract useful quantitative information. This section outlines techniques for extracting useful information from these spherical functions. The section starts with general methods for estimating peak directions. It goes on to describe broad scalar indices of shape, such as Generalized Fractional Anisotropy, and measures of peak curvature that may give further insight into the true white-matter architecture.

3.5.1 Principal Directions

The peaks of the fODF provide estimates of the dominant fibre orientations. Most representations of spherical functions, i.e. linear bases such as spherical harmonics or radial basis functions or non-linear representations such as eqn.(3.8), do not have general analytical expressions for peak directions so we have to search for peaks numerically. Jansons and Alexander's algorithm [15] samples the spherical function in each of a large number of evenly distributed directions and identifies locally maximal samples, i.e. those that are greater than any other samples within a 'search radius'. They use a Newton method to refine the exact positions of each local maximum and finally discard duplicates. Haroon et al [48] speed up the process by fitting a quadratic surface local to each maximum which provides an analytic approximation.

Numerical search for peak directions is computationally expensive and typically depends linearly on the number of parameters in the representation of the spherical function. For fast linear methods like QBall and Spherical Deconvolution, computation for peak finding can be orders of magnitude greater than the initial reconstruction. More recently, Bloy et al [82] provide an analytic expression for peak directions of spherical functions represented as symmetric tensors (equivalent to spherical harmonics), although the approach is not practical for high orders.

3.5.2 Generalized Fractional Anisotropy

In [67], Tuch defines the Generalized Fractional Anisotropy (GFA) as an analogue for QBall of the FA in DTI. The FA is a measure of variation of the DT eigenvalues that is independent of their magnitude. In a similar way, the GFA is a measure of variation of the dODF, ϕ. Mathematically,

$$GFA = \left[\frac{\int(\phi(\hat{\mathbf{x}}) - \bar{\phi})^2 \mathrm{d}\hat{\mathbf{x}}}{\int \phi(\hat{\mathbf{x}})^2 \mathrm{d}\hat{\mathbf{x}}}\right]^{\frac{1}{2}}, \tag{3.9}$$

where $\bar{\phi} = (4\pi)^{-1}\int \phi(\hat{\mathbf{x}})\mathrm{d}\hat{\mathbf{x}}$. The definition extends to any other function of the sphere and we can compute the GFA of any fODF, PAS, uODF, etc in exactly the same way.

In fact, Tuch [67] provides a discrete version of Eqn. 3.9 that works with samples of ϕ, but the continuous version above is more generally useful, since some of the integrals are often analytic, particularly for functions represented using spherical harmonics.

Higher-order moments are also possible,

$$M_n = \left[\frac{\int (\phi(\hat{\mathbf{x}}) - \bar{\phi})^n \mathrm{d}\hat{\mathbf{x}}}{\int \phi(\hat{\mathbf{x}})^n \mathrm{d}\hat{\mathbf{x}}} \right]^{\frac{1}{n}}, \tag{3.10}$$

and the Camino toolkit [83] implements generalized skewness (M_3) and kurtosis (M_4). Higher-order moments may provide other useful information that is complimentary to the fractional anisotropy and reflect features of the fibre configuration that the GFA is insensitive to, although no exploration of this idea is in the current literature. For example, M_3 provides an analogue of the DT skewness (see chapter 3).

3.5.3 Peak Hessians and Peak Sharpness

It is a mistake to assume that the output of any of the methods in section 3.4 gives an exact reconstruction of the fODF. For some algorithms, the difference is explicit, since, as we have seen, the dODF and fODF are different quantities. Even for spherical deconvolution methods however, several factors cause departures of the reconstructed fODF from the true fODF: Choice of linear basis or representation affect the recovered shape, models of R simplify processes in brain tissue and noise, smoothing and regularization add further artefacts.

How well different reconstructed functions reflect the true fODF remains an open question. Peak directions appear to correspond within known fibre directions. Furthermore, we tend to observe different peak shapes in regions with different configurations. In particular, as noted in section 3.2, fanning and bending configurations can produce paddle-shaped peaks with an anisotropic cross-section.

The Hessian, or matrix of second partial-derivatives, describes the curvature of a function. The trace of the Hessian provides a measure of peak sharpness. Parker and Alexander [10] show that the sharpness of the ODF peaks reflect the uncertainty of the fibre orientation estimates and may provide information about the dispersion of fibres within the image voxel. In [10], the Hessian is computed numerically by evaluating the spherical function at slightly displaced positions in two locally orthogonal directions.

3.6 Evaluation and Comparison of Multiple-Fibre Algorithms

This section outlines the main comparisons of the algorithms described in the previous sections to date. The section starts with an overview of typical metrics used to evaluate the performance of reconstruction techniques. We then give an overview of the validation of each method and comparisons between reconstruction techniques.

3.6.1 Validation Methods

There are several methods available for comparing reconstruction algorithms. The following methods are commonly used:

- Qualitative assessment reveals regions where algorithms produce sensible results corresponding to anatomical knowledge and where they do not, but is limited by current knowledge and does not provide quantitative measures for comparison and optimization.

- High quality datasets obtained under special conditions not achievable routinely (e.g. long acquisition times) can provide a ground-truth against which to study the effects of increased noise or reduced image resolution or sampling on algorithm performance. This approach does not highlight fundamental limitations of algorithms that also affects results from high quality data.

- Synthetic data from simple models, such as mixtures of Gaussians, more complex biophysical models (e.g. [84, 85]), or numerical simulations of the diffusion process [86, 87, 88]. In synthetic data, the quantities we aim to recover, such as fibre directions, are known, although the models often over simplify brain tissue and the imaging process.

- Scanner data from physical phantoms, constructed from materials such as glass or polymers, e.g. [75], are also useful, but again do not reflect the full complexity of brain tissue.

3.6.2 Statistics for Validation and Comparisons

In diffusion MRI, we are often interested in being able to accurately and consistently recover the orientations of the dominant white-matter populations in each voxel. Various metrics are used to assess the performance of the reconstruction algorithms within this task. Here, we introduce some of the common metrics and techniques and discuss the requirements for each.

3.6.2.1 Statistics that do not Require a Ground-Truth

The direction concentration [57] measures the precision of the fibre-orientation estimates from reconstruction algorithm. To compute the direction concentration, we require a set of estimates of a direction, but do not require knowledge of the true direction. The set of estimates may come from repeated trials on synthetic data with different noise realizations, as in [57], or from a statistical procedure such as bootstrapping (see section 3.6.3, box 3.6.3). The direction concentration is

$$\gamma = -\log(1 - \kappa_1), \tag{3.11}$$

where κ_1 is the largest eigenvalue of the mean dyadic tensor $\mathbf{Y} = m^{-1} \sum_{i=1}^{m} \mathbf{e}_i \mathbf{e}_i^T$, where $\mathbf{e}_i$, $i = 1, ..., m$ is a collection of directions. A high value of γ indicates that the estimates are tightly clustered around the mean, whereas a low value indicates that the estimates vary more widely.

A related dispersion statistic is the “95% cone of uncertainty” [89] also measures the precision of the reconstruction. This metric uses a population of fibre-orientation estimates in a given voxel to calculate the angle at the vertex of the cone containing 95% of the estimates. This uncertainty is visualized as a cone containing 95% of the fibre-orientation estimates.

3.6.2.2 Statistics that Require a Ground-Truth

In this section we define metrics that require a ground truth. The ground truth can be obtained in several ways. For example, some features of the ground truth, such as fibre orientation, are often known when using a synthetic (numerical) model of diffusion or a physical phantom. Alternatively, the ground truth can be approximated to some extent by a acquiring a very high quality dataset. The measures are then calculated using a subset of the data that is of comparable quality to clinical data.

The angle bias is a measure of accuracy. The true fibre-orientation must be known and a set of estimates must be available, so the measure is generally limited to synthetic data trials or by comparison with estimates from high quality daya. The angle bias is

$$\alpha = \cos^{-1}(\mu \cdot \mathbf{n}), \tag{3.12}$$

which is the difference between the mean μ fibre-orientation estimate and the true fibre orientation $\mathbf{n}$. More specifically μ is the principal eigenvector of the mean dyadic tensor, $\mathbf{Y}$, and $\mathbf{n}$ is the true fibre orientation. A small angle bias indicates that the fibre-orientation estimate is close, on average, to the true fibre-orientation.

Another measure is the consistency fraction [16], which measures how often an algorithm identifies the right number of directions with approximately the right orientations. The number of fibre directions must be known, so the measure is generally limited to synthetic data trials or by comparison with estimates from high quality data. A reconstruction is consistent if:

- The number of estimated directions is the same as the number of true directions.
- The estimated directions match the true directions to within a given tolerance (for example, $\cos^{-1}(0.95)$).

The Kullback-Leiber (KL) Divergence [90] measures the divergence between two distributions and may be used to give a more complete comparison of two spherical functions, as in [67], than just comparing their peak directions. Specifically, the KL divergence of a function ϕ to a reference function ϕ_r is

$$KL(\phi_r, \phi) = \int \phi_r(\hat{\mathbf{x}})(\log \phi_r(\hat{\mathbf{x}}) - \log \phi(\hat{\mathbf{x}}))\mathrm{d}\hat{\mathbf{x}}. \tag{3.13}$$

This measure assumes that the reference function is a gold-standard and that any deviation from this is due to unwanted noise or artefacts in the reconstruction.

3.6.3 Validation of Spherical Deconvolution

In [91], Tournier et al estimate the 95% cone of uncertainty for reconstructions from their spherical harmonic implementation of Spherical Deconvolution using the bootstrap method (see box 3.6.3) and compare the results to those from DTI. The results show that DTI has a significantly higher precision where voxels contain a single fibre population. Spherical Deconvolution shows multiple peaks in the expected directions in some crossing-fibre regions.

3.6.3 - Bootstrap: The bootstrap technique [92] creates a large number of samples from a smaller dataset to improve statistics. The standard method requires multiple acquisitions of the signal of each measurement. To create a new sample, one of each of the measurement is drawn at random from the set of repeats to provide a new combination. Related techniques, such as wild bootstrap [49, 93] and residual bootstrap [93, 45], only require only a single acquisition.

In [94], Tournier et al show qualitatively that there are less spurious peaks in the FODs from their entropy-minimized algorithm than those from their original algorithm. They evaluate their optimization of the response function using entropy-minimization by comparing it to results where the parameters were set empirically.

In [78], Tournier et al optimize their CSD algorithm using synthetic data. They show that CSD gives better angular resolution than the original spherical deconvolution algorithm and that the non-negativity constraint does not introduce a bias into the results. They also use bootstrap data to estimate the 95% cone of uncertainty of CSD and super-CSD and compare the results to those of the original algorithm. They show that CSD is more precise than the original implementation of spherical deconvolution, especially where the crossing angles of the fibres is small. However, the optimal choice of maximum order of spherical harmonic to use to represent the FODs from CSD varies with the intersection angle, volume fraction, etc.

Tournier et al [95] compare CSD to their entropy minimization regularisation and QBall. They perform a qualitative validation using a region of interest in the region of the arcuate fasciculus. They show that their Tikhonov regularization produces FODs with sharper peaks than those generated using their entropy minimization procedure. In [96], they perform a quantitative comparison of their constrained spherical deconvolution algorithm to QBall using the phantom model of Lin et al [75]. At $b = 3500\,\mathrm{s\,mm^{-2}}$, Tournier et al's method was capable of resolving crossing fibres where the crossing angle is 30^o, whereas the QBall algorithm was only able to successfully resolve the two directions in 30% of the voxels and the direction estimates from ODF peaks had a significantly higher bias than those from from FOD peaks.

Dell'Aqua's method [97] has an extra parameter that has a significant effect on the output. In [97], Dell'Aqua et al show the effects of altering the optimization parameter of their method against SNR using synthetic data. They conclude that there is a trade-off between optimization parameter setting and the SNR of the data, and that the value of the optimization parameter must be chosen on a case by case basis.

Sakaie and Lowe [98] compare their Damped Singular Value Decomposition regularisation algorithm to Tournier's low-pass filtering [77] and minimum entropy [94] methods. They show that their method has a smaller error angle than the other regularizations at low SNR. They compare the methods quantitatively using synthetic data and qualitatively on human brain data.

3.6.4 Optimization of PAS-MRI and comparisons with other methods

In [15], Jansons et al optimize the PAS-MRI algorithm using synthetic datasets. They show that when the angular structure is weak (for example, in grey-matter), the PAS has many spurious peaks caused by noise. When the angular structure is strong, the noise has much less affect on the PAS. They demonstrate that PASMRI can resolve orthogonal crossing fibres at SNR=16, which is typical of in-vivo human brain data.

Alexander [16] shows that PASMRI compares favourably to maximum entropy spherical deconvolution (MESD), by having a much higher consistency fraction in synthetic data trials. The experiments show that both non-linear PASMRI and Spherical Deconvolution are consistently better than a linear implementation of Spherical Deconvolution. In [99], Alexander et al compare QBall to PAS-MRI using synthetic datasets. They show that PASMRI provides higher consistency fractions than QBall at fixed SNR.

3.6.5 Comparisons of QBall with other Reconstruction Algorithms

Qualitative results in [64, 68] show good agreement between QBall and DSI in a fibre-crossing region in the human brain. However, these results come from high-quality test data from a spherical acquisition scheme with 492 gradient directions, which requires similar acquisition time to DSI.

Tuch [67] optimizes QBall by finding the width of the basis function σ which minimizes the condition number of the interpolation matrix, $\mathbf{Y}$. He also calculates the angle bias and KL divergence for QBall reconstructions of synthetic data and provides a qualitative evaluation of the performance of QBall using brain data to show that the method produces sensible results.

In [70], Hess et al show that ODFs from their Spherical Harmonic implementation of QBall broadly agree with those from Tuch's original implementation. They compare the implementations qualitatively using a whole-brain dataset. However, the comparison uses a large number of diffusion encoding directions and the precision of each method was not measured.

3.6.6 Other Evaluations and Comparisons

In [100], Kuo et al attempt to find the optimal acquisition scheme for DSI. They acquire a high-quality dataset with 925 values of $\mathbf{q}$, which they subsample to produce datasets with 691, 515 and 203 values of $\mathbf{q}$. They perform tractography on the reconstructions and compare the similarity of the resulting tracts with those from the full dataset. They show that at least 515 samples are necessary, otherwise the results of the method become significantly different from the reference. Furthermore, they compare two types of sub-sampled datasets with the reference. They find that datasets with the same maximum $|\mathbf{q}|$ as the full dataset, but reduced spacing are more similar to the reference than those with the same spacing but reduced maximum $|\mathbf{q}|$.

Lin et al [75] evaluate how well their method approximates the ODF by comparing it to DSI using data acquired from their phantom. They show that although the accuracy and precision of their approximations of the ODF are not as good as those from DSI, their method offers a significant reduction in acquisition time.

Özarslan et al's [101] generalized diffusion tensor imaging method is studied using both synthetic data and data acquired from a rat brain. They show qualitatively that their method produces reasonable results using both the synthetic data and brain data. However, no quantitative validation or comparison has been performed using this method.

Lui et al [102] perform a qualitative evaluation of their method using images acquired from four numerical phantoms. They visualize probability density function isosurface and skewness maps. The shapes of the functions reflect the known orientations of the phantoms.

3.6.7 Summary

Table 3.6.7 (below) provides a summary of the pros and cons of each method.

Method	Acquisition requirement	Computation time	Accuracy	Bias
Two Tensor	low/medium	medium	medium	low
Ball and Stick	low	medium	medium	low
PASMRI	medium	high	high	low
SD (low-pass filtered)	medium	low (peak finding medium)	medium	medium
SD (cSD)	medium	medium	medium	low
DSI	very high	medium	high	medium
QBall	medium/high	low (peak finding medium)	medium/low	high
DOT	medium/high	medium	medium	low

Table 3.1: Summary of acquisition requirements and computation times for the multiple-fibre reconstruction algorithms

3.7 Applications and Exploitation

This section discusses applications of the models and algorithms covered earlier in this chapter. Specifically, we describe applications to tractography algorithms to allow them to exploit the extra information. The results of the tractography algorithms described below have been shown to be more consistent with known anatomy than single fibre approaches [9, 10].

3.8 Extending Tractography for Multiple-Fibre algorithms

In section 2.4 we described two main approaches to tractography: deterministic and probabilistic. In this section we show how these approaches have been extended to incorporate information from multiple-fibre reconstruction algorithms.

3.8.0.1 Extending Deterministic Tractography to Exploit Multiple-Fibre Algorithms

Several methods have been suggested for extending deterministic tractography to the multi-fibre case. Basic streamline tractography algorithms are simple to adapt to exploit multiple fibres in each voxel. The basic extension simply requires a method to choose which of the multiple directions to follow at each step. The simplest strategy [103] picks the direction that aligns most closely with the previous step. Hagmann et al [104] use the same strategy to generate streamlines from DSI data. Perrin et al [105] use the shape and peak orientation of the QBall dODFs to influence the paths of the streamlines at each step.

3.8.0.2 Generalisation of Probabilistic Tractography Algorithms to Multiple-Fibre Reconstructions

Both Parker and Alexander [43] and Cook et al [106, 107] generalize calibrated PICo to use multi-tensor models, which can improve tracking through fibre-crossings. However, this framework suffers from the limitations of the multi-tensor models such as fitting problems and the need to prespecify the number of fibres per voxel. Hosey et al [51] and Behrens et al [9] show results from combining multi-tensor models with the MCMC approach.

Parker and Alexander [10] extend calibrated PICo to exploit multiple fibre reconstruction algorithms. They use peak directions as fibre-orientation estimates, of which there may be several in each voxel. In place of the FA of the diffusion tensor, they use the sharpness of the fibre orientation distribution peak to predict the uncertainty of the estimate. Broad peaks have a high uncertainty, sharp peaks have a low uncertainty. Specifically, they compute the Hessian, or second derivative matrix, of the PAS function at each peak and use its trace as a measure of mean curvature. The uncertainty mapping is indexed using the log of the trace of the Hessian of each peak to find the variance in a Gaussian model of uncertainty. A weakness of the approach in [10] is that the Gaussian model does not account for anisotropy in the uncertainty of the fibre-orientation estimate. Anisotropy in the uncertainty occurs in regions of fanning and bending where the fibres spread out more in one direction than another.

Haroon et al [48] use the wild bootstrap algorithm to estimate the uncertainty of fibre-orientation estimates obtained using QBall. However, the residuals obtained from the QBall ODF are often very small, resulting in poor estimates of uncertainty. They present two methods, both of which use wild bootstrap method. The first method fits the QBall ODF and then estimates the diffusion signal from the ODF using a monoexponential approximation. This estimate is then compared to the measured signal to find the residuals. The second uses QBall to estimate the dominant fibre-orientations present in a voxel and then uses these estimates to constrain the fitting of a compartment model. The residuals from this mixture model are comparable to those from a standard bootstrap estimate of the uncertainty. They show that the second method is a better predictor of uncertainty than the first method, although the uncertainty estimates from this technique are not directly measured from the QBall ODF. Berman et al [108] use the residual bootstrap algorithm to obtain samples of the uODF using QBall.

Hosey et al [51] and Behrens et al [9] use multiple fibre ball and stick models (see section 3.3.2) with Markov Chain Monte Carlo (MCMC) to obtain uODF samples. However, these implementations suffer from the limitations of the over-simplified model of diffusion that they use. For example, it is unclear how the model will fit complex structures such as fannings and bendings. Fonteijn et al [109] estimate the uODF from spherical harmonic QBall dODFs using MCMC.

3.9 Summary

This chapter has reviewed the main multiple-fibre compartment models and multiple-fibre reconstruction algorithms used in diffusion MRI. Although many more exist, we have aimed to give a conceptual overview. These algorithms seek to recover the orientations of the multiple fibre populations in each voxel of an image volume. One class of algorithms, including QBall, DOT and PASMRI estimate features of the particle displacement density, p, that are spherical functions with peaks that provide fibre-orientation estimates. The aim is usually to recover the distribution of fibre orientations or fODF. However, the relationship between p and the fODF is complex and unclear. Spherical deconvolution methods estimate the fODF more directly, but rely on overly simple modelling assumptions. Outstanding issues remain in Spherical Deconvolution of what models provide the most accurate fODFs. Choice of representation of spherical functions remains an important issue, since linear representations lack flexibility and non-linear ones require long computation times. Validation also remains an important issue. Alexander [69] evaluates and compares various algorithms in simulation; Tournier et al [74] make comparisons using phantom data. All the methods in section 3.4 produce spurious peaks in isotropic regions and techniques to distinguish genuine angular structure from noise are important for proper exploitation. The various derived quantities we discuss in section 3.5 provide some robustness to noise that allows exploitation for tractography and connectivity mapping, but further work is required to refine these techniques.

We have outlined each of the methods, as well as some of the main techniques for exploiting the information they provide. Non-parametric reconstructions have the advantage of being able to recover multiple peaks in each voxel without the requiring prior knowledge of the number of fibre populations. Model-based approaches have a clearer link to the underlying microstructure due to their explicit modelling of certain features of the tissues (for example hindered and restricted compartments). If the model approximates the underlying structure well, they can provide useful insight into the microstructure and may also have higher precision.

In summary, although the multiple-fibre techniques we have discussed clearly provide additional insight beyond the basic models in diffusion MRI, extracting reliable quantitative information can be difficult. Much work remains to validate the techniques and quantify what features of their output are reliable and meaningful. Other open questions remain, such as the trade-off between image resolution or voxel size and the number of measurements we can acquire in each voxel. Increasing image resolution can avoid mixing fibre populations in single voxels so that simple models suffice. However, signal decreases as image resolution increases and partial volume effects will still occur even with very small voxels as we cannot avoid having voxels spanning tissue interfaces. As resolution decreases, the configurations within single voxels become more complex, but we can acquire more measurements with higher signal that support more complex models to separate the effects.

We mentioned fanning and bending configurations produce similar fODFs. In fact, many quite different configurations can have similar fODFs and the methods we have described are unable to distinguish them. Future methods may use more global knowledge of fibre geometry to separate these configurations, see for example [110].

Chapter 4

Optimization and Comparison of Reconstruction Algorithms

The methods described in chapter 3 each have their own advantages and disadvantages. The linear methods have the advantage of being computationally inexpensive and having modest data requirements. For this reason we will focus mainly on the linear algorithms, although we show results from several non-linear approached to provide insight into the improvement that can be gained from a more computationally heavy reconstruction algorithm. As discussed in chapter 3, the multiple-fibre reconstruction algorithms we compare have already been evaluated using varying qualities and types of data (such as synthetic data and brain data), as well different measures of accuracy and precision. Here, we propose comparing methods using a framework which consists of synthetic data that models two fibre-populations and various scoring criteria. As far as we know, this is the only comparison of the multiple-fibre methods using a standardised framework. The parameters of the reconstruction algorithms are optimized prior to any between-method comparison to ensure that the tests give a fair representation of the performance. Thus, the methods are compared on a level playing field. We optimise and compare the following linear algorithms:

- spherical harmonic QBall (SH-QBall)
- radial basis function QBall (RBF-QBall)
- linear persisent angular structure MRI (RBF-PAS)
- radial basis function spherical deconvolution (RBF-SD)

- spherical harmonic spherical deconvolution (SH-SD) with a DT response function
- spherical harmonic spherical deconvolution (SH-SD) with a ‘spike’ response function

In addition to this, we optimise and compare the following non-linear algorithms to show the potential improvements gained from using more complex reconstruction algorithms:

- constrained spherical deconvolution (CSD)
- persisent angular structure MRI (PASMRI)
- maximum entropy spherical deconvolution (MESD)

Finally, we perform a timing analysis to compare the computational demands of the algorithms using a synthetic dataset. We present the results for each algorithm in a table summarising the reconstruction time and subsequent post-processing time.

4.1 Experimental Strategy

The experiments here aim to disprove the null-hypothesis that all the linear methods perform equally well. We limit the comparisons to synthetic data that represents voxels containing two distinct fibre-populations, but the framework is straightforward to extend to include both single-fibre voxels as well as three-fibre voxels. Furthermore, we limit the quality of the datasets to approximate the quality of data that can be acquired in a clinical setting. The methods are evaluated by calculating the precision, accuracy and consistency of fibre-orientation estimates recovered from synthetic data. For each reconstruction algorithm, we perform the following steps:

- create synthetic datasets using various parameter combinations
- for each parameter setting combination of the reconstruction algorithm
    - for each dataset
        - reconstruct the data
        - find the peak directions

- find the optimal peak threshold by calculating the mean consistency fraction over all datasets for each peak threshold setting.

- calculate all metrics at optimal settings

The details of the procedure above are given in the remainder of this section.

4.1.1 Synthetic Data

We generate synthetic data using a two-tensor model of diffusion. By varying the parameters of the tensor model, we can generate a range of crossing fibre configurations on which to test the reconstruction algorithms. For this experiment we generate data using 45 different combinations of the two-tensor model. Each parameter combination is used to generate a dataset consisting of 144 voxels containing diffusion measurements synthesized from the model. Specifically, we generate data using the test function. Specifically, we generate data using the test function

$$p(\mathbf{x}) = aG(\mathbf{x};\mathbf{D}_1,t) + (1-a)R_\theta^T G(\mathbf{x},\mathbf{D}_2,t)R_\theta \tag{4.1}$$

where a is a mixing parameter, $G(\mathbf{x};\mathbf{D},t)$ is a zero mean Gaussian with covariance $2t\mathbf{D}$, $\mathbf{D}_1 = diag(\lambda_1,\lambda_2,\lambda_2)$, $\mathbf{D}_2 = diag(\lambda_2,\lambda_1,\lambda_2)$ and R_θ is a rotation by θ about the z-axis. Each dataset uses a single parameter combination from $\lambda_1 \in \{1.9, 1.5, 1.1\} \times 10^{-9}\,\mathrm{m}^2\,\mathrm{s}^{-1}$, $a \in \{0.5, 0.6, 0.7\}$ and $\theta \in \{0^\circ, 10^\circ, 20^\circ, 30^\circ, 40^\circ\}$. In all of the datasets $\lambda_1 + \lambda_2 = 2.1 \times 10^{-9}\,\mathrm{m}^2\,\mathrm{s}^{-1}$. The fractional anisotropy of the diffusion tensors, $\mathbf{D}$, are 0.94, 0.77 and 0.46 respectively. The parameter settings are chosen such that all of the algorithms will fail to consistently recover both fibre orientations for at least some of the datasets. A random rotation is applied to the test function prior to the estimation of the diffusion-weighted measurements to remove any potential directional bias caused by acquisition scheme. The data is synthesized by sampling the Fourier transform of p, using eqn 2.4, at each wavenumber in a spherical acquisition scheme with 60 gradient directions and $b = 1200\,\mathrm{s}\,\mathrm{mm}^{-2}$. The settings of the acquisition scheme are chosen so that the data is of similar quality to data that can be acquired clinically. The distribution of noise in MR data is Rician [111]. Therefore, noise is added to the measurements as random complex numbers with independent real and imaginary parts drawn from $N(0,\epsilon^2)$, where $\epsilon = F(0)/S$, F is the Fourier transform of p at each wavenumber, S is the signal to noise ratio (SNR) at $b = 0$. We then take the modulus to get the synthetic measurement. The data generated uses $S = 20$, which is typical of diffusion MRI data.

The parameters of the test functions have been chosen such that all the methods would fail to reconstruct at least some of the test functions, whether it be due to a limited angular resolution of the method or an inability to reconstruct a secondary peak with a very small volume fraction.

4.1.2 Processing

We use the peak finding method of Jansons and Alexander [15] (see section 3.5.1) to recover the fibre-orientation estimates from the ODF for each voxel. In addition to the peaks that correspond to fibre-populations, there are also spurious peaks that result from noise in the data. The fibre-orientation estimates that correspond to these spurious peaks do not contain useful information and must be removed. This is achieved by setting a threshold on the peak magnitude. The amount of peak-thresholding required to remove spurious peaks varies from algorithm to algorithm. For example, QBall dODFs are very smooth and have a few small spurious peaks. Therefore, QBall dODFs tend to require a threshold that removes only the smallest peaks; conversely, spherical deconvolution produces spiky fODFs which contain many large spurious peaks and therefore needs a much larger threshold. To find the optimal peak-culling thresholds for each algorithm we vary the thresholding parameters to maximize $\bar{c}$. Specifically, we remove peaks where

$$m > (q * g + w * h), \tag{4.2}$$

where m is the magnitude of the peak,

$$q = \frac{1}{4\pi} \int_{|x|=1} f(x) dx \tag{4.3}$$

is the mean magnitude of the ODF,

$$w = \frac{1}{4\pi} \int_{|x|=1} (f(x) - q)^2 dx \tag{4.4}$$

is the number of standards deviations of the magnitudes over the ODF and g and h are tuneable parameters.

Prior to comparing the algorithms, we optimize the methods with regard to their parameters. This involves varying the parameters of each method to maximize the consistency fraction (section 3.6.2). To simplify the search, we use the mean consistency fraction $\bar{c}$ over all 45 datasets. We discuss the metrics used in more detail in the following section.

4.1.3 Metrics

To assess the performance of each algorithm, we compute the angle bias, α, direction concentration,γ, and consistency fraction, c, of the estimated fibre-orientations over a large number of trials. Details of how each metric are calculated are given in section 3.6.2. We primarily use the consistency fraction for our analysis, since it looks at both the accuracy and precision of the reconstruction. However, the metric only tests whether the reconstruction provides the correct number of fibre-orientation estimates and whether they are within a given tolerance. In a case where one algorithm has a high accuracy but the other is just within the tolerance, the consistency fraction will assign an equal score to both. Therefore, we also look at the angle bias (accuracy) and direction concentration (precision) of the fibre-orientation estimates separately to provide further insight into the performance of the algorithms.

In addition to the metrics described above, we also compute the mean consistency fraction, $\bar{c}$, which is the average of the consistency fractions for all 45 datasets at one parameter setting of the reconstruction algorithm. We maximize $\bar{c}$ when optimizing the parameters of each reconstruction algorithm and when searching for the optimal peak thresholding settings.

4.2 Experiment 1 - Comparison of SH-QBall and RBF-QBall

In this section we compare the Tuch's original QBall implementation (RBF-QBall) [67, 68] to the Spherical Harmonic implementation (SH-QBall) [70].

4.2.1 Method

SH-QBall has a single parameter to vary, the order of the spherical harmonic, which we alter in the range $\{4, 6, 8\}$. The range is set such that the dODF has enough parameters to be able to reconstruct multiple peaks without having more free parameters than the number of gradient directions. Specifically, spherical harmonic representation with a maximum order of 8 has 45 parameters, which less than the 60 unique diffusion-weighted measurements in our acquisition; increasing the maximum order further will result in having more parameters than measurements. Conversely, dODFs with a maximum order below 4 will not be able to represent crossing fibres. See appendix A for details on the implementation of spherical harmonics.

The implementation of RBF-QBall uses two sets of radial basis functions (details of the QBall implementation are given in appendix B). Each set of radial basis functions has two parameters, the number of basis function centres and the width of the basis functions, σ. We use the first set of radial basis functions,

$$A(\mathbf{q}) = \sum_{j=1}^{J} \xi_j \psi_j(q), \tag{4.5}$$

where ξ_j is the weight of the j-th basis function ψ_j, to model the data. We fix the number of basis function centres J to be the same as the number of gradient directions in the acquisition. The second set of radial basis functions,

$$\phi(\hat{\mathbf{x}}) = \sum_{k=1}^{K} \beta_k \theta_k(\hat{\mathbf{x}}), \tag{4.6}$$

where β_k is the weight of the k-th basis function θ_k,represents the reconstructed dODF. We use $K = \{42, 80, 120, 246, 755\}$ basis functions to represent the dODF. We vary the width of both sets of radial basis functions independently in the range $\sigma \in [3°, 27°]$.

In addition to the parameters of each variant of QBall, we also maximize $\bar{c}$ over the threshold parameters, g and h. We select a discrete set of values for both parameter such that $g \in [0, 1.5]$ and $h \in [0, 8]$.

4.2.2 Results

We observe that varying the maximum order of spherical harmonic basis in the range $\{4, 6, 8\}$ has no significant effect on the mean consistency fraction, $\bar{c}$. Therefore we use a maximum spherical harmonic order of 6, which is in agreement with other work, such as [70]. For SH-QBall with a maximum spherical harmonic order of 6, $\bar{c}$ is maximized when the threshold settings are $g = 1$ and $h = 0$. However, the increase in $\bar{c}$ attained by thresholding the QBall dODFs is negligible (see figure 4.1). In this experiment we apply the peak thresholds for completeness. The settings that maximize $\bar{c}$ for spherical harmonic QBall are: maximum spherical harmonic order 6, $g = 1$ and $h = 0$. At these settings $\bar{c} = 0.27$.

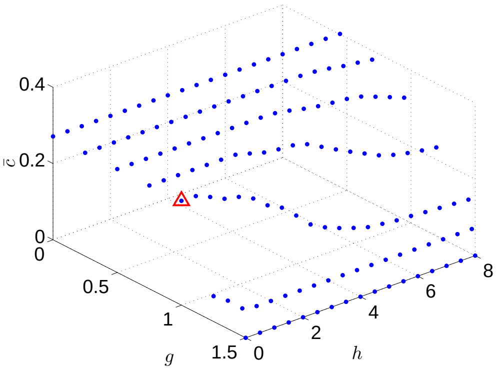

Figure 4.1: Plot of mean consistency fraction, $\bar{c}$, against peak threshold parameters g and h for SH-QBall. The threshold removes peaks with $m > (q * g + w * h)$, where q is the mean magnitude of the ODF and w is the number of standards deviations of the magnitudes over the ODF. The combination of g and h that maximize $\bar{c}$ is indicated with a red triangle.

Figure 4.2 plots the consistency fraction (c), angle bias (α) and direction concentration (γ) for all datasets at the optimal reconstruction settings for SH-QBall. We will refer to this type of plot as a "tile plot". In this figure, a separate tile is shown for each dataset and there are separate panels of tiles for c, γ and α. The lighter the colour of the tile, the better the performance of the reconstruction algorithm with regard to the corresponding metric. For SH-QBall, the reconstructions have a high consistency fraction for orthogonal crossings where both tensors have $\lambda_1 = 1.9 \times 10^{-9}$ (top left panel). However, SH-QBall fails to consistently recover fibre-crossings for many of the synthetic data configurations. In particular, the technique is unable to recover fibre crossings when the fibre populations cross at $\theta > 20^\circ$, so the tiles for these datasets are black. The angle bias, α, (centre row) of SH-QBall reconstructions is less than 5° for all datasets where $\theta \leq 20^\circ$ and $\lambda_1 \geq 1.5 \times 10^{-9}\,\mathrm{m}^2\,\mathrm{s}^{-1}$. This suggests that when multiple peaks are recovered by the dODF, the bias in the estimates of fibre orientations is small. In contrast, the direction concentration is only high for datasets where $m \in \{0.5, 0.6\}$ and $\lambda_1 = 1.9 \times 10^{-9}$ or $\theta = 20^\circ$ and $\lambda_1 = 1.9 \times 10^{-9}$ (bottom row, left panel). The direction concentration is low for all other datasets, which suggests that there is a lot of uncertainty in the fibre-orientation estimates. The full table of results showing the numerical data underlying figure 4.2 is given in appendix F.1.

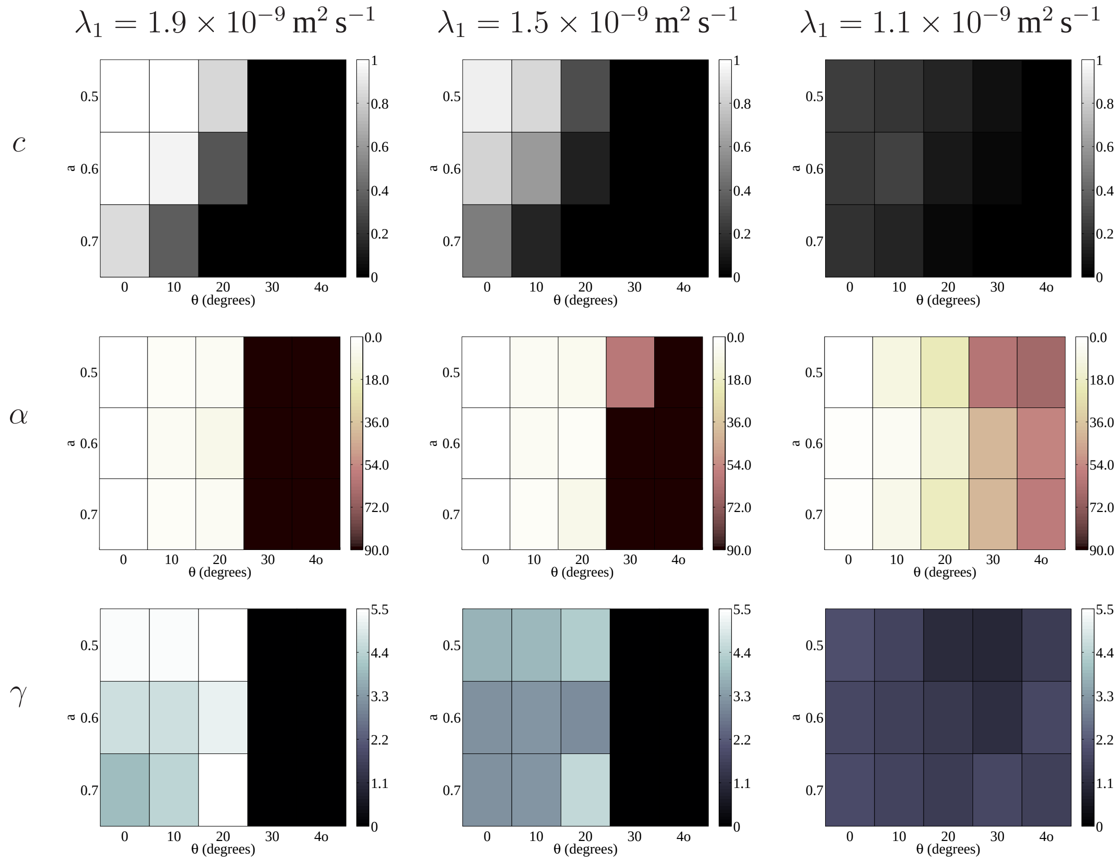

Figure 4.2: Tile plot for SH-QBall reconstructions showing c (gray), α (yellow-red) and γ (blue) for datasets using test functions with $\lambda_1 = 1.9 \times 10^{-9}\,\mathrm{m}^2\,\mathrm{s}^{-1}$ (left column) $1.5 \times 10^{-9}\,\mathrm{m}^2\,\mathrm{s}^{-1}$ (centre column) and $1.1 \times 10^{-9}\,\mathrm{m}^2\,\mathrm{s}^{-1}$ (right column). The rows of each grid correspond to test functions with $a \in \{0.5, 0.6, 0.7\}$. The crossing angle varies with grid column.

Figure 4.3 plots $\bar{c}$ against the number of basis functions, K, (a), the width of the basis functions, σ,(b) and the width of the basis functions used to approximate the data, σ_{data}, (c) for RBF-QBall. In these plots, all parameters are varied to maximize $\bar{c}$ for the parameter of interest. We find that the $\bar{c}$ is maximised when using 120 basis functions (figure 4.3a). $\bar{c}$ appears to be stable when the width of the basis function is between $7 - 12°$ (figure 4.3b), although the maximum is at $7.5°$. Figure 4.3d shows the effect of varying σ_{data} on $\bar{c}$. The optimal setting of σ_{data} is around $3°$. Increasing the width of the basis functions for the RBF representation of the data yields no improvement in $\bar{c}$. The optimal RBF-QBall settings are: $K = 120$, $\sigma = 7.5°$, $\sigma_{data} = 3°$, $g = 1$ and $h = 0.5$. At these settings $\bar{c} = 0.25$.

Figure 4.4 shows results for each dataset at the optimal reconstruction settings.

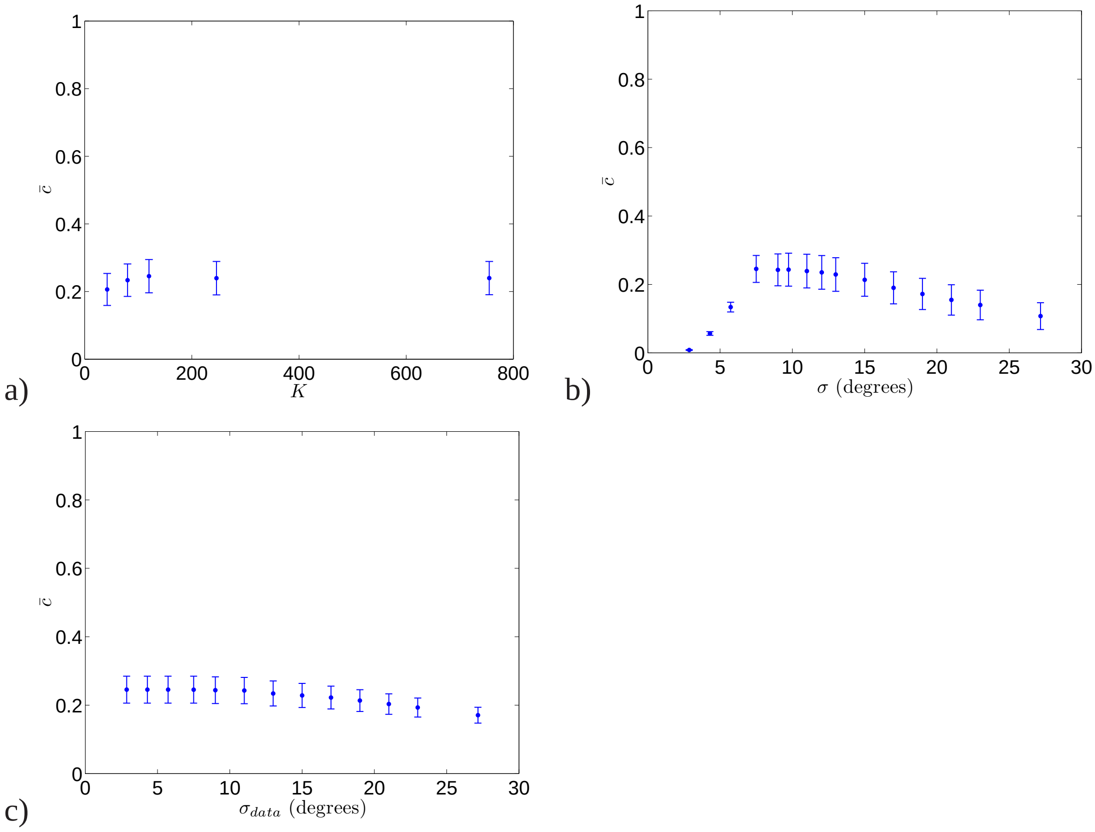

Figure 4.3: Plot of a) K, b) σ and c) σ_{data} against $\bar{c}$ for RBF-QBall to show the effect of varying the algorithm's parameters on its performance.. The error bars show the standard error of the consistency fractions for the 45 datasets.

As with SH-QBall, RBF-QBall is only able to consistently reconstruct a few datasets at $\lambda_1 = 1.9 \times 10^{-9}\,\mathrm{m}^2\,\mathrm{s}^{-1}$ and $\lambda_1 = 1.5 \times 10^{-9}\,\mathrm{m}^2\,\mathrm{s}^{-1}$. However, unlike SH-QBall, the maximum consistency fraction does not reach 1 for any of the datasets. Another difference between RBF-QBall and SH-QBall is that RBF-QBall is able to capture two fibre orientations when the crossing angle is $60°$, $a = 0.5$ and $\lambda_1 = 1.9 \times 10^{-9}\,\mathrm{m}^2\,\mathrm{s}^{-1}$, although the consistency fraction for these datasets is very low (see figure 4.4, top left panel). The full table of results showing the numerical data underlying figure 4.4 is given in appendix F.2.

4.2.3 Conclusions

Peak thresholding offers little improvement on the consistency of the results for QBall regardless of basis used to represent the dODF (see appendix E, figures E.1a and b). The QBall dODFs have very broad peaks and therefore seem less susceptible to spurious peaks caused by noise. However, the dODF peaks are also often very small, so even

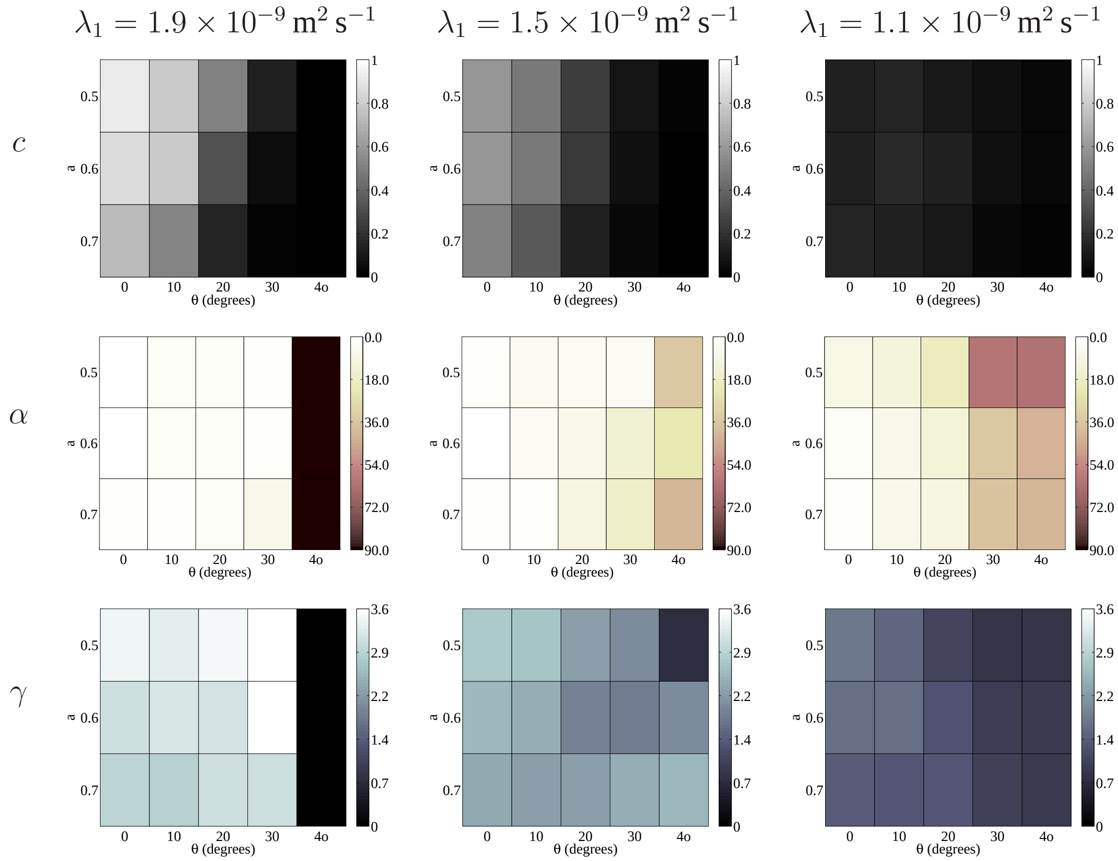

Figure 4.4: Tile plot for RBF-QBall reconstructions showing c (gray), α (yellow-red) and γ (blue) for datasets using test functions with $\lambda_1 = 1.9 \times 10^{-9}\,\mathrm{m^2\,s^{-1}}$ (left column) $1.5 \times 10^{-9}\,\mathrm{m^2\,s^{-1}}$ (centre column) and $1.1 \times 10^{-9}\,\mathrm{m^2\,s^{-1}}$ (right column). The rows of each grid correspond to test functions with $a \in \{0.5, 0.6, 0.7\}$. The crossing angle varies with grid column.

modest threshold settings are likely to remove useful fibre-orientation estimates.

In terms of the quality of reconstruction, figures 4.2 and 4.4 show that both SH-QBall and RBF-QBall resolve crossing fibres consistently when $\theta = 20°$ but not when $\theta = 30°$. The reconstructions also give poor results when one fibre population provides more signal than the other. The dODFs here appear worse than in [67, 68] because they use higher quality data with higher b-values and many more gradient directions. However, the acquisition scheme used in that work is not suitable for routine clinical use.

SH-QBall has two benefits over the original RBF implementation. Firstly, it gives more consistent results (see figures 4.2 and 4.4, top row) than the RBF implementation for most datasets where $\theta \leq 20°$ and $a \in \{0.5, 0.6\}$, which is perhaps due to the analytic approach to calculating the integrals for the Funk-Radon transform. Second, there is only a single parameter that needs to be optimized for the SH implementation. In contrast, RBF-QBall requires the optimization of 3 parameters and it is unclear how the optimal parameter settings will vary between acquisition schemes and how they interact. Therefore, we recommend using SH-QBall.

4.3 Experiment 2 - Comparison of RBF-SD and RBF-PAS

In section 3.4.4 we discuss how PASMRI can be considered to be SD with a specific response function. In this experiment we examine the effect that changing the response function has on the consistency of reconstructions for a radial basis function implementation of SD. Specifically, we compare a 'spike' response, which assumes diffusion only occurs in the fibre direction, to the PAS response. We use the same linear deconvolution approach to reconstruction to ensure that we are only comparing the changes to the response function. The implementation of RBF-PAS was published in [19].

4.3.1 Method

Both RBF-PAS and RBF-SD are implemented using the linear SD algorithm described in appendix C. For both methods, we use the radial basis functions $\theta(\hat{\mathbf{x}}) = \exp(-\sigma^{-2}\cos^{-1}(\hat{\mathbf{x}} \cdot \hat{\mathbf{y}}))$ centred on a set of reconstruction points, $\hat{\mathbf{y}}$, $k = 1, ..., K$, which are evenly distributed over the sphere; σ controls the width of the radial basis function. In addition to the RBF parameters, RBF-PASMRI has a response function parameter r and SD has the response function parameter d.

For both methods, we use $K = \{42, 80, 120, 246\}$ basis functions and a discrete set of $\sigma \in [10, 150]^\circ$. For RBF-PASMRI, we use the response function $R(\mathbf{q}; \hat{\mathbf{x}}) = r^{-2}\cos(r\mathbf{q} \cdot \hat{\mathbf{x}})$ and choose a set of r such that $r \in [0.5, 5]$. For RBF-SD, we use the 'spike' response function $R(\mathbf{q}; \hat{\mathbf{x}}) = \exp(-bd(\mathbf{q} \cdot \hat{\mathbf{x}}))$ and set the parameter d so that we have a discrete range of $bd \in [0.5, 7]$.

As in the previous experiment, we vary the peak threshold parameters, g and h. We select a discrete set of values such that $g \in [0, 10]$ and $h \in [0, 100]$ for RBF-PAS and $g \in [0, 10]$ and $h \in [0, 8]$ for RBF-SD.

4.3.2 Results

Figure 4.5 shows plots of performance metrics against parameter settings for RBF-PASMRI. Changing the number of basis functions (figure 4.5a) does not have a large effect on the quality of reconstruction, although 80 basis functions gives the greatest mean consistency. Figure 4.5b shows how the response function affects the quality of reconstruction. For each setting of r, we fix the number of basis functions to 80 and vary σ to maximize $\bar{c}$. The response yields the largest $\bar{c}$ at $r = 2.6$. Figure 4.5c plots basis function width, σ, against $\bar{c}$. In this plot the number of basis functions is fixed at 80 and the response is fixed at $r = 2.6$. There is a large increase in $\bar{c}$ at around $\sigma = 40°$ and the value remains around the same value to the end of the tested range. The optimal value for the datasets used is $\sigma = 90°$. The threshold settings that maximize the $\bar{c}$ for RBF-PASMRI are $g = 1.5$ and $h = 62$. The complete list of optimal settings for RBF-PASMRI are: $K = 80$, $r = 2.6$, $\sigma = 90$,$g = 1.5$ and $h = 62$. At these settings $\bar{c} = 0.44$.

Figure 4.6 shows similar plots for RBF-SD. As with RBF-PASMRI, 80 basis function centres provides the highest $\bar{c}$ (figure 4.6a). Figure 4.6b shows the effect of varying the response parameter, bd, on $\bar{c}$. Unlike the PAS response, varying the parameter of the ‘spike’ response gives a gradual change in $\bar{c}$. For RBF-SD, $bd = 5$ maximizes $\bar{c}$, although $bd \in [3.5, 5.5]$ yields similar results. Varying the width of the basis functions (Figure 4.6c) shows a similar general trend to the plot in figure 4.5c, although $\bar{c}$ is maximal at $\sigma = 100°)$. The optimal settings for RBF-SD are: $K = 80$, $bd = 5$, $\sigma = 100$,$g = 1.5$ and $h = 8$. At these settings $\bar{c} = 0.51$.

Figure 4.7 shows the complete set of results for RBF-PASMRI. At the parameter settings selected, the RBF-PASMRI algorithm is able to consistently reconstruct test functions with $\lambda_1 = 1.9 \times 10^{-9}\,\mathrm{m}^2\,\mathrm{s}^{-1}$ and $\theta \leq 10°$ (top left panel). The method is also able to reconstruct test functions with $\theta \leq 40°$ and $\lambda_1 \geq 1.5 \times 10^{-9}\,\mathrm{m}^2\,\mathrm{s}^{-1}$ to some extent, although it fails completely outside of this range. In this range of synthetic data settings the angle bias for RBF-PAS is around $3°$ to $10°$. The complete table of results is provided in Appendix F.3.

Figure 4.8 shows the complete set of results for RBF-SD. The method is able to provide near-consistent results when $\lambda_1 = 1.9 \times 10^{-9}$ and $\theta \leq 20°$. The consistency is reduced slightly when $\lambda_1 = 1.5 \times 10^{-9}$, although the angle bias remains low. As with

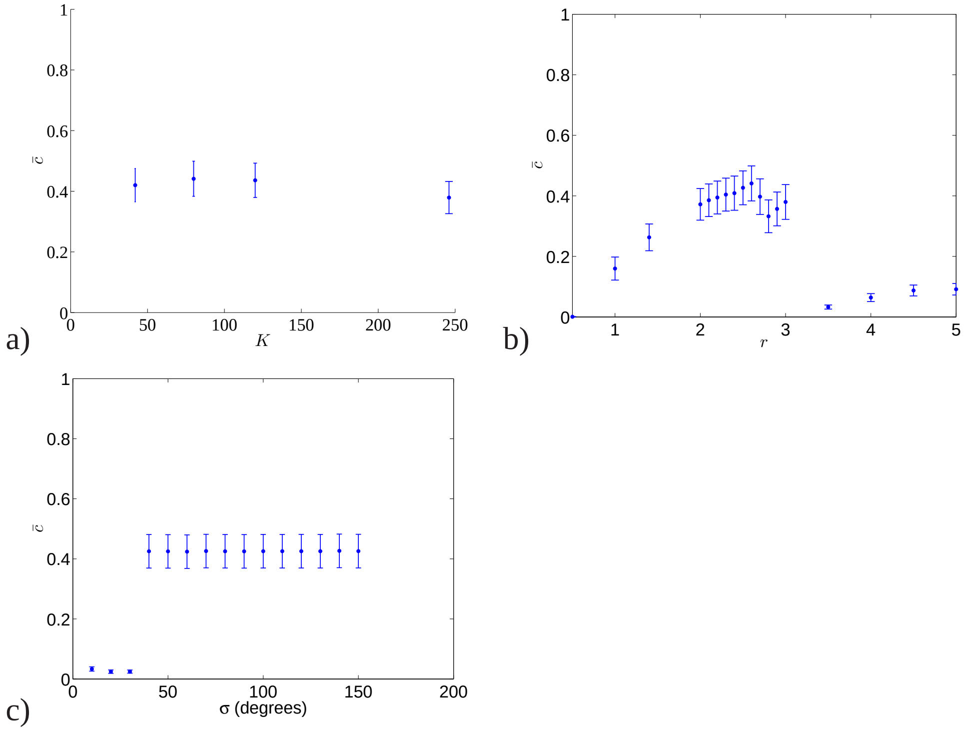

Figure 4.5: Plots the mean consistency fraction, $\bar{c}$, against a) the number of basis functions, K, b) the response parameter, r, and c) the width of the basis functions, σ, for RBF-PAS to show the effect of varying the algorithm's parameters on its performance. The error bars show the standard error of the consistency fraction for the 45 datasets.

RBF-PAS, RBF-SD is unable to recover crossings when $\theta = 40^\circ$ or $\lambda_1 = 1.1 \times 10^{-9}$. However, RBF-SD generally provides more consistent reconstructions (top rows of figures 4.7 and 4.8), has a smaller angle bias (middle rows), and a higher direction concentration (bottom rows). The complete table of numerical results for all datasets is provided in Appendix F.4.

4.3.3 Conclusions

Using a set of $K = 80$ basis functions yields the most consistent results for both RBF-PAS and RBF-SD. Using more basis functions than this does not improve the consistency further and results in longer processing times and greater storage requirements of the reconstructions. In terms of the width of the basis functions, $\bar{c}$ is low for small settings of σ but increases rapidly when $\sigma = 40^\circ$ (RBF-PAS) or $\sigma = 80^\circ$ (RBF-SD). This increase in $\bar{c}$ may be due to a reduction in the number of spurious peaks, since basis functions with broad peaks will be unable to over-fit to the noise in the data. Both RBF-PAS and RBF-SD appear to be stable over large ranges of σ (see figures 4.5c and 4.6c

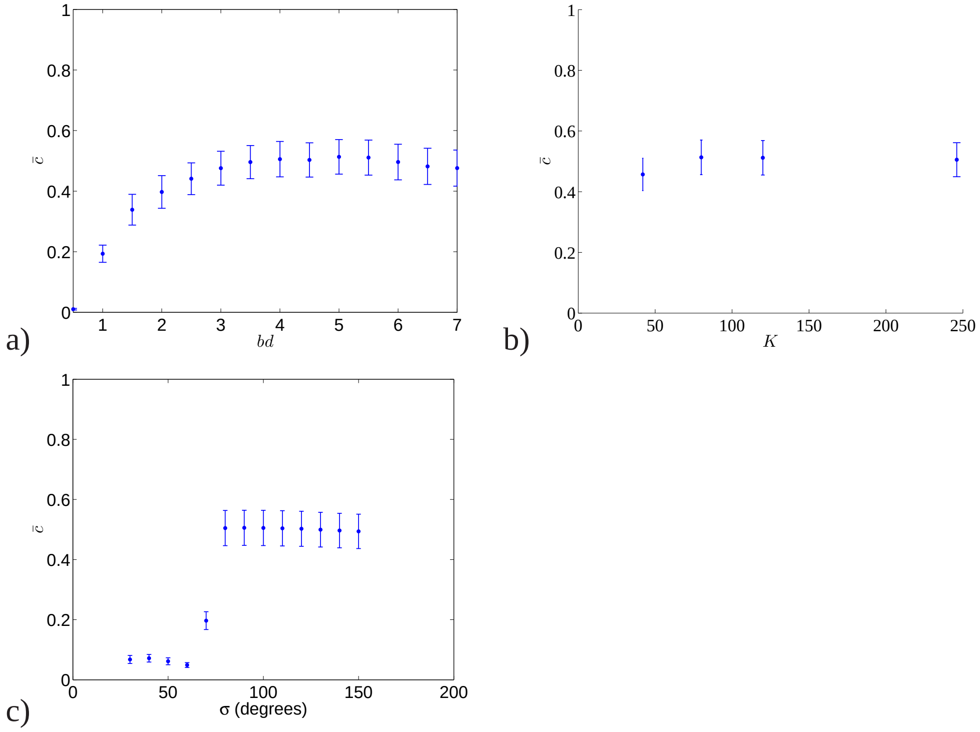

Figure 4.6: Plots $\bar{c}$ against a) the number of basis functions, K, b) the response parameter, bd, and c) the basis function width, σ, for RBF-SD to show the effect of varying the algorithm's parameters on its performance. The error bars show the standard error of the consistency fraction for the 45 datasets.

respectively), although $\bar{c}$ is maximised when setting the width of the basis functions to $\sigma \in \{90°, 100°\}$. In practise voxels may contain three or more fibre populations. Therefore, it may be better to use a smaller value of σ in the stable ranges shown in the figures.

The 'spike' response provides more consistent reconstructions. This is demonstrated in figures 4.7 and 4.8, which show the performance of RBF-PAS and RBF-SD respectively. The optimal setting of the 'spike' response function is $bd = 5$ for the acquisition used here, although the value can be changed in the range $[3.5, 5.5]$ without a large decrease in $\bar{c}$. In contrast, $\bar{c}$ appears to be greatly affected by the precise setting of r for RBF-PAS. This is due to the cosine term used in the response function. As r increases the frequency of the waves on the response increases. Certain frequencies seem to provide good fits to the data. In conclusion, we recommend using the 'spike' response with around $K = 80$ basis functions for an acquisition similar to the one used here.

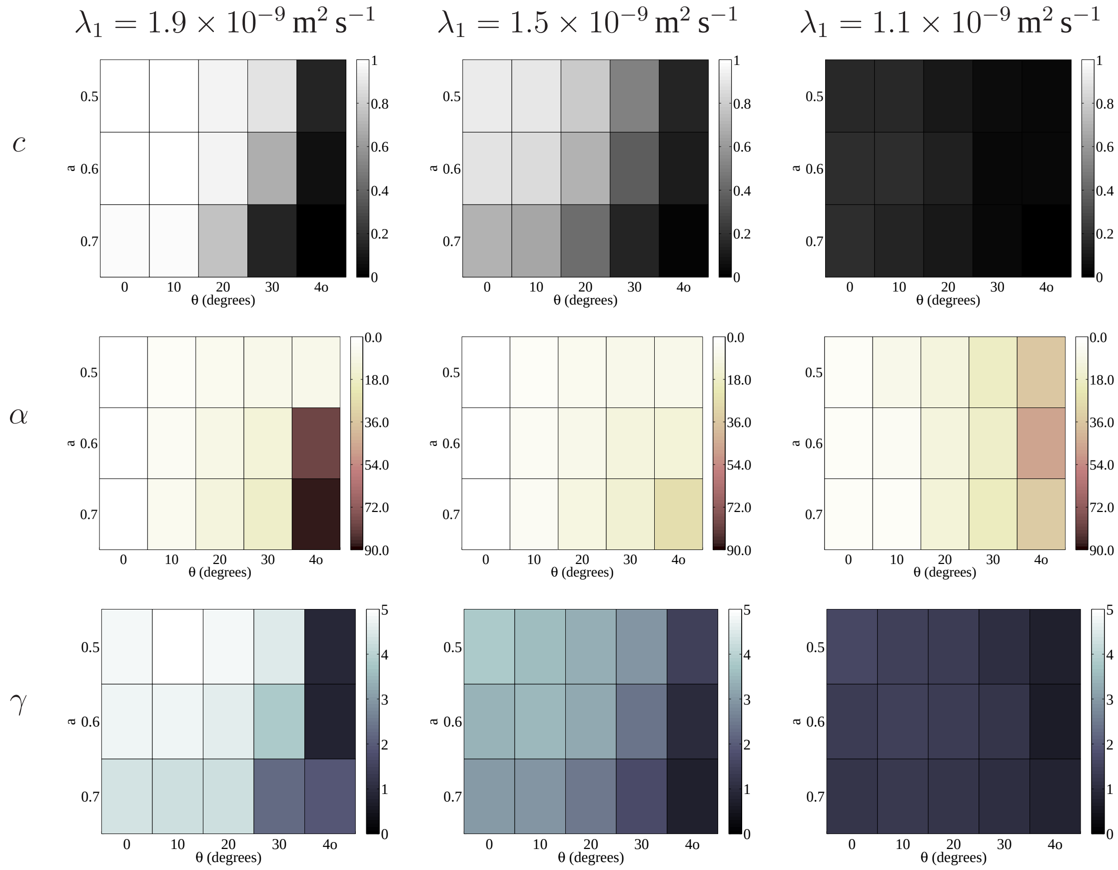

Figure 4.7: Tile plot for RBF-PAS reconstructions showing c (gray), α (yellow-red) and γ (blue) for datasets using test functions with $\lambda_1 = 1.9 \times 10^{-9}\,\mathrm{m}^2\,\mathrm{s}^{-1}$ (left column) $1.5 \times 10^{-9}\,\mathrm{m}^2\,\mathrm{s}^{-1}$ (centre column) and $1.1 \times 10^{-9}\,\mathrm{m}^2\,\mathrm{s}^{-1}$ (right column). The rows of each grid correspond to test functions with $a \in \{0.5, 0.6, 0.7\}$. The crossing angle varies with grid column.

4.4 Experiment 3 - Comparing a SH-SD to RBF-SD

In the previous experiment we investigate the effect of changing the response function of spherical deconvolution on the performance of the algorithm. We show that the choice of response can have a significant effect on the consistency of the reconstructions. In this experiment we investigate the effect of using two different basis function representations, spherical harmonics and spherical radial basis functions, on the quality of reconstruction. We compare the results from RBF-SD given in the previous experiment to those from the original spherical harmonic implementation of the algorithm. In order to make the comparison fair, we change the response function for the spherical harmonic implementation to the ‘spike’ function, although we also show results for the

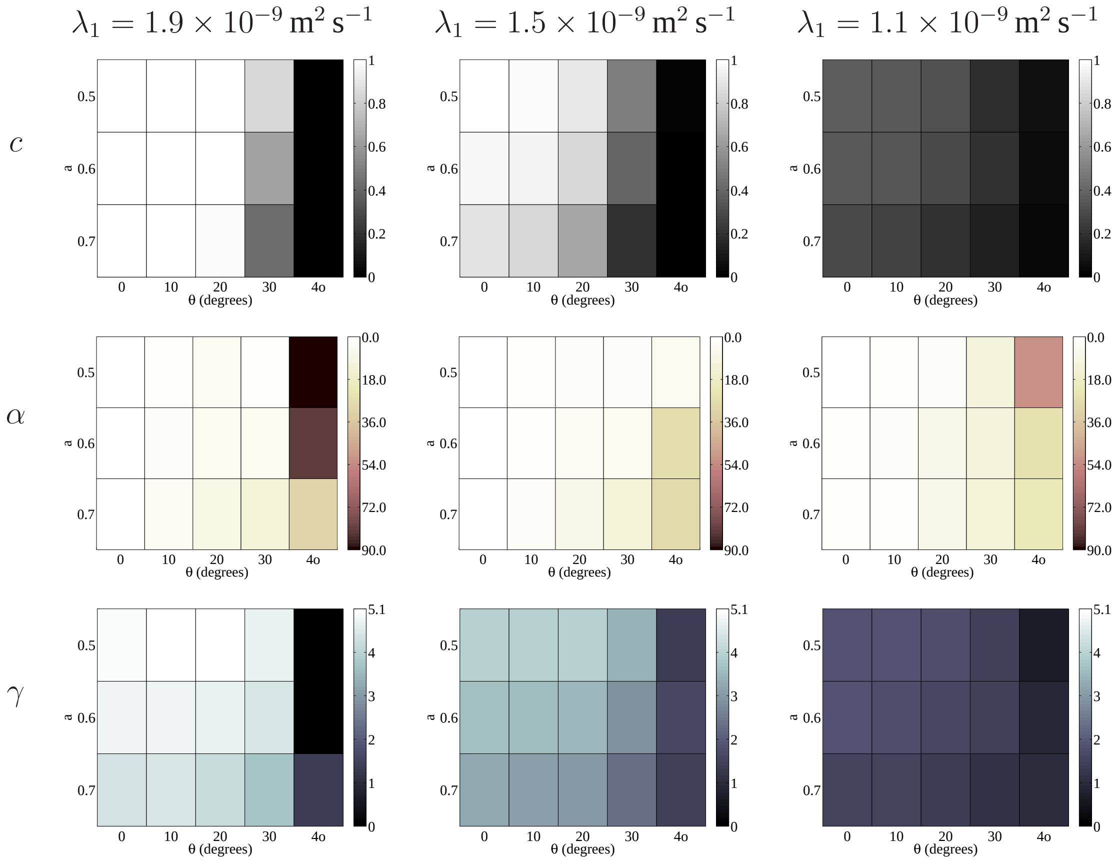

Figure 4.8: Tile plot for RBF-SD reconstructions showing c (gray), α (yellow-red) and γ (blue) for datasets using test functions with $\lambda_1 = 1.9 \times 10^{-9}\,\mathrm{m^2\,s^{-1}}$ (left column) $1.5 \times 10^{-9}\,\mathrm{m^2\,s^{-1}}$ (centre column) and $1.1 \times 10^{-9}\,\mathrm{m^2\,s^{-1}}$ (right column). The rows of each grid correspond to test functions with $a \in \{0.5, 0.6, 0.7\}$. The crossing angle varies with grid column.

DT response used by [77].

4.4.1 Method

The Matlab code for the spherical harmonic implementation of SD [77] was kindly supplied by Donald Tournier. The implementation provided uses the DT response $R(\mathbf{q}; \hat{\mathbf{x}}) = \exp(-t\mathbf{q}\mathbf{D}\mathbf{q})$, where $\mathbf{D} = \upsilon\hat{\mathbf{x}}\hat{\mathbf{x}}^T + \beta\mathbf{I}$. In addition to this, we use the 'spike' response from the previous experiment. The spherical harmonic implementation of Spherical Deconvolution has two parameters: the maximum spherical harmonic order of the fODF and the response parameter (d for the 'spike' response; FA for the DT response). See appendix A for details on the implementation of spherical harmonics.

In this experiment we investigate the quality of SH-SD using maximum spherical harmonic orders of 4 and 6. The settings for the RBF-SD are given in section 4.3.1. We set the FA of the tensor in the range $\{0.4, 0.5, 0.6, 0.7, 0.8, 0.9, 1\}$; the diffusivity is set internally to $Tr(\mathbf{D}) = 0.9 \times 10^{-9}\,\mathrm{m}^2\,\mathrm{s}^{-1}$. We use discrete settings of the parameter d in the 'spike' response so that $bd \in [0.5, 8]$.

For both methods, we vary the threshold parameters, g and h, to maximise $\bar{c}$. We select a discrete set of values for both parameter such that $g \in [0, 10]$ and $h \in [0, 8]$.

4.4.2 Results

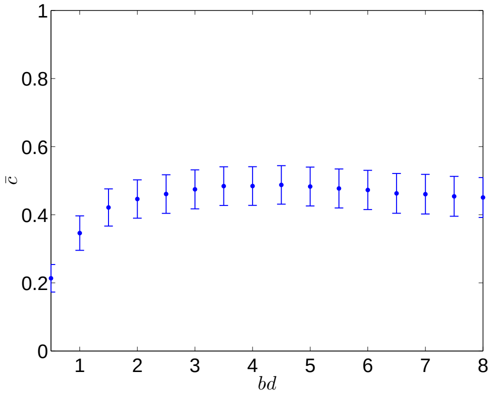

Figure 4.9: Plots of $\bar{c}$ against bd of the 'spike' response for SH-SD to show the effect of varying the parameter on the algorithm's performance. The error bars show the standard error of the consistency fraction for the 45 datasets.

Only Spherical Harmonic with a maximum spherical harmonic order of 4 produced non-zero consistency fractions for SD when using the original spherical harmonic implementation. Figure 4.9 plots the effect of altering the parameter bd of the 'spike' response function. From the settings investigated, $\bar{c}$ is maximised at around $bd = 4.5$, although the value of $\bar{c}$ does not vary much in the range $bd \in [3.5, 5.5]$. The optimal settings for SH-SD ('spike' response) are: maximum spherical harmonic order 4, $bd = 4.5$, $g = 2$ and $h = 1$. At these settings $\bar{c} = 0.49$

SH-SD with the 'spike' response gives $\bar{c} = 0.49$ when optimized. The method therefore has a similar performance to RBF-SD, which gives $\bar{c} = 0.51$ when optimized. Looking at the datasets individually (figures 4.11 and 4.8), both implementations of SD can reconstruct voxels where $\theta = 30°$ but not $\theta = 40°$. However, RBF-SD reconstructs datasets where $m = 0.7$ more consistently (top row of figure 4.8) than SH-SD.

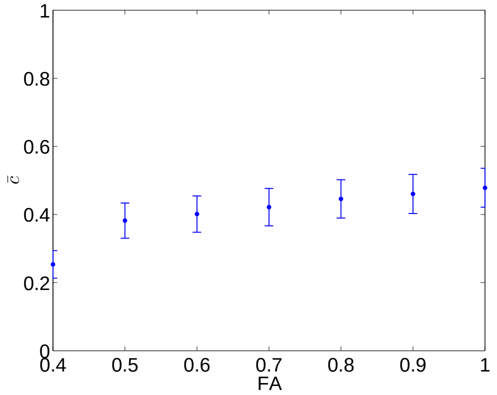

Figure 4.10: Plots of $\bar{c}$ against the FA of the DT response function for SH-SD to show the effect of varying the parameter on the algorithm's performance. The error bars show the standard error of the consistency fraction for the 45 datasets.

Figure 4.10 plots the effect of altering the FA of the DT response for SH-SD. There is an increase in $\bar{c}$ as the FA of the response increases and $\bar{c}$ is maximized when the FA=1. The optimal settings for SH-SD (DT response) are: maximum spherical harmonic order 4, FA=1, $g = 2.5$ and $h = 2$. At these settings $\bar{c} = 0.48$.

Figure 4.12 shows a tile plot for SH-SD with the DT response. When the test functions have $\lambda_1 = 1.9 \times 10^{-9}\,\mathrm{m}^2\,\mathrm{s}^{-1}$, SD can consistently resolve fibres with separation angles of 60° ($\theta = 30^\circ$), but not 50° ($\theta = 40^\circ$). At $\lambda_1 = 1.5 \times 10^{-9}\,\mathrm{m}^2\,\mathrm{s}^{-1}$ the consistency of the reconstructions drops for all test functions. SH-SD (DT reponse) produces very inconsistent reconstructions when $\lambda_1 = 1.1 \times 10^{-9}\,\mathrm{m}^2\,\mathrm{s}^{-1}$ for the parameter settings selected. This method provides slightly biased estimates of fibre-orientation with the angle bias for each dataset typically around 3 to 10°. The consistency of reconstructions from SH-SD using the DT response is similar to that of SH-SD using the 'spike' response, although the consistency fraction is noticeably lower for several datasets where $\theta \in \{0^\circ, 20^\circ\}$ and $\lambda_1 \in \{1.5, 1.9\} \times 10^{-9}\,\mathrm{m}^2\,\mathrm{s}^{-1}$ (see figures 4.11 and 4.12, top rows). The complete table of results is provided in Appendix F.5.

4.4.3 Conclusions

The RBF implementation of spherical deconvolution gives a slightly higher $\bar{c}$ than the SH implementation. When looking at the consistency fractions for each dataset, the RBF implementation provides more consistent results when one fibre population con-

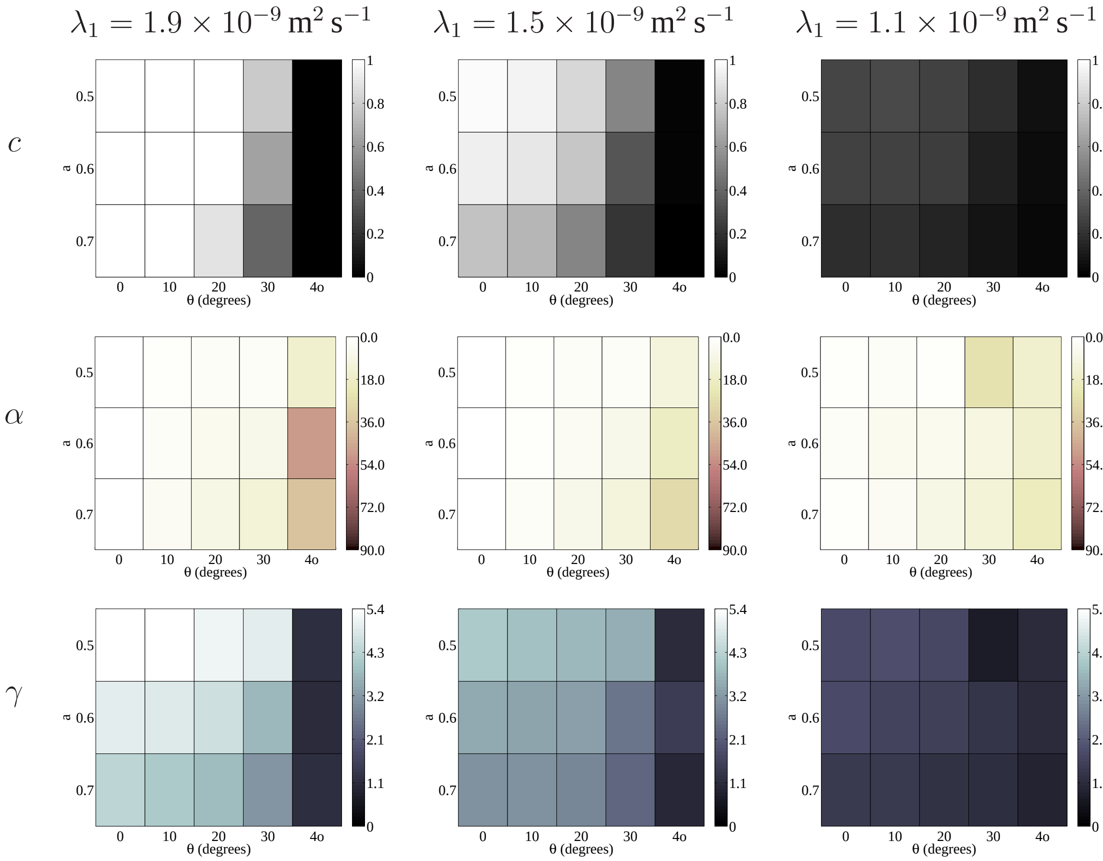

Figure 4.11: Tile plot for SH-SD (‘spike’ response) reconstructions showing c (gray), α (yellow-red) and γ (blue) for datasets using test functions with $\lambda_1 = 1.9 \times 10^{-9}\,\mathrm{m^2\,s^{-1}}$ (left column) $1.5 \times 10^{-9}\,\mathrm{m^2\,s^{-1}}$ (centre column) and $1.1 \times 10^{-9}\,\mathrm{m^2\,s^{-1}}$ (right column). The rows of each grid correspond to test functions with $a \in \{0.5, 0.6, 0.7\}$. The crossing angle varies with grid column.

tributes more to the signal than the other. In addition to this, the direction concentration is slightly larger for the RBF implementations than for the SH implementations, especially when $\lambda_1 = 1.9 \times 10^{-9}\,\mathrm{m^2\,s^{-1}}$. However, the SH implementation has less parameters to optimize than the RBF implementation and, depending upon the response function used, may be more intuitive to set. Optimizing the RBF implementation of SD for each acquisition scheme is computationally heavy task and it is still unclear how the settings will affect the reconstruction performance for voxels containing one or many fibre-populations. Therefore, the spherical harmonic implementation is preferable despite the small sacrifice in reconstruction consistency.

The two response functions used for SH-SD give similar results. However, the ‘spike’ function appears to give slightly more consistent reconstructions than the DT

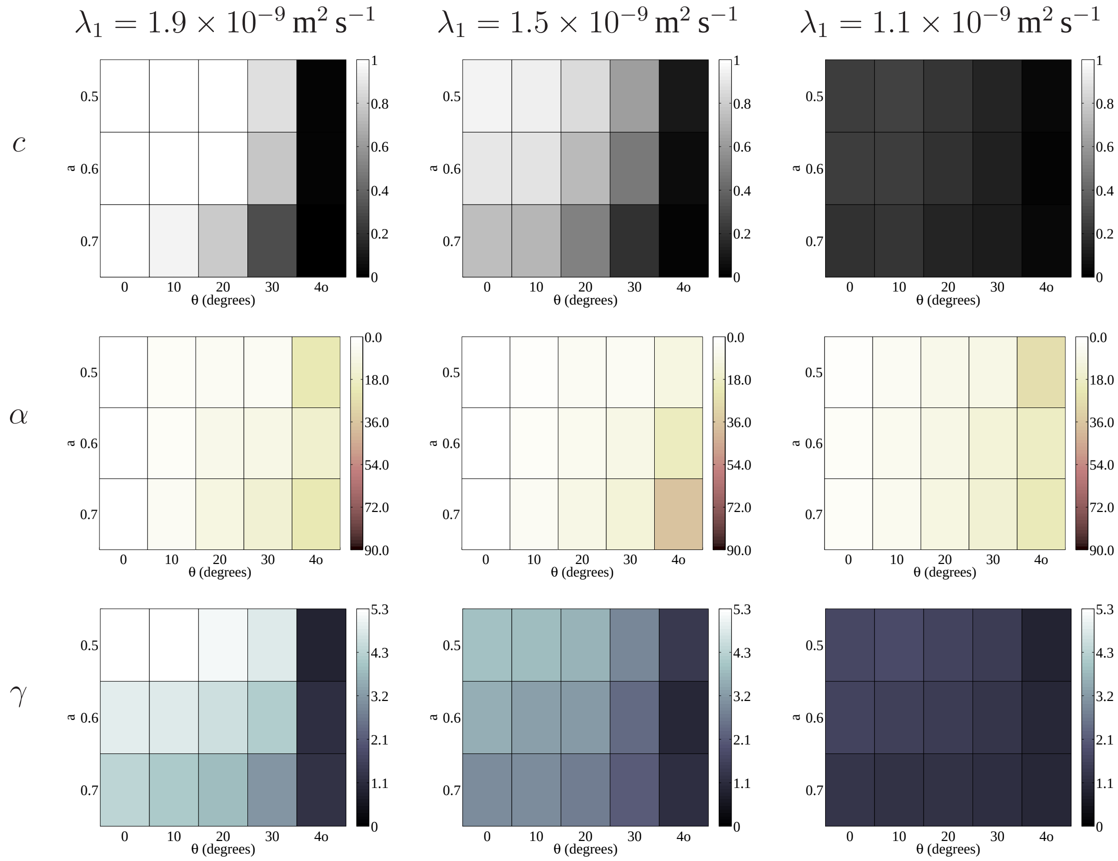

Figure 4.12: Tile plot for SH-SD (DT response) reconstructions showing c (gray), α (yellow-red) and γ (blue) for datasets using test functions with $\lambda_1 = 1.9 \times 10^{-9}\,\mathrm{m^2\,s^{-1}}$ (left column) $1.5 \times 10^{-9}\,\mathrm{m^2\,s^{-1}}$ (centre column) and $1.1 \times 10^{-9}\,\mathrm{m^2\,s^{-1}}$ (right column). The rows of each grid correspond to test functions with $a \in \{0.5, 0.6, 0.7\}$. The crossing angle varies with grid column.

response in datasets where $\lambda_1 \geq 1.5 \times 10^{-9}\,\mathrm{m^2\,s^{-1}}$ and $\theta \leq 20^\circ$ (see figures 4.11 and 4.12, top rows). The 'spike' response also has a higher direction concentration (see figures 4.11 and 4.12, bottom rows), although the angle bias is similar regardless of the response used. It is unclear whether other response functions may yield more consistent results over all datasets.

4.5 Experiment 4 - Comparing CSD to PASMRI and MESD

In this experiment we optimize and compare three of the more established non-linear methods, CSD, PASMRI and MESD.

4.5.1 Method

Constrained spherical deconvolution (CSD) has five parameters that need to be optimized (see appendix D for implementation details). There are two sets of spherical harmonic basis functions, each with a maximum spherical harmonic order. One set represents the data and the other represents the fODF. The third parameter is the FA of the response function. Finally, CSD has two parameters for regularization. The first is the regularization parameter τ and the second controls the a parameter λ that controls the degree of regularization. For the comparisons here we use the following ranges for the parameters: $\lambda \in \{0, 0.25, 0.5, 1, 2, 5, 10\}$ and $\tau \in \{0\%, 10\%, 20\%, 30\%\}$, as well as the maximum order of the spherical harmonic as {6, 8, 10, 12, 14, 16}. In addition to the SH basis for the fODF, we fit a SH basis to the data using maximum spherical harmonic orders of 6 and 8. We limit the maximum order for data interpolation to 8 because an order 10 fit has 66 free parameters. We alter the FA of the DT used to generate the response function in the range {0.4, 0.5, 0.6, 0.7, 0.8, 0.9, 1}. The Matlab code for CSD was kindly supplied by Donald Tournier

Both PASMRI and MESD only have a single parameter to optimize. For PASMRI, we use $r \in \{1.0, 1.1, 1.2, 1.3, 1.4, 1.5, 1.6, 1.7, 1.8, 1.9, 2.0\}$. For MESD, we set d such that we have a set of bd in the range $bd \in [0.8, 3]$.

As in the previous experiment, we vary the peak threshold parameters, g and h. We select a discrete set of values such that $g \in [0, 15]$ and $h \in [0, 15]$ for PASMRI and MESD and $g \in [0, 15]$ and $h \in [0, 8]$ for CSD.

4.5.2 Results

Figure 4.13 shows the effect of varying each parameter of CSD on the mean consistency fraction. When varying each parameter, all of the other parameters are fixed at their optimum values. The setting of τ (figure 4.13a) has little effect on $\bar{c}$. In contrast, varying λ has a much larger effect on $\bar{c}$. Figure 4.13b plots λ against $\bar{c}$. At $\lambda = 0$ the reconstructions are inconsistent, but a small increase in λ results in a large increase in $\bar{c}$. Increasing λ further results in a gradual reduction in $\bar{c}$. The consistency fraction is greatest when modelling the fODF (figure 4.13c) using an order 8 spherical harmonic fit and the data (figure 4.13d) using an order 6 spherical harmonic fit. Unlike SH-SD (DT response), $\bar{c}$ does not increase linearly with FA. Instead, $\bar{c}$ is maximimal when the response function has an FA of 0.6 (figure 4.13e). The optimal settings for CSD are $\lambda = 0.25$, $\tau = 0$, $SH = 8$, $SH_{data} = 6$, FA=0.6, $g = 6$ and $h = 0$. At these settings $\bar{c} = 0.62$.

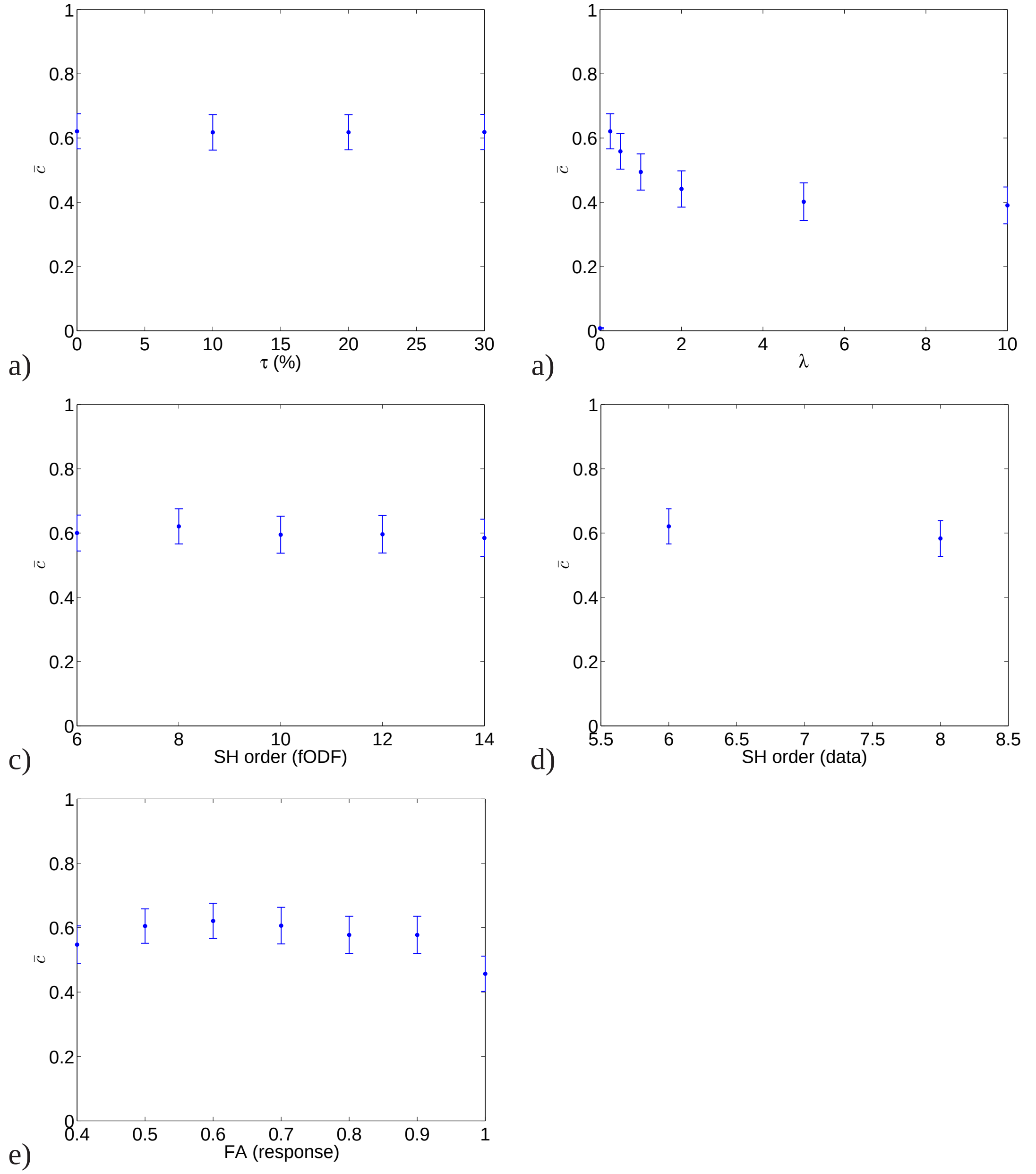

Figure 4.13: Effect of changing parameter settings on mean consistency fraction, $\bar{c}$, for CSD. The parameters are a) τ, b) λ, c) fODF SH order, d) data ODF SH order and e) response FA. The error bars show the standard error of the consistency fraction for the 45 datasets.

Figure 4.14 shows the effect of changing the parameters for MESD (left) and PASMRI (right) on $\bar{c}$. The setting $bd = 1.8$ maximizes $\bar{c}$ for MESD, whereas the value

$r = 1.5$ gives the highest $\bar{c}$ for PASMRI. The effect of changing the PAS parameter r is less eratic than for the linear implementation (RBF-PAS). The threshold settings that maximize $\bar{c}$ for PASMRI and MESD are $g = 8$, $h = 0$ and $g = 7$, $h = 4$ respectively. The optimal settings for PASMRI are: $r = 1.5$, $g = 8$ and $h = 0$. At these settings $\bar{c} = 0.58$. For MESD, the maximum mean consistency fraction ($\bar{c} = 0.54$) is observed at the settings: $bd = 1.8$, $g = 7$ and $h = 4$.

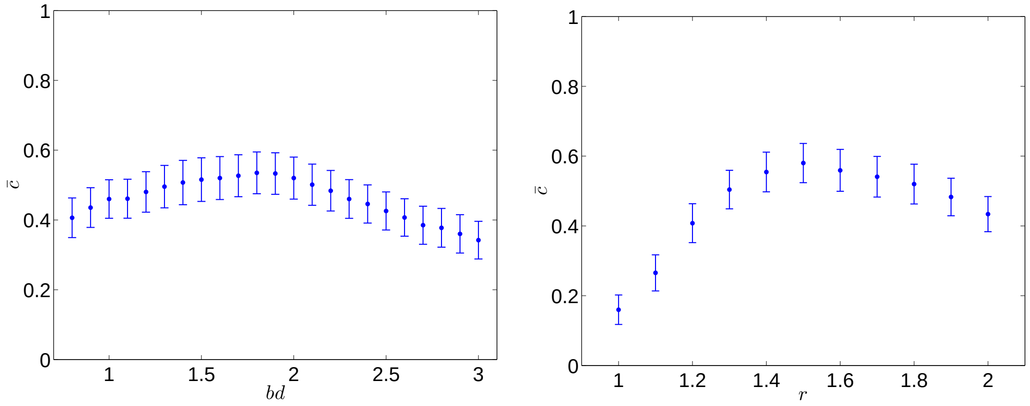

Figure 4.14: Plots of mean consistency fraction, $\bar{c}$, against the parameter for MESD (left) and PASMRI (right). The error bars show the standard error of the consistency fraction for the 45 datasets.

CSD (figure 4.15) and PASMRI (figure 4.16) both provide consistent reconstructions when $\lambda_1 = 1.9 \times 10^{-9}\,\mathrm{m}^2\,\mathrm{s}^{-1}$ and $\theta \leq 20°$. The consistency of reconstructions from both methods are generally high even when $\lambda_1 = 1.5 \times 10^{-9}\,\mathrm{m}^2\,\mathrm{s}^{-1}$ and $\theta = 60°$, although outside of this range the methods fail. In contrast, MESD (figure 4.17) mainly gives less consistent reconstructions than PASMRI or CSD when $\lambda_1 = 1.5 \times 10^{-9}\,\mathrm{m}^2\,\mathrm{s}^{-1}$. However, MESD provides more consistent reconstructions than all of the other two algorithms for datasets where $\lambda_1 = 1.5 \times 10^{-9}\,\mathrm{m}^2\,\mathrm{s}^{-1}$ and $\theta = 40°$. The angle bias for CSD and MESD is less than $4.5°$ for datasets where $\lambda_1 \geq 1.5 \times 10^{-9}\,\mathrm{m}^2\,\mathrm{s}^{-1}$ and $\theta \leq 20°$. PASMRI has a higher angle bias over this range with values lower than $13°$.

4.5.3 Conclusions

We find that the non-linear reconstruction algorithms all give consistent results for most of the datasets. In particular, CSD gives the most consistent results, with PASMRI performing almost as well. The consistency of MESD reconstructions is slightly lower

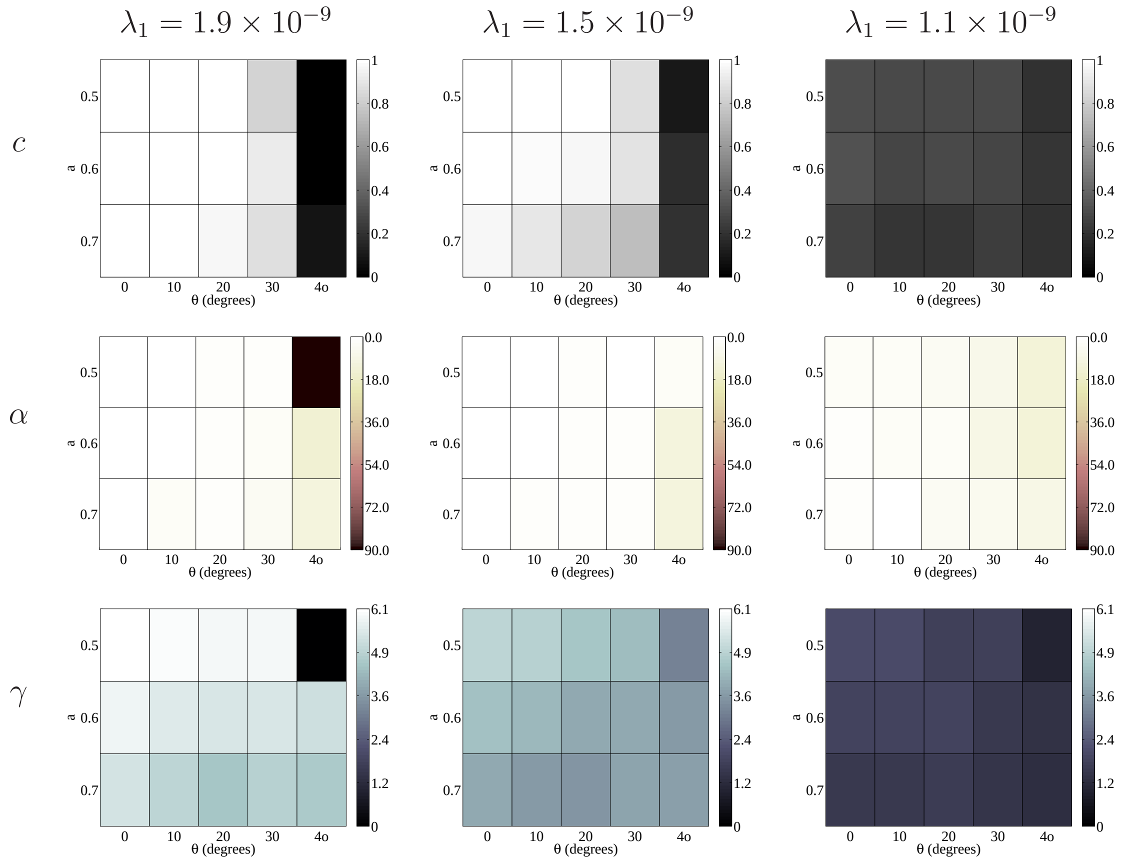

Figure 4.15: Tile plot for CSD reconstructions showing c (gray), α (yellow-red) and γ (blue) for datasets using test functions with $\lambda_1 = 1.9 \times 10^{-9}\,\mathrm{m}^2\,\mathrm{s}^{-1}$ (left column) $1.5 \times 10^{-9}\,\mathrm{m}^2\,\mathrm{s}^{-1}$ (centre column) and $1.1 \times 10^{-9}\,\mathrm{m}^2\,\mathrm{s}^{-1}$ (right column). The rows of each grid correspond to test functions with $a \in \{0.5, 0.6, 0.7\}$. The crossing angle varies with grid column.

than for the other methods, except for datasets where $\lambda_1 = 1.5 \times 10^{-9}$ and the crossing angle is 50°, where the consistency is around 0.5. The reason for this difference may be due to the tuning of the parameter setting; other settings of bd may result in greater consistency in other datasets. This is also true of the other reconstruction algorithms. The angle bias of all of the methods examined in this section is low across the range, particularly for CSD.

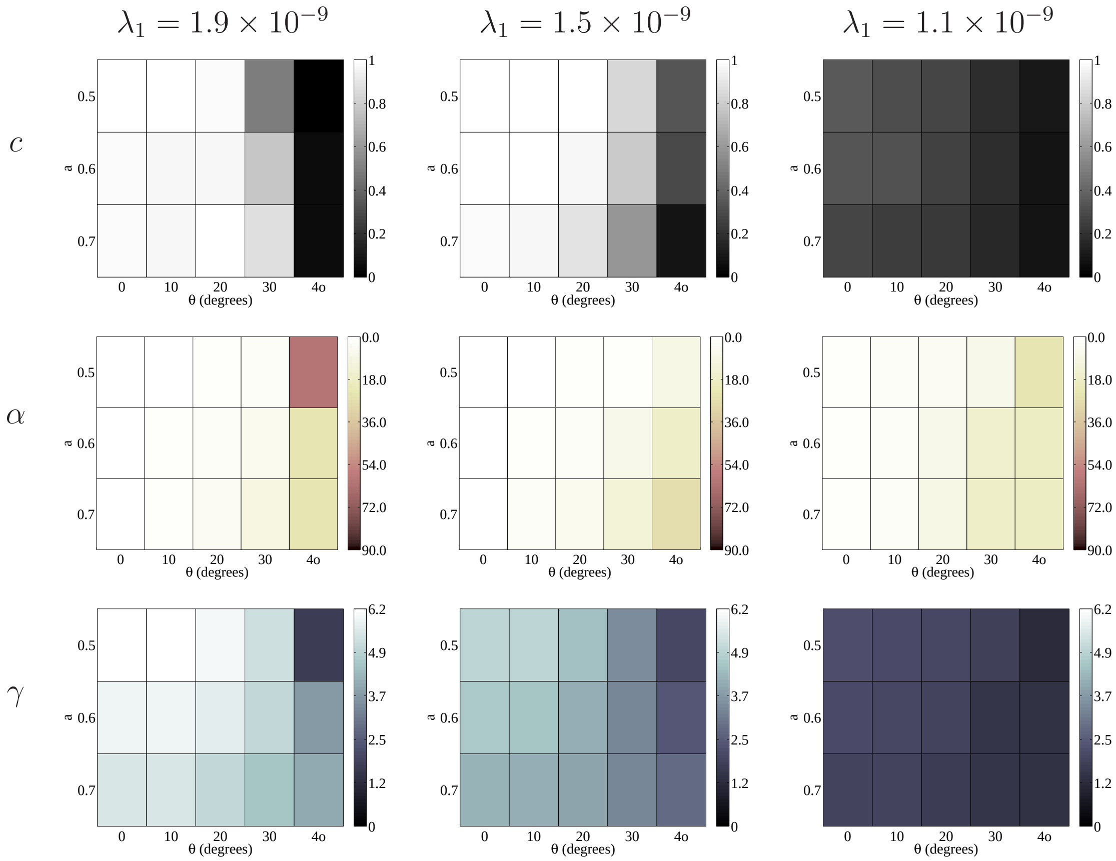

Figure 4.16: Tile plot for PASMRI reconstructions showing c (gray), α (yellow-red) and γ (blue) for datasets using test functions with $\lambda_1 = 1.9 \times 10^{-9}\,\mathrm{m}^2\,\mathrm{s}^{-1}$ (left column) $1.5 \times 10^{-9}\,\mathrm{m}^2\,\mathrm{s}^{-1}$ (centre column) and $1.1 \times 10^{-9}\,\mathrm{m}^2\,\mathrm{s}^{-1}$ (right column). The rows of each grid correspond to test functions with $a \in \{0.5, 0.6, 0.7\}$. The crossing angle varies with grid column.

4.6 Time requirements of the reconstruction algorithms

In this section we look at the time requirements of the algorithms compared above. To test the time requirements of the algorithms, we generate a synthetic dataset consisting of 144 voxels and time how long each algorithm takes to reconstruct the dataset. As a further test, we time how long the subsequent process of finding the peak orientations takes for each algorithm. All processing was performed on a 2.26GHz processor running Windows Vista.

The dataset used in this analysis consists of two-fibre voxels generated using equation 4.1.1, with $a = 0.5$, $\lambda_1 = 1.9 \times 10^{-9}\,\mathrm{m}^2\,\mathrm{s}^{-1}$, $\theta = 0^\circ$ and $S = 20$. The parameters

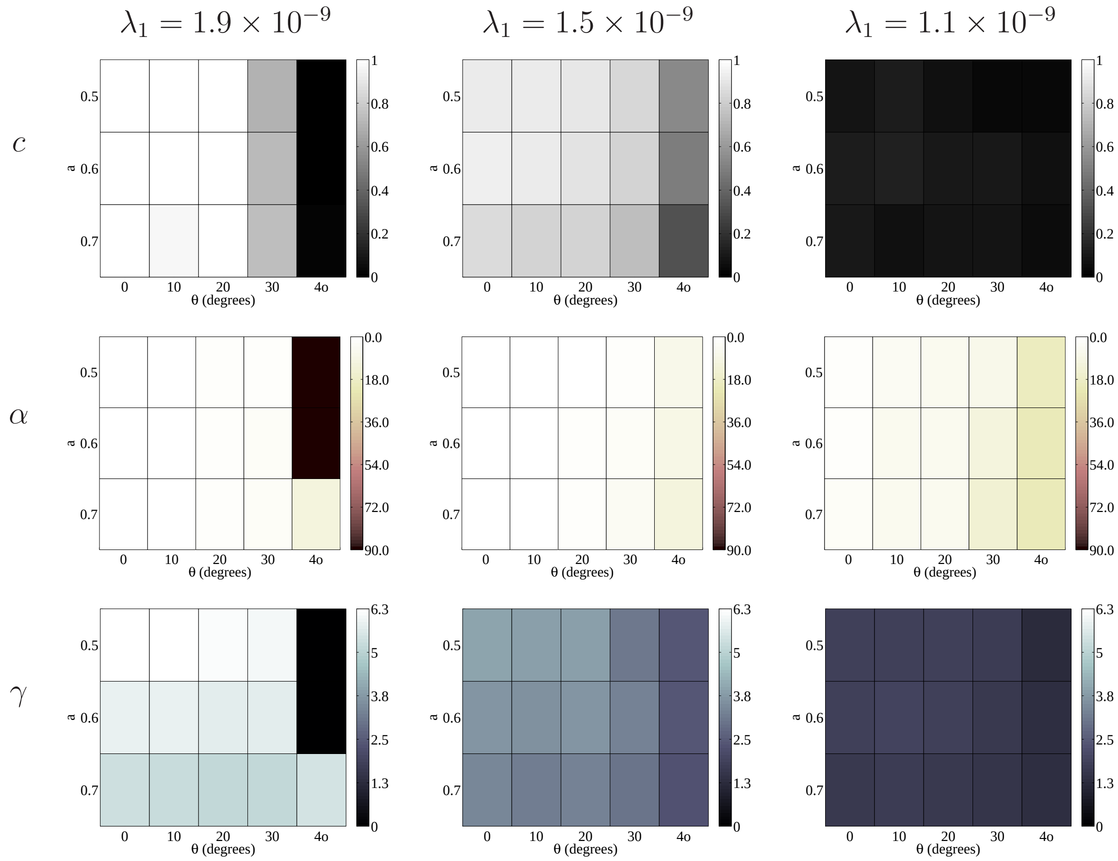

Figure 4.17: Tile plot for MESD reconstructions showing c (gray), α (yellow-red) and γ (blue) for datasets using test functions with $\lambda_1 = 1.9 \times 10^{-9}\,\mathrm{m}^2\,\mathrm{s}^{-1}$ (left column) $1.5 \times 10^{-9}\,\mathrm{m}^2\,\mathrm{s}^{-1}$ (centre column) and $1.1 \times 10^{-9}\,\mathrm{m}^2\,\mathrm{s}^{-1}$ (right column). The rows of each grid correspond to test functions with $a \in \{0.5, 0.6, 0.7\}$. The crossing angle varies with grid column.

of each algorithm were set to the values that maximised $\bar{c}$ in the comparisons performed earlier on in the chapter.

Table 4.1 shows the reconstruction and peak-extraction times for each algorithm. The linear algorithms (RBF-SD, SH-SD, RBF-QBall and SH-QBall) all have a fast reconstruction time. However, the calculation of the fibre-orientation estimates is faster for the linear algorithms that use spherical harmonics to represent the ODF (SH-SD and SH-QBall) than those that use radial basis functions (RBF-SD and RBF-QBall). CSD has a short reconstruction time, and the calculation of the fibre-orientation estimates also has a low time requirement. PASMRI and MESD take several orders of magnitude

algorithm	computational complexity	time (s)		
		reconstruction	peak extraction	total
CSD	medium	4	38	42
PASMRI	high	4466	21	4487
MESD	high	5752	27	5579
SH-SD	low	5	17	22
RBF-SD	low	1	153	154
RBF-QBall	low	1	237	238
SH-QBall	low	2	26	28

Table 4.1: Summary of the computational complexity and time requirements for all optimized algorithms. RBF-PAS has been omitted since it is a variation of RBF-SD and therefore has the same complexity and time requirements.

longer to run than the algorithms described above, although the time required for peak-orientation extraction is comparable to that of SH-SD and SH-QBall.

The results suggest that using spherical harmonics to represent the ODF helps speed up post-processing of the reconstructions to find the peak orientations. In terms of the non-linear algorithms, the overall computation time for CSD is similar to that of the linear algorithms, although the algorithm complexity is slightly higher. PASMRI and MESD both take far longer to reconstruct the data than the other methods tested. This is in part due to the comprehensive checks that the original algorithm uses. Removing these checks results in a significant reduction of computation times.

4.7 Conclusions and Future Work

In this chapter we have presented a standardised framework for optimizing and comparing multiple-fibre reconstruction algorithms. As far as we know, this is the first head-to-head analysis of multiple-fibre algorithms using a standardized framework that optimizes the parameters of each reconstruction algorithm. We provide a table of the mean consistency fraction, $\bar{c}$, and parameter settings for each reconstruction algorithm in table 4.2. As expected, non-linear algorithms, such as CSD and PASMRI, give more consistent results than the linear methods. This is particularly noticeable when the crossing angle between fibre populations is 60° (i.e. $\theta = 30^\circ$) or the mixing parameter

$a = 0.7$. In both of these cases, CSD, PASMRI and MESD all give more consistent results than the other methods. In this work we calibrate the non-linear implementation of PASMRI for our datasets. Although we present an optimal setting of $r = 1.5$, this value only holds for two-fibre configurations. We recommend using $r = 1.4$, as used by Jansons and Alexander [15], which is optimized using one, two and three fibre datasets. Although PASMRI, MESD and CSD all give consistent results, the computation time of CSD is several orders of magnitude smaller than that of PASMRI and MESD. However, the implementation of PASMRI and MESD used for this analysis includes a large number of internal checks to test convergence of the algorithm. If these are removed there is a significant increase in the speed of the algorithm.

Of the linear algorithms, RBF-SD gives the most consistent results. RBFs allow a greater degree of flexibility when approximating the reconstructed fODF/dODF unless there is a mathematical advantage to using the spherical harmonic representation, as in [70]. However, there are two limitations of the RBF implementation. The first limitation is that it has more tuneable parameters than the spherical harmonic implementation and it is unclear how the optimal settings of these parameters vary with changes to the acquisition scheme. The second limitation is that peak extraction is far slower for the RBF implementation than for the spherical harmonic implementation. Therefore, we recommend using spherical harmonic basis functions.

QBall gives the least consistent results of all the reconstruction algorithms. The QBall results appear worse than those in other studies (e.g. [67, 70]), since the quality of data used here has been limited to a level that can be acquired in a time-frame that is tolerable to patients.

There are, however, several refinements can be made to the design of the framework. Firstly, our work uses datasets with two fibre orientations. Adding voxels containing 1 and even 3 fibre orientations will provide further insight into the capabilities of the reconstruction algorithms.

In this work we use acquisition settings that are typical for a clinical dataset. Further experiments are required to optimise the acquisition for multiple-fibre reconstruction algorithms.

We use the mean consistency fraction, $\bar{c}$ to optimize the parameters of the reconstruction algorithms. This is just one measure that we can use. In future work we will investigate other metrics that may improve the optimization procedure.

algorithm	$\bar{c}$	parameters
CSD	0.62	$\lambda = 0.25$, $\tau = 0$, $SH = 8$, $SH_{data} = 6$, FA=0.6, $g = 6$, $h = 0$
PASMRI	0.58	$r = 1.5$, $g = 8$, $h = 0$
MESD	0.54	$bd = 1.8$, $g = 7$, $h = 4$
RBF-SD	0.51	$K = 80$, $bd = 5$, $\sigma = 100$,$g = 1.5$, $h = 8$
SH-SD (‘spike’ response)	0.49	$SH = 4$, $bd = 4.5$, $g = 2$, $h = 1$
SH-SD (DT response)	0.48	$SH = 4$, FA=1, $g = 2.5$, $h = 2$
RBF-PAS	0.44	$K = 80$, $bd = 5$, $\sigma = 100$,$g = 1.5$, $h = 8$
SH-QBall	0.27	$SH = 6$, $g = 1$, $h = 0$
RBF-QBall	0.25	$K = 120$, $\sigma = 7.5°$, $\sigma_{data} = 3°$, $g = 1$, $h = 0.5$

Table 4.2: Summary of $\bar{c}$ and parameter settings for all optimized algorithms

In addition to this, although the tensor model used to generate data has the benefit of providing the exact orientations of all the fibre orientations present, the model is an over-simplification of the diffusion processes occurring in the brain. Use of simulations or physical phantoms may provide a more realistic dataset with which to test the datasets. Depending on the method used to simulate data, this may in turn allow us to look at other features of the ODF that encode useful information, such as peak shape or sharpness.

Alternatively, we could use brain data to compare the algorithms. However, the lack of a ground truth presents a significant challenge when using brain data to compare reconstruction algorithms. There are several ways to create a ground truth. For example, acquiring high-quality data from an ex-vivo brain can give reliable fibre-orientation estimates. Other techniques, such as tracers and histology, can also provide insight into the microstructure, although combining them with diffusion MRI reconstructions present their own challenges.

Chapter 5

Exploiting Peak Anisotropy for Tracking Through Complex Structures

In this chapter we show that multi-fibre reconstruction techniques, such as Persistent Angular Structure (PAS) MRI or QBall Imaging, provide much more information than just discrete fibre orientations, which is all that previous tractography algorithms exploit from them. We show that the shapes of the peaks of the functions output by multiple-fibre reconstruction algorithms reflect the underlying distribution of fibres. Furthermore, we show how to exploit this extra information to improve probabilistic index of connectivity (PICo) tractography. The method uses the Bingham distribution to model the uncertainty in fibre-orientation estimates obtained from peaks in the PAS or QBall dODF. The Bingham model captures anisotropy in the uncertainty, allowing the method to track through fanning and bending structures, which previous methods do not recover reliably. We devise a new calibration procedure to construct a mapping from peak shape to Bingham parameters. We test the accuracy of the calibration using a bootstrap experiment. Finally, we show that exploiting the peak shape in this way can provide improved PICo tractography results.

5.1 Methods

This section describes how to calculate the shape of the cross-section of peaks from multiple fibre reconstructions and introduces the peak anisotropy, which is a measure of how elliptical the cross-section of a peak is. We then give details of the bi-polar Bingham distribution, which can model anisotropy in a spherical distribution. Finally, we describe a calibration procedure that exploits peak shape to improve estimates of

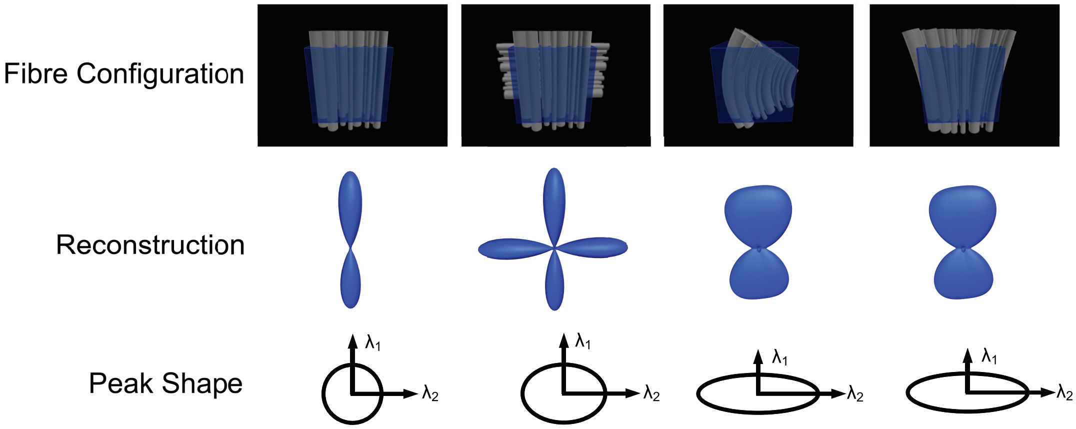

Figure 5.1: Example peak shapes for a variety of plausible white-matter configurations in each voxel. In the crossing-fibre case, there are two peak anisotropies, one for each peak.

uncertainty required for PICo tractography.

5.1.1 Peak Anisotropy

Peak anisotropy describes how elliptical the cross-sections of the peaks of multiple-fibre reconstructions are. We hypothesize here that the peak anisotropy reflects the underlying distribution of fibre-orientations. Figure 5.1 shows examples of peak shapes we expect for different fibre configurations. When the white-matter tract consists of axons oriented parallel with each other (left) we expect the dODF to have a single peak with a circular cross-section; the peak anisotropy is low. In contrast, in voxels containing two fibre populations (centre-left), the peaks of the function will have a slightly elliptical cross-section with the broader part of the ellipse oriented in the plane of the crossing. Finally, where there is a bending or fanning structure present in the voxel (centre-right and right respectively), the peaks of the function will have a highly elliptical cross-section that corresponds to the distribution of fibre-orientations present. Note that the peak shape is the same for the bending and fanning configurations. This is because the distribution of fibre orientations is approximately the same for each configurations, even though the spatial localization of each fibre orientation is different. We use the Hessian to describe each peak. We compute a separate peak Hessian for each peak in the dODF.

To calculate the peak anisotropy, we generalize the standard definition of the frac-

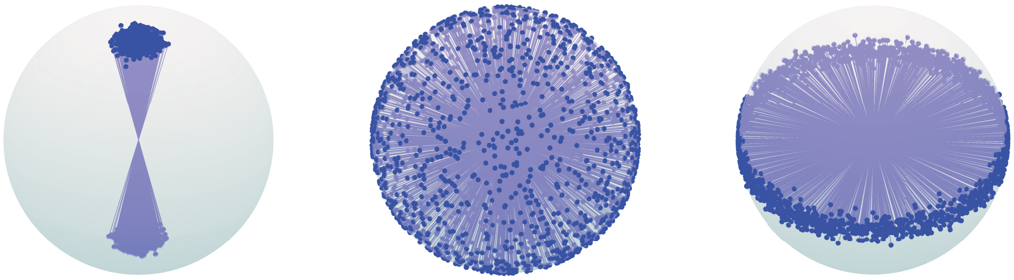

Figure 5.2: The Watson distribution when $\kappa > 0$ (left), $\kappa = 0$ (centre) and $\kappa < 0$ (right). The mean orientation of the distribution, $\mathbf{z}$, is the same for all three images.

tional anisotropy [112] to

$$FA = \sqrt{\frac{N \sum (\lambda_i - \bar{\lambda})^2}{(N-1) \sum \lambda_i^2}}, \tag{5.1}$$

where λ_i, $i = 1, ..., N$ are eigenvalues of some N-dimensional quadratic form and $\bar{\lambda}$ is their mean. For $N = 3$, we get the familiar FA for three-dimensional DTs proposed in [112]. Here we use $N = 2$ to compute the anisotropy of the Hessian at PAS or dODF peaks. We refer to this quantity as the *peak anisotropy*.

We also use the FA of the two minor eigenvalues of the diffusion tensor, which provides an analogue to peak anisotropy for DT-MRI. The FA of the minor eigenvalues quantifies diffusion anisotropy orthogonal to the principal direction of the diffusion tensor.

5.1.2 Spherical Distributions

The Watson distribution [44] is

$$p(\mathbf{x}) = W(\mathbf{x}; \mathbf{z}, \kappa) = M\left(\frac{1}{2}, \frac{3}{2}, \kappa\right)^{-1} \exp[\kappa(\mathbf{z} \cdot \mathbf{x})^2], \tag{5.2}$$

where M denotes the confluent hypergeometric function of the first kind [44], the vector $\mathbf{z}$ is the mean orientation and κ controls the concentration of the distribution. The distribution is isotropic about $\mathbf{z}$. Figure 5.2 shows how various settings of κ affect the shape of the distribution. When $\kappa > 0$ (figure 5.2, left), the distribution is “bipolar” and is most concentrated at $\pm\mathbf{z}$. At $\kappa = 0$ (figure 5.2, centre) the estimates are uniformly distributed over the sphere and when $\kappa < 0$ (figure 5.2, right) the distribution forms

Figure 5.3: The Bingham distribution for $\kappa_1 = \kappa_2 < 0$ (left), $\kappa_1 < \kappa_2 < 0$ (centre) and $\kappa_1 = \kappa_2 = 0$ (right)

a girdle. The Bingham distribution is a generalisation of the Watson distribution with elliptical contours,

$$p(\mathbf{x}) = \frac{1}{M_2(\frac{1}{2}, \frac{3}{2}, \mathbf{A})} \exp[\kappa_1(\mathbf{z_1} \cdot \mathbf{x})^2 + \kappa_2(\mathbf{z_2} \cdot \mathbf{x})^2], \tag{5.3}$$

where

$$\mathbf{A} = (\mathbf{z_3}, \mathbf{z_2}, \mathbf{z_1}) \begin{bmatrix} \kappa_3 & 0 & 0 \\ 0 & \kappa_2 & 0 \\ 0 & 0 & \kappa_1 \end{bmatrix} (\mathbf{z_3}, \mathbf{z_2}, \mathbf{z_1})^T \tag{5.4}$$

and M_2 is the confluent hypergeometric function of the first kind for matrix argument [44]. There are two parameters, $\kappa_1 \leq \kappa_2 \leq 0$, that define the concentration of the distribution, since $\mathbf{A}$ and $\mathbf{A} + d\mathbf{I}$ give equivalent distributions for any real d, where $\mathbf{I}$ is the identity. Therefore it is customary to set $\kappa_3 = 0$. Figure 5.3 shows how setting κ_1 and κ_2 affects the shape of the distribution. When $\frac{\kappa_2}{\kappa_1} \approx 1$ the distribution is circular(figure 5.3, left) . As $\frac{\kappa_2}{\kappa_1} \rightarrow 0$ the distribution becomes increasingly elliptical (figure 5.3, centre). The distribution is a girdle when $\kappa_2 = 0$, and when $\kappa_1 = \kappa_2 = 0$ the distribution is uniform (figure 5.3, right). The mean of the distribution is $\mathbf{z}_1 \times \mathbf{z}_2$ and $\mathbf{z}_1$ and $\mathbf{z}_2$ are the principal axes of the elliptical contours of the PDF.

5.1.3 Calibration

For calibration, we construct a mapping from the two Hessian eigenvalues λ_1 and λ_2 to the Bingham parameters κ_1 and κ_2 using simulations on two-tensor mixture models with known peak directions. Specifically, for a large number of noisy trials we synthesize data from test functions and reconstruct fibre-orientation estimates and associated Hessian matrices using the multiple-fibre reconstruction of choice. In each trial, we rotate the true direction to a common reference frame and apply the same rotation to the reconstructed direction. We collect the rotated reconstruction directions into bins with similar Hessian eigenvalues. We choose the bin sizes empirically such that the bins contain enough samples to provide a robust estimate of the distribution parameters while being small enough to limit the mixing of peak shapes. The bin size is set to 0.45 for the PASMRI calibration, 0.2 for the QBall (spherical harmonic order 4) and 0.3 for the QBall (spherical harmonic order 6) calibrations, and the bins are indexed using the log of the Hessian eigenvalues. We fit the parameters of the Bingham distribution in each bin containing 50 or more samples. Finally, we fit linear surfaces to the log of each Bingham parameter as a function of the log of the Hessian eigenvalues. We create two calibration mappings; one for the voxels containing a single fibre population and one for voxels containing two fibre populations. In voxels where more than two fibre populations are reconstructed we use the two-fibre calibration mapping to estimate uncertainty. The Hessian of the peaks of the dODFs are calculated using the method of Parker and Alexander [10] (see section 3.5.3).

The synthetic data come from test functions described in section 4.1.1. We use combinations of $\lambda_2 \in [1, 5] \times 10^{-10}\,\mathrm{m}^2\,\mathrm{s}^{-1}$, $a \in [0.1, 0.5]$ and $\theta \in [0, 45^o]$. We set $Tr(\mathbf{D}) = \lambda_1 + 2\lambda_2 = 2.1 \times 10^{-9}\,\mathrm{m}^2\,\mathrm{s}^{-1}$, which is approximately the value expected in brain data. For datasets containing a single fibre orientation per voxel, the test function is $p(\mathbf{x}) = G(\mathbf{x}; \mathbf{D}_1, t)$, where $\lambda_2 \in [1, 5] \times 10^{-10}\,\mathrm{m}^2\,\mathrm{s}^{-1}$. The parameters are varied between their minimum and maximum values to create all possible variations of the test function. A random rotation is then applied to the test function to remove any directional bias due to the chosen acquisition scheme. We add Rician noise to make S, the SNR at $b = 0$ equal to 20, which is approximately the same value as the average SNR of the white matter in the $b = 0$ image of each brain volume.

The synthetic data used for calibrating the original diffusion tensor implementation of PICo is constructed using the method described above to generate data from a single Gaussian model; see Cook et al [36] for details.

Figure 5.4 shows an example calibration mapping. Firstly, samples from peaks with similar shapes are collected into bins (figure 5.4a). The figure shows the distribu-

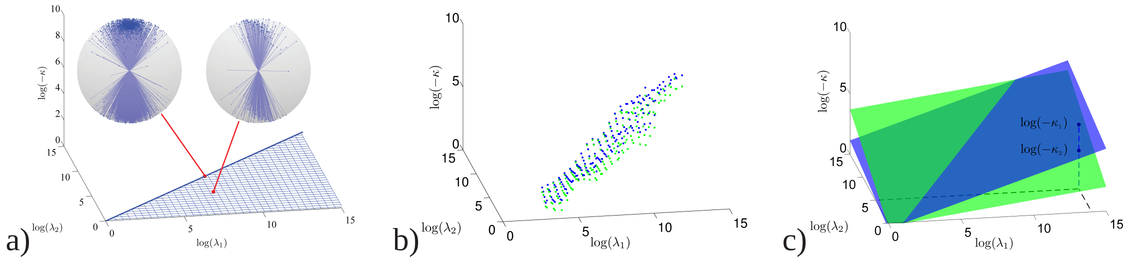

Figure 5.4: Illustration of the calibration procedure. a) Shows the samples after the binning step (bins are demarked by blue lines; the bin size has been doubled for clarity). b) Plots the Bingham distribution parameters, κ_1 (blue dots) and κ_2 (green dots), in each bin prior to fitting calibration mappings. c) The calibration outputs two linear mappings from the Hessian eigenvalues, $\log(\lambda_1)$ and $\log(\lambda_2)$, and the Bingham parameters $\log(-\kappa_1)$ (blue surface) and $\log(-\kappa_2)$ (green surface).

tion of samples for two bins. The distribution of samples on the left comes from a bin where $\log(\lambda_1) = \log(\lambda_2)$. These samples form an isotropic distribution. The distribution on the right comes from a bin where $\log(\lambda_1) > \log(\lambda_2)$. The samples in this bin form an anisotropic distribution. Next, the Bingham distribution is fitted to the samples in each bin (figure 5.4b). The figure shows two markers for each bin, one for $\log(-\kappa_1)$ (blue) and one for $\log(-\kappa_2)$ (green). Finally, a linear surface is fitted to the Bingham parameters (figure 5.4c). Each of the surfaces maps the Hessian eigenvalues of a peak to one of the Bingham parameters. In this example, the blue surface maps λ_1 and λ_2 to κ_1 and the green surface maps λ_1 and λ_2 to κ_2. Only half of the surfaces is ever used, since $\lambda_1 \geq \lambda_2$. Thus, to estimate the Bingham parameters of the uncertainty model for a peak with Hessian eigenvalues λ_1 and λ_2 from the calibration mapping, we set

$$\kappa_1 = -\exp(c_1^{(1)} + c_2^{(1)} \log(\lambda_1) + c_3^{(1)} \log(\lambda_2)) \tag{5.5}$$

$$\kappa_2 = -\exp(c_1^{(2)} + c_2^{(2)} \log(\lambda_1) + c_3^{(2)} \log(\lambda_2)), \tag{5.6}$$

where $c_i^{(1)}$ and $c_i^{(2)}$, $i = 1, 2, 3$, are the coefficients for the two linear surfaces. During tractography we draw vectors from the Bingham distribution with shape parameters κ_1 and κ_2, using the fibre-orientation estimate as the mean of the distribution.

5.1.4 Human Brain Data

High angular resolution diffusion-weighted imaging (HARDI) data were acquired on a 3 T Philips Achieva scanner using an 8-element SENSE head coil. A pulsed gradient spin echo (PGSE) echo planar imaging (EPI) sequence was implemented with TE=54ms, TR=6000ms, Gmax=62mT/m, partial Fourier factor 0.679, 112×112 matrix reconstructed to 128×128 using zero filling, reconstructed resolution $1.836,$ mm $\times$ $1.836,$ mm, slice thickness $2.1,$ mm, 34 contiguous slices, 61 diffusion sensitisation directions at $b = 1200\,\mathrm{s\,mm}^{-2}$, 1 at $b = 0$, SENSE acceleration factor = 2.5. The total imaging time for each HARDI acquisition was approximately 7 minutes. This acquisition was repeated 8 times during a single scanning session in the same volunteer to provide a conventional bootstrapping dataset. All diffusion-sensitised images were registered to the corresponding $b = 0$ image within each slice location to remove eddy current-induced distortions and for all scanning repetitions to the first scan, using the 6-degrees-of-freedom 2D registration schedule file available in FSL's FLIRT. The average SNR in the white-matter regions of the $b = 0$ image is 20.

5.2 Experiments and Results

In this section, we show that the peaks of multiple-fibre reconstructions do provide useful information that can be used to improve tractography results. We use the calibration procedure for both QBall and PASMRI. For the QBall reconstruction we use spherical harmonic basis functions [70], since the spherical integral can be computed analytically and therefore does not incur the numerical inaccuracies of the radial basis function implementation described in [67]. We use the PASMRI standard settings listed in [15].

5.2.1 Correlation between Hessian anisotropy and fanning in the human brain

We start by testing the hypothesis that the peaks of the PAS or dODF contain more useful information than simply the peak sharpness and direction by generating images of the peak anisotropy of the dominant peaks of the PAS and the dODF in each voxel, as well as the anisotropy of the DT perpendicular to its principal axis. The peak anisotropy images (figure 5.5) generated are colour-coded to show the direction of the anisotropy using the principal eigenvector of the peak Hessian of the spherical functions and the second eigenvector of the DT respectively. Both point in the direction of the largest anisotropy of the peak cross-section, which we hypothesize is the direction of the fibre-spread/uncertainty. In this experiment we use a maximum spherical harmonic order 4 for QBall, which is the simplest spherical harmonic representation that can support multiple peaks. We consider this simplified case before looking at more complex representations because the effects of noise are less problematic.

Figure 5.5 shows the magnitude and direction of the 2D FA of the DT (b) and the peak anisotropy of the dominant peak from dODF (c) and PAS (d) in each voxel. In figures 5.5b and 5.5c, light pixels indicate that the cross-section of the principal peak of the reconstruction is elliptical; dark regions indicate that the peak cross-section is circular. Where there are multiple peaks, figures 5.5b and 5.5c show only the anisotropy of the largest peak. The peak anisotropy at the centre of the corpus callosum (highlighted with the upper box) is low, since the fibres are approximately parallel in this region and any spread is isotropic. Note that this is in stark contrast to the diffusion tensor anisotropy (Fractional Anisotropy) in the corpus callosum, which is usually very high. However, the PAS peaks in the descending motor pathways (highlighted with the left box) have high anisotropy with the largest axis in the posterior-anterior direction (green), which, according to anatomical knowledge [113], is the direction of the fanning of this structure. The dODF peak anisotropy image highlights the fanning structure less clearly than PAS. This is a result of the fourth-order spherical-harmonic representation of the dODF, which cannot model anisotropy in the peak sufficiently well. However, both the PASMRI and QBall peak anisotropy maps broadly agree. In the case of the DT, the FA of the two-dimensional DT orthogonal to the dominant fibre direction generally agrees with the other two images.

5.2.2 Calibration validation

We validate the estimates of the Bingham distribution parameters provided by the calibration mapping by comparison with bootstrap samples from the 8 repeats of the human brain data. We identify 4 regions of interest (ROIs), one containing voxels with highly coherent fibre bundles, one with fibre-crossings, one in a fanning region and one in an isotropic region. Each ROI contains 25 voxels. The ROIs are shown in figure 5.6. Each

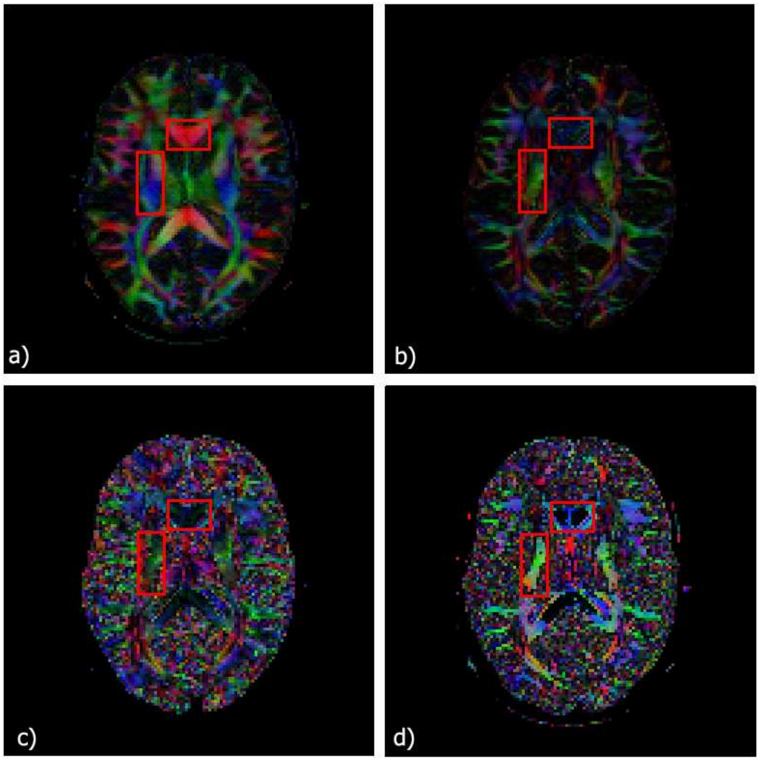

Figure 5.5: images of a) the standard colour-coded principal direction map from the DT weighted by FA of the full three dimensional DT. Red indicates left-right; green indicates front to back; blue top to bottom; intensity is FA. b) Colour-coded map of the second eigenvector weighted by the FA of the two-dimensional DT orthogonal to the dominant fibre direction. c) Colour-coded peak major axis orientation weighted by peak anisotropy for the dominant dODF peak. d) Colour-coded peak major axis orientation weighted by peak anisotropy for the dominant PAS peak. In cases where the PAS or dODF has several peaks, the peak anisotropy of the peak with the greater magnitude is shown.

ROI was extracted from all 8 datasets and we create 100 bootstrap sets of measurements for each voxel by sampling with replacement from the 8 options for each measurement [114]. We reconstruct using PASMRI and QBall (using maximum spherical harmonic orders of both 4 and 6) and estimate the fibre-orientation estimates and associated Hessians for each bootstrap. We then order the peak directions from the bootstraps into populations with similar orientations and store the peak directions corresponding to the largest peak.

To calculate the bootstrap estimate of uncertainty, we fit the Bingham distribution to the bootstrap estimates of the peak direction for the largest peak and find $\zeta_1 = log(-\kappa_1)$, $\zeta_2 = log(-\kappa_2)$ and the 2D FA of the Bingham parameters $\eta_b = FA(\text{diag}(\kappa_1, \kappa_2))$. For the calibration estimates, we find the Bingham parameter estimates for the peak directions of each of the 100 bootstraps using the calibration mapping (equations 5.1.3 and 5.1.3) and calculate the mean of the three measures, $\bar{\zeta_1}$, $\bar{\zeta_2}$ and $\bar{\eta_c}$.

Figure 5.7 plots ζ_1, ζ_2 and η_b against $\bar{\zeta_1}$, $\bar{\zeta_2}$ and $\bar{\eta_c}$ for QBall (orders 4 and 6) and PASMRI. Each marker represents a voxel in one of the ROIs. If the bootstrap and calibration estimates of uncertainty agree, the markers will be on the line $x \simeq y$. In terms of the anisotropy of the Bingham parameters (left column), neither QBall order 4 or QBall order 6 provides compelling results. For both methods, the calibration estimates of $\bar{\eta_c}$ are generally in the range [0, 0.4]. The agreement between bootstrap estimates of η_b and calibration estimates of $\bar{\eta_c}$ for PASMRI is a little better, although in most cases the calibration still underestimates anisotropy in the uncertainty. With regards to the magnitude of the Bingham parameters, the calibration and bootstrap methods broadly agree.

The anisotropy estimates from the dominant peak of the reconstructions, $\bar{\eta_c}$, are generally lower than the corresponding estimates from the bootstrap, η_b. However, in cases where there are several peaks, it is likely that samples will be drawn from both peak directions during tractography. Therefore, we fit a single Bingham to both populations when computing η_b to capture this effect. Specifically, to estimate the uncertainty anisotropy, we fit a Bingham distribution to the set of all peak directions from all 100 bootstraps and compute the 2D FA of the Bingham parameters, η_b. Then, for each bootstrap, we use the calibration to estimate the Bingham parameters. We

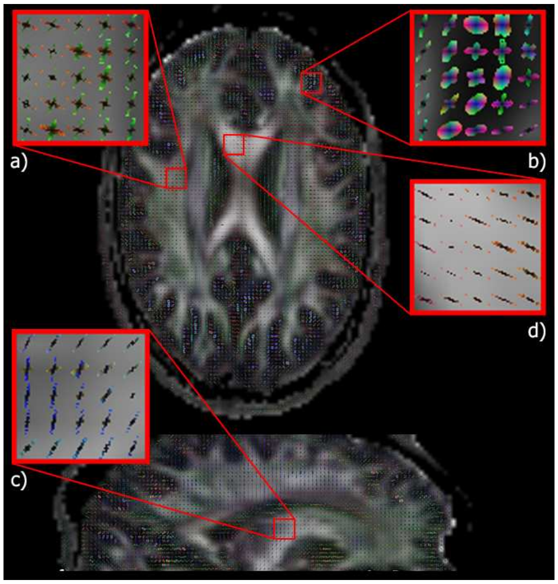

Figure 5.6: The regions of interest used for validating the performance of the fitted mapping (the PAS is shown in each voxel of the ROIs). The ROIs were chosen to include a) crossing fibre, b) grey matter, c) fanning and d) single fibre regions of the brain.

draw 100 samples from all of the Bingham PDFs in each bootstrap, fit a single Bingham PDF to the whole collection of these samples and compute $\bar{\eta_c}$. Figures 5.8a and 5.8b plot η_b against $\bar{\eta_c}$ for each voxel in each ROI for PASMRI and QBall, respectively. As in figure 5.7, each marker represents a voxel in one of the ROIs and markers on the line $x \simeq y$ indicate agreement between the calibration and bootstrap estimates of uncertainty.

For both settings of QBall, η_c (figure 5.8b) are generally very low $(0.1 - 0.2)$ in comparison to η_b, although η_c improves for grey matter and fibre-crossing regions. Neither the fourth-order or sixth-order spherical-harmonic basis function representation of the dODF cannot adequately capture the anisotropy in the peaks of the QBall dODF. The PASMRI calibration gives better results (figure 5.8a), with η_b and $\bar{\eta_c}$ generally agreeing. Some disagreement occurs for the high FA samples, where bootstrapping gives much higher anisotropy. Occasionally, when the uncertainty is anisotropic, PASMRI produces small peaks in the perpendicular direction rather than a single elliptical peak. The small spurious peak causes unexpectedly low $\bar{\eta_c}$ in the main peak. Future work may correct for this by including the peak height in the calibration map-

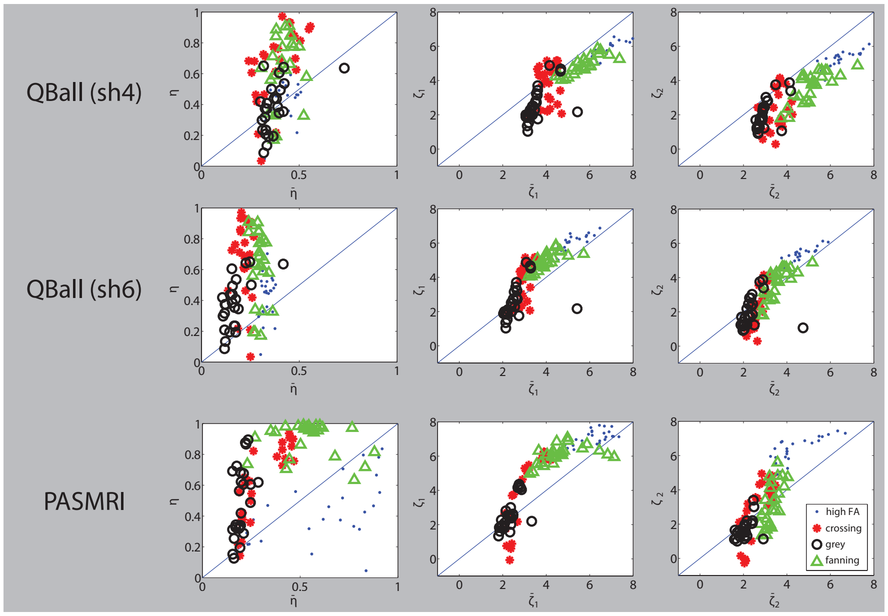

Figure 5.7: Validation results for calibration mapping estimates of the Bingham parameters. Each plot compares bootstrap estimates of uncertainty to the mean estimate from the calibration mapping. The left column shows plots comparing estimates of the anisotropy of the Bingham parameters, the centre column shows plots comparing estimates of κ_1 and the right column shows plots comparing estimates of κ_2.

ping.

5.2.3 Tractography

We run PICo tractography on the human brain data using the new multiple-fibre PICo algorithm in conjunction with PASMRI and QBall (both order 4 and order 6) and compare the results to those of the algorithm described in [43]. The tractography process was started from a manually defined region of interest at the base of the corticospinal/corticopontine tracts (see Figure 5.9, inset). The dominant pathway from the seed region runs inferior-superior into the corona radiata, where the descending motor pathway fibres cross lateral fibres projecting from the corpus callosum.

Figure 5.9 shows the results of tractography using the multi-fibre algorithm with both PASMRI and QBall as well as results from the DT algorithm introduced by [36] using both the Watson and Bingham distributions to model uncertainty. As expected, the original DT-PICo algorithm fails at fibre-crossings, which results in large holes in the descending motor pathway reconstructions. In the DT case, the connection indices

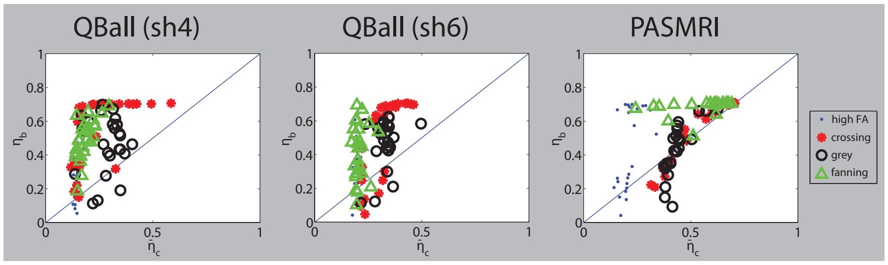

Figure 5.8: Validation results for calibration mapping estimates of the Bingham parameters. a) and b) are plots of the mean anisotropy of the Bingham parameters, $\bar{\eta}_c$, estimated by our mapping against the anisotropy of the Bingham parameters, η_b, estimated using bootstrapped data for both PAS and QBall respectively.

in the descending motor pathways vary widely, as opposed to the connection indices from PAS-PICo and QBall-PICo, which are more consistent over the tract. For QBall, the PICo results have fewer holes than the DT-PICo results, since the QBall dODFs are able to model multiple peaks. However, for QBall order 4 the reconstruction of the descending motor pathways generally fails to reach the cortical layer. The results of the PAS-PICo and QBall order 6 tractography experiments are more favourable. Not only do the algorithms correctly map the fanning structure of the descending motor pathways, the reconstructed tracts extend to the cortical layer. The PAS-PICo results show fewer holes in the descending motor pathways than those from either order 4 or order 6 QBall PICo. These results reflect the greater ability of PASMRI to resolve fibre-crossings with a small number of measurements over QBall [32]. The difference map from the PAS-PICo experiment shows that using the information about the shape of the peak results in a more even index of connection over the descending motor pathways, although the overall magnitude of the connection indices is lower.

5.3 Discussion and Conclusions

We have introduced a generalization of the PICo algorithm that allows us to use more of the information contained in the fibre-orientation distributions to improve tractography through complex white-matter structures. We have demonstrated that the algorithm described here works for both PASMRI and QBall. Since the algorithm exploits infor-

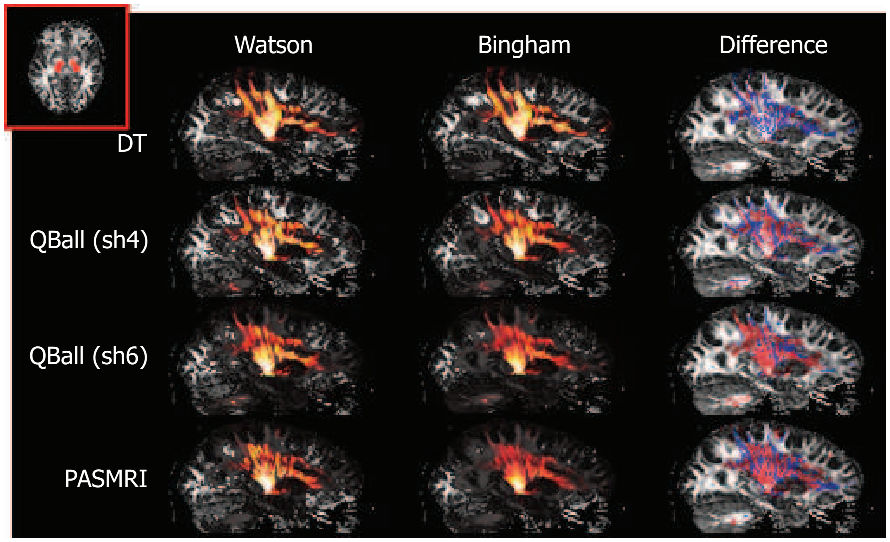

Figure 5.9: PICo tractography results using a DT reconstruction (top row), QBall reconstruction (middle row) and PASMRI reconstruction (bottom row). The difference map shows where the probability of connection is higher when using the Bingham distribution (blue) or the Watson distribution (red). The seed ROIs are shown in the axial view in the top-left corner (inset).

mation captured by the ODF, it is independent of reconstruction technique and extends easily to similar algorithms such as Spherical Deconvolution (see chapter 3). The bootstrap validation shows that the FA of the Bingham parameters from the PASMRI calibration and the bootstrap estimates approximately correlate. For order 4 QBall-PICo, the choice of PDF used to model uncertainty makes little difference to the resulting PICo connectivity map. This results from using a fourth-order spherical-harmonic basis function representation of the dODF. The connectivity map from order 6 QBall-PICo is more favourable, although the bootstrap validation still suggests that the ODF is still unable to model anisotropic peaks. Using a spherical radial basis function representation of the dODF or higher-order SH may allow peak anisotropy to be captured better. PAS-PICo gives the most compelling results. The difference maps in figure 5.9 demonstrate clear changes by modelling anisotropy. The PAS-PICo difference map clearly shows that using both the shape and sharpness of the PAS peaks results in a higher connection probability in regions of fibre crossings. Utilizing other information in the peaks of multi-fibre reconstructions, such as the height of the peaks of functions, in PICo may improve results further. The bootstrap validation highlights one weakness of the PASMRI reconstruction algorithm, which is that it sometimes produces a spurious perpendicular peak in fanning structures. Future work will investigate and compare the ability of other multiple fibre reconstructions to capture the shape of fanning and bending structures. For example, we can extend the framework described in the previous chapter to determine how well different algorithms model complex fibre configurations such as fannings and bendings.

Chapter 6

Refining Multiple-Fibre PICo

In the previous chapter we introduced a method for exploiting the peak shapes of multiple-fibre reconstructions to improve estimates of uncertainty in PICo tractography. Since its initial publication in 2007, it has become the standard multiple-fibre reconstruction PICo method in the popular Camino toolkit [83]. However, the histogram-based calibration procedure has several limitations. First, the choice of bin size affects the mapping and needs to be chosen empirically for each new calibration. Make the bins too large and peaks with different shapes will be combined into a single bin; make the bins too small and there will not be enough samples to obtain a reliable estimate of the distribution parameters. Second, bins that do not contain enough samples are not used to estimate the parameters of the calibration mappings, which wastes useful information. A consequence of this second point is that the histogram-based calibration procedure requires a large amount of data over all peak shapes in order to generate a reliable mapping. Several methods may improve the calibration. For example, instead of binning fibre-orientation estimates into fixed bins, we could choose the k-nearest neighbours [115] to given Hessian eigenvalues. Alternatively, we could dynamically alter the sizes of the bins to reduce the effects they have on the calibration surfaces.

In this chapter we describe a new calibration procedure that avoids using a binning procedure completely by parameterising the mapping from peak shape to the distribution parameters and fitting it to all the data at once. This not only allows us to avoid any requirement for choosing parameters, but it also exploits all of the fibre-orientation estimates in the calibration dataset. Furthermore, it allows us to use a smaller calibration dataset, since we no longer need to fit individual distributions explicitly.

Finally, we present some exploratory work on a method which aims to model the fODF, as opposed to the uODF, in each voxel.

6.1 Maximum Likelihood Calibration

In this section we describe the maximum likelihood approach to learning a calibrated mapping between peak shape and the parameters of a distribution used to model uncertainty. Reconstructing synthetic data using a multi-fibre reconstruction algorithm gives us two useful pieces of information: the shape of each peak of the ODF and the deviation angle between the peak direction (our fibre orientation estimate) and the true fibre-orientation. The goal of the calibration procedure is to find the mapping between features of the ODF and distribution parameters from the deviations of the calibration data. The calibration mapping uses features of the ODF to predict the distribution parameters that model the uncertainty of the fibre-orientation estimates. For example, in the previous chapter we use the eigenvalues of the peak Hessian to estimate the Bingham parameters. The calibration mapping consists of calibration surfaces for each of the n distribution parameters, i.e. $\kappa_1, ..., \kappa_n$. The calibration procedure alters the parameters of the mapping surfaces to maximize the likelihood of all the deviations in the training data. Specifically, given N samples we aim to maximise the log-likelihood function

$$L = \sum_{i=1}^{N} \log \left(p(\theta_i, \phi_i | \kappa_1(\lambda_1, \lambda_2; c_1^{(1)}, ..., c_M^{(1)}), ..., \kappa_n(\lambda_1, \lambda_2; c_1^{(n)}, ..., c_P^{(n)})) \right) \tag{6.1}$$

where p gives the likelihood of deflection θ_i and ϕ_i given the Bingham parameter estimates from $\kappa_1, ..., \kappa_n$; $c_1^{(1)}, ..., c_M^{(1)}, ..., c_1^{(n)}, ..., c_P^{(n)}$ are the coefficients of the calibration mappings and λ_1 and λ_2 are the Hessian eigenvalues of the peak.

The full calibration procedure consists of the following steps:

1. choose calibration dataset
2. synthesize data
3. fit ODF to synthetic data
4. extract peak shape and orientation information
5. choose uncertainty model

6. choose surface model for calibration mapping
7. pre-process calibration data
8. fit surface to maximize 6.1

The first five steps are identical to the corresponding steps in the histogram-based calibration described in the previous chapter. We will therefore focus on the last three steps in the remainder of this section. In particular, we will examine different calibration mappings and alternative strategies for processing the calibration data to match fibre-orientation estimates to their corresponding fibre orientations and remove outliers.

6.2 Choosing the model of uncertainty and mapping representation

We consider two distributions to model the uncertainty of each ODF peak: the Watson and Bingham distributions. For each of these distributions we need to define suitable mapping parameterizations. Here, we consider a 1D mapping for the Watson distribution parameter and two 2D mappings for the Bingham parameters. We define several mapping parameterizations below.

For the Watson distribution, we map from the peak sharpness to the concentration parameter, κ, using the mapping (*wm1*)

$$\kappa_1 = c_1 + c_2 \log(\mathrm{Tr}(H)). \tag{6.2}$$

The *wm1* mapping allows the Watson distribution parameter, κ, to be both positive and negative. This mapping also only has two parameters to optimize, which should make the calibration robust.

For both of the Bingham calibrations, we use a separate mapping for each of the distribution parameters, κ_1 and κ_2. The first calibration mapping for the Bingham is the unconstrained mapping (*bm1*)

$$\kappa_1 = -\exp(c_1^{(1)} + c_2^{(1)} \log(\lambda_1) + c_3^{(1)} \log(\lambda_2)), \tag{6.3}$$

$$\kappa_2 = -\exp(c_1^{(2)} + c_2^{(2)} \log(\lambda_1) + c_3^{(2)} \log(\lambda_2)), \tag{6.4}$$

where we set $\kappa_1 = \kappa_2$ if $\kappa_2 < \kappa_1$ to ensure that the Bingham parameters are valid (i.e. that $\kappa_1 <= \kappa_2 <= 0$). Neither of the *bm1* mapping surfaces are constrained, which makes the mapping flexible.

The second mapping we consider is the constrained mapping (*bm2*)

$$\kappa_1 = -\exp(c_1^{(1)} + c_2^{(1)} \log(\lambda_1) + c_3^{(1)} \log(\lambda_2)), \tag{6.5}$$

$$\kappa_2 = \kappa_1 + \exp(c_1^{(2)} \lambda_1 \ + c_2^{(2)} \lambda_2). \tag{6.6}$$

The constrained (*bm2*) mapping has fewer free parameters than the unconstrained (*bm1*) mapping, which may make the calibration more robust. However, using a constrained mapping for κ_2 will limit the shapes of the distributions that can be captured by the calibration and therefore may bias estimates of the distribution parameters.

6.3 Calibration data

We construct a separate calibration mapping for one- and multiple-fibres. This means that each mapping only models uncertainty for a subset of the data, which should result in more accurate estimates of uncertainty from the calibration. Prior to fitting the mapping to the calibration data, we must make choices on how to split the dataset into one- or multiple-fibre subsets, match the fibre-orientation estimates to the true fibre directions and reduce the effect of outliers. We start this section by discussing how to separate the calibration dataset into one-fibre and multiple-fibre voxels so that the resulting calibration mappings provide a more representative estimate of uncertainty. We then look at how to match fibre-orientation estimates to the true fibre orientations. In particular, we focus on cases where the number of estimates (i.e. ODF peaks) does not agree with the actual number of fibre populations. Finally, we consider methods for reducing the effect of outliers on the calibration mappings.

6.3.1 Sorting samples into one- and multi-fibre calibration datasets

The calibration dataset is constructed from test functions using one and two tensor models; the dataset contains voxels with one and two fibre directions. However, the number of fibre-orientation estimates from the reconstructed ODFs do not necessarily match the number of fibre directions. Therefore, when separating the calibration data we must decide which data is used for the one-fibre calibration and which data is used for the multi-fibre calibration. In the previous chapter we split the calibration dataset into two subsets according to the number of tensors used to create the test function. However, we do not know the true number of fibre orientations in each voxel of a brain volume, just the estimated number of fibres. Therefore, the uncertainty estimates from the original mapping may be biased because the set of voxels used for creating the calibration mapping will not be reflective of the voxels for which the mapping estimates the uncertainty. We present two alternatives below.

Separate A more suitable approach to the one used in the previous chapter is to separate the datasets into different subsets based on whether the voxel contains a single fibre-orientation estimate or multiple estimates. Therefore, if reconstructed ODF has a single peak, the corresponding fibre-orientation estimate is used in the one-fibre mapping. Conversely, if the ODF has multiple peaks, the corresponding fibre-orientation estimates are used in the multiple-fibre mapping. The benefit of this approach is that both the calibration and tractography algorithms use the same criteria for classifying each voxel. In addition to this, using separate mappings for one- and multiple-fibre voxels potentially makes the calibration procedure more flexible.

Combined Alternatively, we can bypass the problem of subdividing the calibration dataset by using the whole dataset, consisting of both one- and multiple-fibre voxels, to learn a single combined mapping. This simplifies the calibration process, since there is no longer a need to classify voxels as one fibre or multiple fibre before predicting uncertainties. A potential limitation of this approach is that a single mapping may not be flexible enough to model accurately the uncertainties for both one fibre and multiple fibre voxels.

6.3.2 Matching fibre-orientation estimates to true fibre-orientations and dealing with bias

Multi-fibre reconstructions often contain spurious peaks (false-positives) or model several fibre-orientations with a single peak (false-negatives). Reconstructions exhibiting these artefacts have a detrimental effect on the calibration if they are not removed or down-weighted. Some spurious peaks can be thresholded out, which may alleviate the problem to some extent. However, there are many voxels where spurious peaks remain, useful fibre-orientation estimates are removed, or the reconstruction provides a misleading estimate of the fibre orientation (i.e by modelling several fibre orientations by a single peak). The false-positives and false negatives cause several problems. Firstly, matching fibre-orientation estimates to true fibre orientations becomes problematic because there is not a one-to-one correspondence. Another problem is that errors in reconstruction may adversely influence the resulting mapping if they are not dealt with appropriately. In this section we propose several methods for matching fibre-orientation estimates to the true fibre orientations and for dealing with reconstructions that may introduce bias into the mapping.

Let us consider the case where two fibre orientations are modelled as a single peak in the reconstruction and compare that to a case where both fibre orientations are correctly modelled with separate peaks. For both of these configurations we expect to see anisotropic distributions, oriented so that the distribution of fibre orientations is greater in the plane of the crossing, with the fibre-orientation estimates clustered around the fibre directions. However, when the directions are modelled by a single peak this is not the case. Although the peak shape reflects the underlying fibre configuration, the distribution of fibre orientation estimates is no longer clustered around the fibre directions.

Figure 6.1 illustrates both cases using fibre-orientation estimates from PASMRI reconstructions. The fibre orientations are shown by red markers. In the voxels that contain a 60° crossing (left), the PAS generally has two peaks and we observe an anisotropic distribution of fibre-orientation estimates clustered around the two fibre orientations. For voxels that contain 20° crossings (right), only a single fibre orientation is predicted. The fibre-orientation estimates for the 20° case are tightly clustered around a point half way between the two fibre orientations. This effect introduces a bias into the calibration data because the true deflections are much greater than the variance of the single fibre-orientation estimate.

These biased estimates need to be downweighted or removed from the calibration dataset. We outline several methods for downweighting or removing these estimates below.

All The first approach to mapping fibre-orientation estimates to the fibre directions ap-

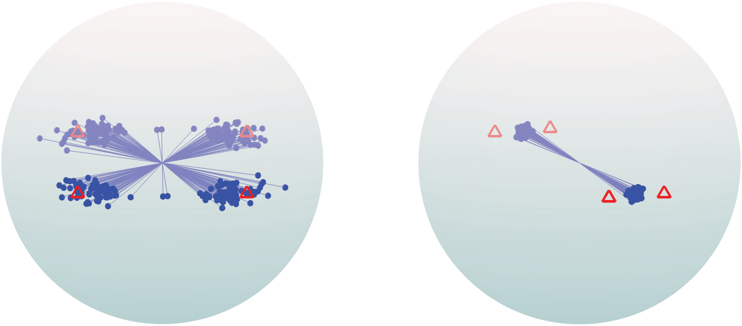

Figure 6.1: Uncertainty of fibre-orientation estimates from PASMRI reconstructions of synthetic data for 60° crossings (left) and 20° crossings (right). For each configuration, we generate 50 noisy trials using a two-tensor model of diffusion and plot the fibre-orientation estimates (blue markers) on the sphere. We also plot the fibre orientations (red markers) for reference.

plies no downweighting. Specifically, we assign each fibre-orientation estimate to the closest fibre direction and allow the same estimate to be matched to both fibre directions when there is only a single estimate but two fibre directions. This approach has the benefit of using all of the available data. However, it makes no attempt to remove the biased estimates described above. Therefore, the resulting mapping will overestimate the uncertainty.

Closer In the second approach, we assign each fibre-orientation estimate to the closest fibre-direction as before, but here we match the estimate only to the closer of the two fibre orientations when a single peak is recovered from two fibre orientations. This reduces the contribution of the misclassifications to the one-fibre mapping, although the resulting mapping still overestimates the uncertainty.

noFP The third approach rejects all of the false positives (i.e. remove all voxels where the number of fibre-orientation estimates does not match the number of fibre orientations). This removes a lot of the training data, but also culls a most of the spurious and biased samples.

6.3.3 Outlier rejection

In addition to the methods described in section 6.3.2, we consider the use of outlier rejection to remove spurious samples from the ‘all’ and ‘closer’ datasets used to calibrate the mapping between the distribution parameters and the peak shape. Outlier rejection is not applied to the ‘noFP’ dataset, since many of the outliers have been removed already.

To remove the outliers from a dataset, we perform an initial calibration using the procedure described above section 6.1 with both the ‘all’ and ‘closer’ datasets. We then use the calibration mapping to calculate the likelihood of each sample in the dataset. Finally, we remove samples that have a likelihood lower than a manually selected threshold and refit the mapping to the remaining samples.

Figure 6.2 shows examples histograms of the log-likelihood of each sample of a complete calibration dataset for a PASMRI calibration. The histograms shows a distribution that has a very long tail to the left where the likelihood of the samples is very close to zero. These samples are considered outliers in the dataset and thresholded out.

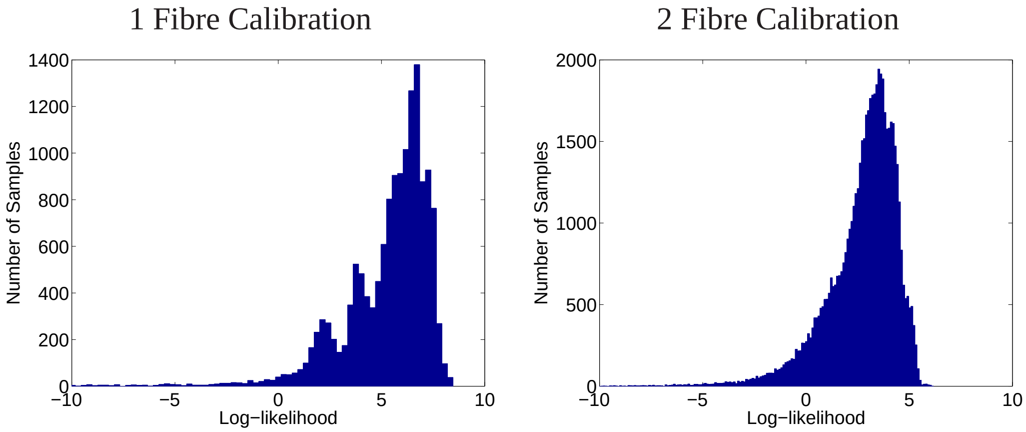

Figure 6.2: Histograms showing the likelihood of each sample in a single-fibre (left) and a two-fibre (right) calibration dataset (‘all’) as estimated using PASMRI and the *bm1* calibration mapping.

6.4 Fitting

We use the matlab function fminunc to search for the mapping parameters that minimize the negated likelihood from equation 6.1. The function uses an unconstrained

Broyden-Fletcher-Goldfarb-Shanno (BFGS) quasi-Newton method [116, 117, 118, 119] for the minimization. At each iteration, we find the local gradient numerically.

To overcome local minima, we run the algorithm 20 times, with different starting points drawn from a zero-mean normal distribution. We set the standard deviations of the distributions on the initial setting of each parameter to a similar magnitude as the parameter settings obtained using the histogram-based approach in chapter 5. The algorithm converges on the same solution and terminates having minimised the objective function for approximately 60% of the runs and we assume that solution is the global minimum.

6.5 Experiments

In this section we investigate the effects of outliers on the maximum likelihood calibration and compare the variants of the calibration procedure using a bootstrap validation and PICo tractography. Details of the method used to generate the bootstrap data and the measures calculated are provided in sections 5.2.2 and 5.2.3 respectively. We use both PASMRI and Spherical Harmonic QBall with a maximum spherical harmonic order of 6 to reconstruct the data.

6.5.1 Effect of synthetic data artefacts on a calibration between peak sharpness and uncertainty

We start by examining the effects of outliers on calibrations between uncertainty and peak sharpness (i.e. using the Watson distribution to predict uncertainty). We anticipate that outliers in the calibration dataset will add a large bias the calibration mapping. In particular, we expect to see an over-estimation of uncertainty.

To test this hypothesis, we plot the deflection angle between the fibre orientation and the corresponding peak orientation against the peak sharpness for two datasets (the ‘all’ and ‘noFP’ datasets) and compare the plots. If there are no outliers, we expect the deflection angles to decrease as the peak sharpness increases. The ‘noFP’ dataset will reject most outliers, so we can consider the plot from this dataset as close to the ground truth. We reconstruct the calibration data using PASMRI. The samples are aligned with the z-axis using the approach described in section 5.1.3.

Figure 6.3 plots the deflection angle of the samples against peak sharpness for the

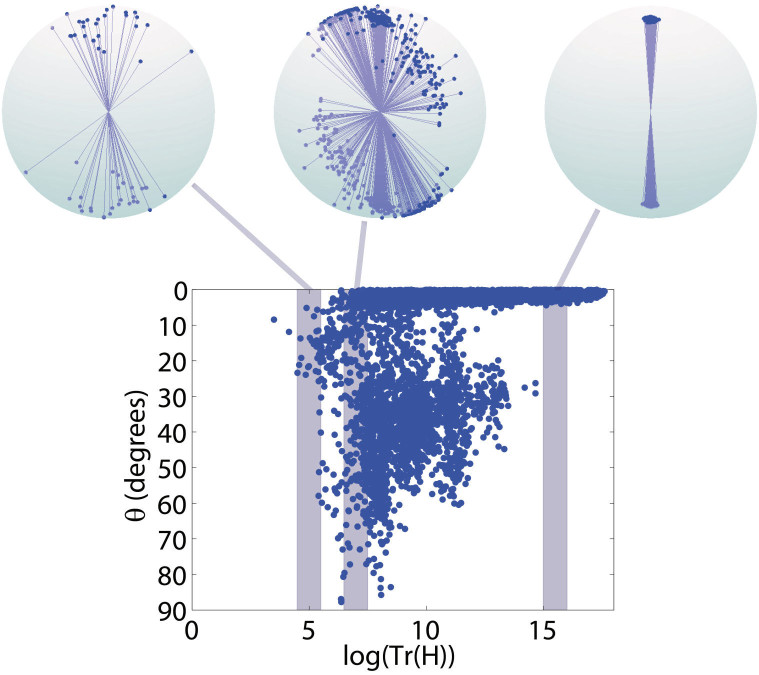

Figure 6.3: Plots the deflection angle of each sample in the single-fibre ‘all’ calibration dataset against the corresponding peak sharpness. The distribution of samples on the sphere are shown for three ranges of peak sharpness (top row). PASMRI was used to reconstruct the data.

single-fibre ‘all’ calibration dataset. In the scatter plot, there are two clusters of samples. One cluster consists of samples with small deflection angles. The other consists of samples with far larger deflection angles and is limited to the middle of the range of peak sharpness. Samples from several ranges of peak sharpness are shown above the plot of deflection angles. The samples from broad peaks (left) have a large distribution whereas sharp peaks (right) are tightly clustered around the z-axis. In contrast, peaks with a sharpness in the middle of the range (centre) have a broad distribution with anisotropic contours. This is caused by voxels that contain two true directions which have produced a single anisotropic peak. As suggested in section 6.3.2, this configuration yields deflection angles that are not representative of the underlying uncertainty.

Figure 6.4 shows a plot similar to the one in figure 6.3 but using the ‘noFP’ dataset. Unlike figure 6.3, the scatter plot for this dataset only contains a single cluster consisting of samples with small deflection angles; the second cluster of samples with large deflection angles no longer appears. The distributions of samples from broad peaks (left) and sharp peaks (right) are similar to those from the 'all' dataset. However, the distribution of samples in the middle of the range (centre) is far more concentrated around the fibre-orientation. In addition to this, the contours of the distribution are not anisotropic and the variance is lower than for the equivalent range in figure 6.3.

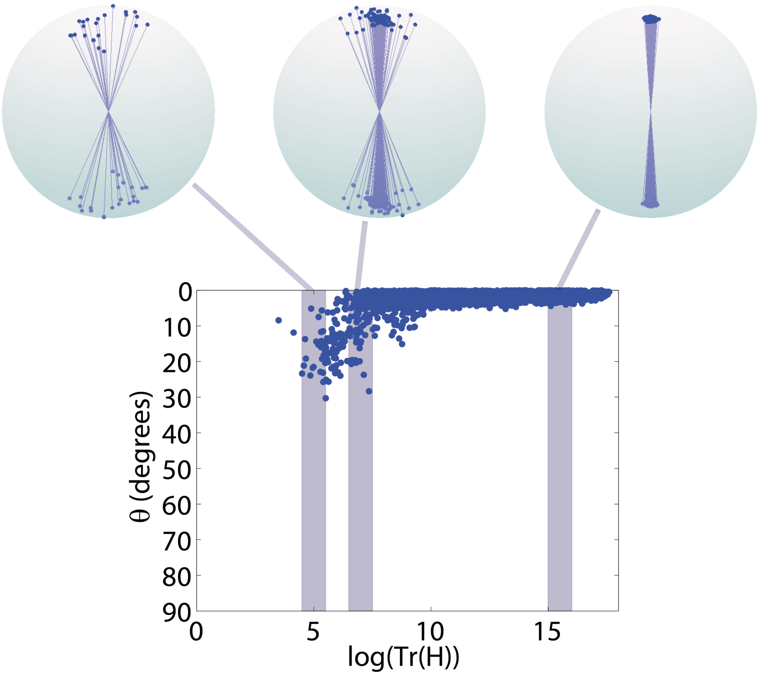

Figure 6.4: Plots the deflection angle of each sample in the single-fibre 'noFP' calibration dataset against the corresponding peak sharpness (the trace of the peak Hessian, as in chapter 5). The distribution of samples on the sphere are shown for three ranges of peak sharpness (top row). PASMRI was used to reconstruct the data.

The anisotropic distribution of samples from ODFs with a single peak that models two fibre directions provides some information about the spread of fibre orientations but does not reflect the actual uncertainty of the fibre-orientation estimates. These samples greatly increase the uncertainty in the middle of the range of peak sharpnesses (figure 6.3, centre), which increases the uncertainty estimates for the majority of fibre-orientation estimates when using a linear mapping during tractography. The effect is particularly noticeable for calibrations where uncertainty is estimated using peak sharpness (for example, when using the *wm1* mapping). Outlier rejection reduces the effect of these outliers slightly, but they still have a large affect the *wm1* mapping. We investigate the effects of outlier rejection in more detail in the following experiment (section 6.5.2). We therefore recommend using the 'noFP' dataset when calibrating between peak sharpness and uncertainty. Although this effect is important when considering mapping uncertainty to peak sharpness, it also affects calibration mappings between peak shape and uncertainty.

6.5.2 Calibration estimates of uncertainty vs bootstrap estimates

Here we use the bootstrap data from the previous chapter to compare bootstrap estimates of uncertainty to estimates from the maximum likelihood calibration procedure described in section 6.1. We expect bootstrap estimates of uncertainty to broadly agree with the calibration estimates of uncertainty.

We have three main hypotheses: firstly, we expect outlier rejection to improve the agreement between the bootstrap estimates of uncertainty with those from the calibration mapping. Secondly, the constrained (*bm2*) calibration mapping has less parameters which will result in a calibration that is less likely to get trapped in local minima. Therefore, we hypothesise that the *bm2* mapping will provide better agreement with the bootstrap than the *bm1* mapping. Thirdly, we hypothesise that separate mappings for single fibre and multi-fibre voxels will provide a more flexible mapping than a single combined mapping for all voxels. Separate mappings are only fitted to a subset of the data and may therefore reduce any problems caused by any non-linearity in the relationship between the peak shape and distribution parameters. If this is the case, estimates of uncertainties from separate mappings will have a better agreement with the bootstrap estimates than those from the combined mappings.

In this experiment, we focus on the dominant peaks and compare the predicted Bingham parameters from the bootstrap with those from the calibration mappings. Details of the method used to generate the bootstrap data and the measures calculated are provided in section 5.2.2. We reconstruct each of these voxels and compare the bootstrap estimates of the Bingham anisotropy, η_b, and the Bingham parameters, ζ_1 and ζ_2 to the corresponding mean calibration estimates in each voxel, $\bar{\eta}_c$, $\bar{\zeta_1}$ and $\bar{\zeta_2}$ (see section 5.2.2).

6.5.2.1 Effect of outlier rejection on calibration

First, we test the hypothesis that outlier rejection improves the agreement between calibration estimates of uncertainty with the bootstrap estimates. For this experiment we use the 'all' dataset and separate *bm1* calibration mappings for the single- and multi-fibre voxels. The outlier threshold is chosen manually for each calibration.

Figure 6.5 shows plots of $\bar{\eta}_c$ (left column), $\bar{\zeta}_1$ (centre column) and $\bar{\zeta}_2$ (right column) of the calibration estimate against the corresponding estimate for the bootstrap. For both PASMRI (top two rows) and QBall (bottom two rows) we show plots before and after outlier rejection. The PASMRI plots without outlier rejection (top row) shows good agreement between the calibration and bootstrap estimates of anisotropy in uncertainty ($\bar{\eta}_c$ and η_b respectively) for crossing and fanning fibres. However, the calibration estimates of $\bar{\zeta}_2$ are considerably lower than the estimates of ζ_2 from the bootstrap. Applying outlier rejection (second row) yields similar agreement between the calibration and bootstrap estimates of anisotropy in the uncertainty but provides a closer agreement between the calibration estimate of $\bar{\zeta}_2$ and bootstrap for ζ_2. There is also closer agreement between the calibration estimate of $\bar{\zeta}_1$ and bootstrap for ζ_1.

The QBall calibration, without outlier reduction (figure 6.5, third row), yields poor agreement between the bootstrap estimates of ζ_1 (centre panel) and $\bar{\zeta}_2$ (right panel) and the corresponding calibration estimates. Specifically, the calibration estimates of the Bingham parameters are very low compared to the bootstrap estimates. There is, however, some agreement between the calibration and bootstrap estimates of anisotropy in uncertainty (left panel) for fanning and high FA voxels. The QBall calibration with outlier rejection (fourth row) has good agreement with the bootstrap for estimates of ζ_1 and ζ_2 (centre and right panels respectively). However, there is poor agreement between the calibration and bootstrap estimates of anisotropy in uncertainty (left panel).

Outlier rejection improves the agreement between the calibration mapping predictions of the Bingham parameters and the bootstrap predictions for both reconstruction algorithms. In particular, the agreement between the calibration estimates of $\bar{\zeta}_2$ and bootstrap estimates of ζ_2 is improved. For PASMRI, the Bingham anisotropy appears to agree with the bootstrap estimates in the crossing fibre voxels, fanning voxels and some of the grey matter voxels both before and after outlier rejection. In comparison, QBall underestimates the Bingham anisotropy, although the agreement is worse after outlier rejection.

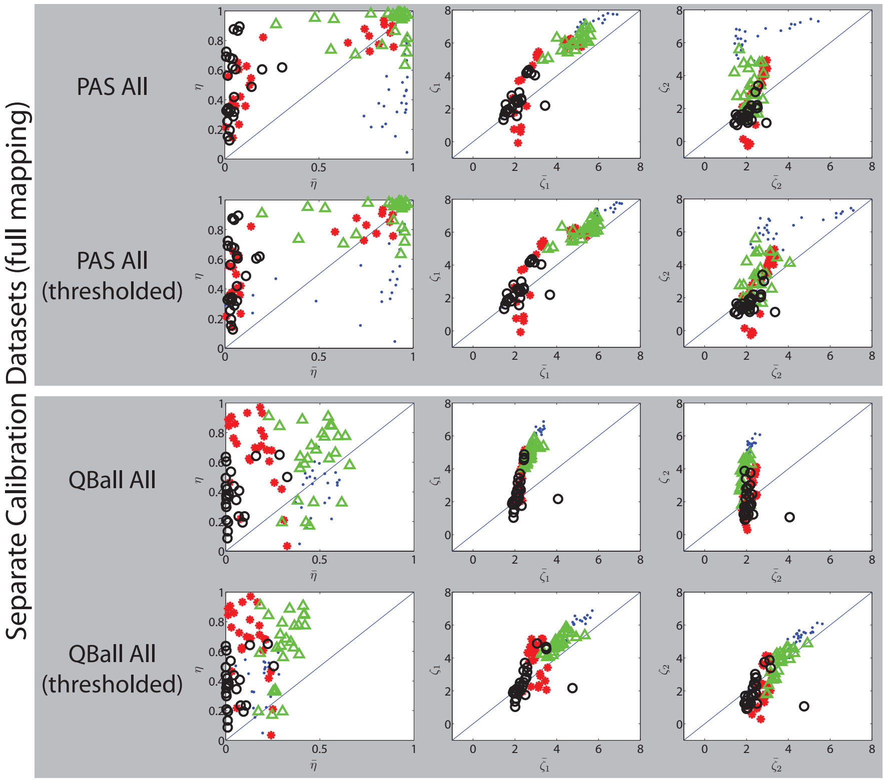

Figure 6.5: Comparison of uncertainty estimates from maximum-likelihood calibration mappings with bootstrap estimates for PASMRI (top two rows) and QBall (bottom two rows). Each plot compares bootstrap estimates of the uncertainty to the mean estimate from the calibration mapping. The left column shows plots comparing estimates of the anisotropy of the Bingham parameters, the centre column shows plots comparing estimates of κ_1 and the right column shows plots comparing estimates of κ_2. For each reconstruction algorithm, we plot results before (upper row) and after (lower row) outlier removal. All mappings use the 'all' dataset and the *bm1* mapping.

6.5.2.2 Unconstrained vs constrained calibration mappings

Next, we test the hypothesis that the constrained (*bm2*) calibration mapping is more robust than the unconstrained (*bm1*) calibration mapping. If this is the case, the agreement between the bootstrap estimates of uncertainty and calibration estimates should be at least as good for the *bm2* mapping as it is for the *bm1* mapping. We use the 'noFP' dataset and separate mappings for one- and multi-fibre voxels for all of the calibrations.

Figure 6.6 shows plots bootstrap estimates of the measures against calibration estimates from the ‘noFP’ dataset for PASMRI (top two rows) and QBall (bottom two rows). For PASMRI, the unconstrained mapping predicts a large range of Bingham anisotropy (top row, left panel) and there is a good agreement with the bootstrap estimates of anisotropy for crossing and fanning voxels although the calibration underestimates anisotropy for some voxels, particularly grey matter and high FA. There is also good agreement between the calibration estimates of $\bar{\zeta_1}$ and bootstrap estimates of ζ_1 (top row, centre panel) as well as ζ_2 and $\bar{\zeta_2}$(top row, right panel). The constrained mapping gives far higher estimates of anisotropy than the bootstrap for most grey matter and crossing fibre voxels (second row, left panel). One reason for this is that the *bm2* mapping is unable to model $\kappa_1 = \kappa_2$. This is demonstrated by the example mappings in figure 6.7. In this illustration the blue surface represents the calibration mapping for κ_1 and the green surface represents the mapping for κ_2. Since $\lambda_1 < \lambda_2$, only the parts of the mapping that meet this requirement are used. Both calibration mappings predict high uncertainty when peaks are broad ($\log(\lambda_1) = \log(\lambda_2) = 0$) and low uncertainty when the peaks are sharp ($\log(\lambda_1) = \log(\lambda_2) = 15$). However, the surfaces should intersect where $\lambda_1 = \lambda_2$ (i.e. the Bingham distribution should be isotropic when the peak shape is isotropic). However, due to the constraint on κ_2, the surfaces for *bm2* will predict a large amount of anisotropy, even when $\lambda_1 = \lambda_2$. This problem is less apparent for the *bm1* mapping.

The QBall *bm1* mapping estimates of $\bar{\zeta_1}$ and $\bar{\zeta_2}$ agree with the bootstrap estimates of ζ_1 (third row, centre panel) and ζ_2 (third row, right panel). However, the mapping is does not capture the full anisotropy in the uncertainty (third row, left panel) except for the grey matter voxels and a few of the crossing fibre voxels. The QBall *bm2* estimates of $\bar{\zeta_1}$ and $\bar{\zeta_2}$ agree with the bootstrap estimates of ζ_1 (fourth row, centre panel) and ζ_2 (fourth row, right panel). One outlier with $\bar{\zeta_2} = -14$ has been removed from the QBall *bm2* plot to improve visualisation. Estimates of $\bar{\eta_c}$ are smaller than η_b, although as η_b increases, $\bar{\eta_c}$ tends to increase as well. However, $\bar{\eta_c}$ is always greater than 0 (i.e. the calibration always predicts some anisotropy).

Overall, the full (*bm1*) calibration mapping shows closer agreement to the bootstrap than the constrained (*bm2*) mapping. Therefore, we recommend using the *bm1* mapping to map between peak shape and uncertainty.

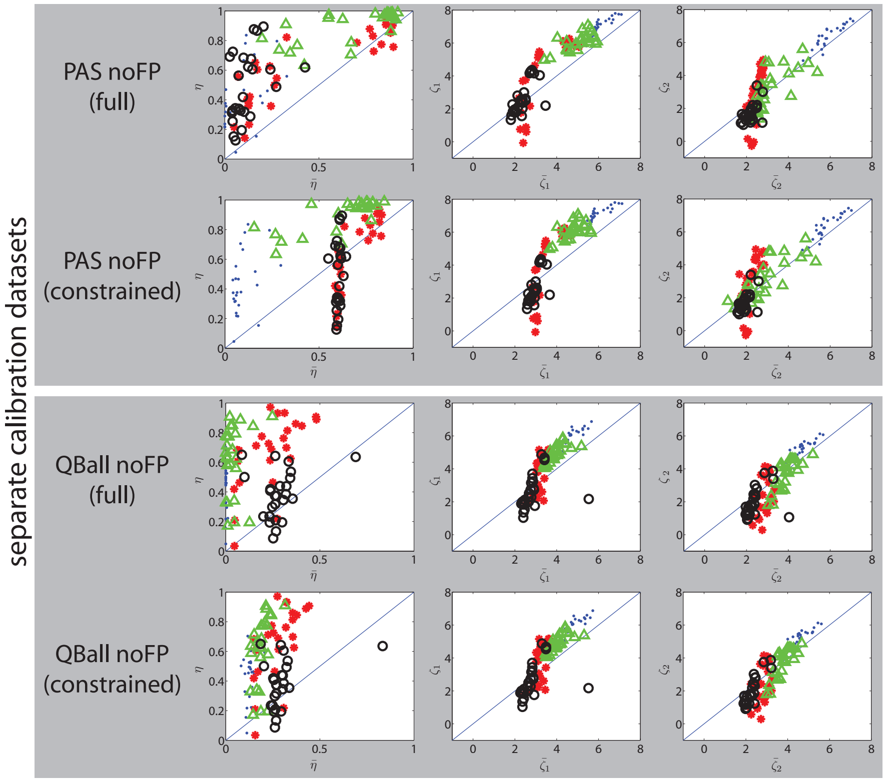

Figure 6.6: Comparison of uncertainty estimates from maximum-likelihood calibration mappings estimates against bootstrap estimates for PASMRI (top two rows) and QBall (bottom two rows). Each plot compares bootstrap estimates of the uncertainty to the mean estimate from the calibration mapping. For each reconstruction algorithm, we plot results using the *bm1* mapping (upper row) and *bm2* mapping (lower row). All calibrations use the ‘noFP’ dataset and generate separate mappings for one-fibre and multi-fibre voxels.

6.5.2.3 Separate vs combined calibration mappings

Finally, we test the hypothesis that ‘separate’ mappings are more flexible than ‘combined’ mappings. If this is the case, there should be better agreement between the calibration estimates of uncertainty and bootstrap estimates, especially for voxels with a single fibre orientation (i.e. high FA and some fanning voxels). For all variants we use the *bm1* mapping with outlier rejection and the ‘closer’ dataset.

Figure 6.8 shows plots comparing both ‘separate’ and ‘combined’ mapping estimates of uncertainty to the bootstrap estimates for PASMRI (top two rows) and QBall (bottom two rows). Estimates of $\bar{\eta}_c$ for PASMRI using ‘separate’ calibration mappings

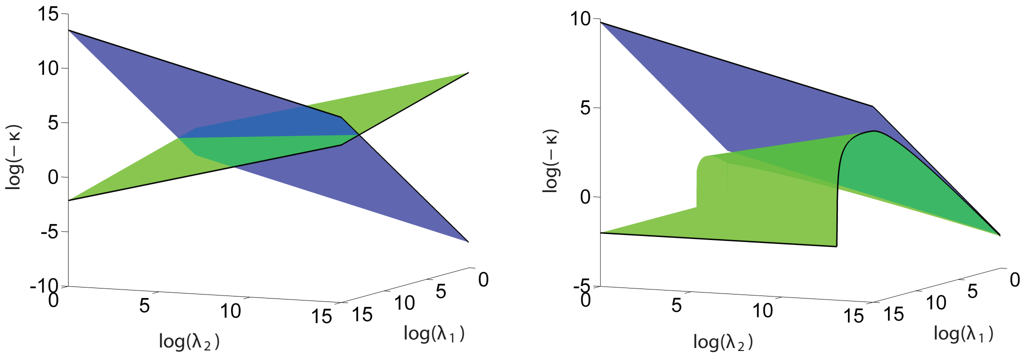

Figure 6.7: Examples of the original unconstrained calibration mapping (left) and the constrained calibration mapping (right). For both mappings we plot $\log(-\kappa_1))$ (blue) and $\log(-\kappa_2)$ (green). The $\log(-\kappa_2)$ surface in the *bm2* mapping has a lower limit of $\log(-\kappa_2) = -2$ imposed on the surface for visualisation.

(top row, left panel) agree with the bootstrap estimates, η_b for most of the fanning voxels and around half of the crossing voxels. However, the calibration give large estimates of anisotropy for the high FA voxels. The calibration estimates of $\bar{\zeta}_1$ show good agreement with ζ_1 (top row, centre panel). The calibration estimates of $\bar{\zeta}_2$ agree with the bootstrap estimates of ζ_2 in most voxels, although the calibration gives low estimates of $\bar{\zeta}_2$ for many of the high FA voxels. The combined mapping for PASMRI (second row) shows similar agreement with the bootstrap.

The QBall 'separate' mapping estimates of $\bar{\eta}_c$ (third row, left) show little agreement to the bootstrap estimates, η_b, although the calibration does capture some anisotropy in the fanning and crossing voxels. Estimates of $\bar{\zeta}_1$ and $\bar{\zeta}_2$ generally agree with the bootstrap estimates, ζ_1 and ζ_2 for all voxels except one grey matter voxel. The 'combined' mapping estimates of $\bar{\eta}_c$ are low compared to the bootstrap estimates, η_b, although there is agreement in the general trend. Calibration estimates of $\bar{\zeta}_1$ and $\bar{\zeta}_2$ generally agree with the bootstrap estimates, ζ_1 and ζ_2.

There is little difference between using 'separate' and 'combined' mappings for PASMRI, although estimates of $\bar{\zeta}_1$ are in closer agreement with ζ_1 for the 'separate' mapping (both PASMRI and QBall). Both the 'separate' and 'combined' PASMRI calibration mappings overestimate the anisotropy in uncertainty for high FA voxels, although the Bingham distribution will be highly concentrated for these voxels, so this

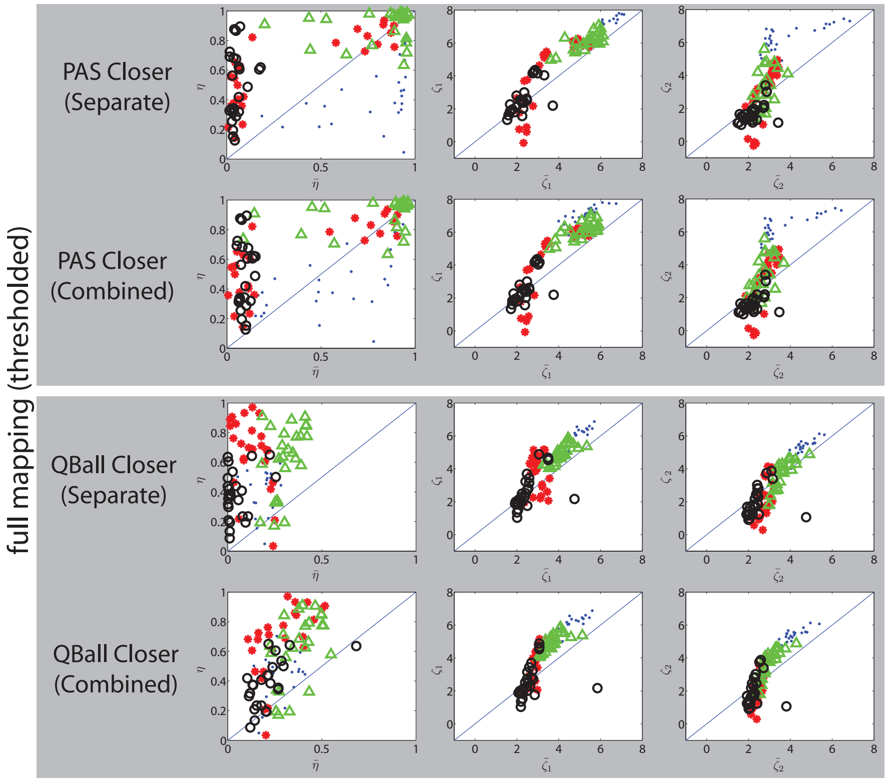

Figure 6.8: Comparison of uncertainty estimates from maximum-likelihood calibration mappings with bootstrap estimates for PASMRI (top two rows) and QBall (bottom two rows). Each plot compares bootstrap estimates of the uncertainty to the mean estimate from the calibration mapping. For each reconstruction algorithm, we plot results from calibrations using ‘separate’ mappings (upper row) and a ‘combined’ mapping (lower row). All mappings use the ‘closer’ dataset and the *bm1* mapping.

anisotropy is unlikely to have a large effect in practice. In contrast, the ‘combined’ mapping estimates of anisotropy in uncertainty for QBall show a better agreement to the bootstrap estimates than those from the ‘separate’ mappings. This may be because the dODFs from QBall models many of the complex fibre configurations with a single peak. Therefore, the extra anisotropy information encoded in the ‘combined’ mapping provides a more accurate relationship between peak shape and uncertainty. In conclusion, both the ‘separate’ and ‘combined’ calibration mappings have similar agreement with the boostrap, although there is a slight advantage in using the ‘separate’ mapping for PASMRI.

6.5.2.4 Conclusions

For PASMRI, using separate *bm1* calibration mappings and the ‘noFP’ dataset appears to generate a calibration mapping that is in closest agreement with the bootstrap. In contrast, the QBall mappings appear to yield similar results, although outlier rejection significantly improves agreement between calibration and bootstrap estimates of the Bingham parameters (see figure 6.5, third and fourth rows). However, the QBall ODFs still underestimate anisotropy in the distribution regardless of the calibration procedure used.

6.5.3 Tractography

In this section, we perform a qualitative comparison of tractography results using the different calibration options. We hypothesise that the PICo maps from the maximum-likelihood calibration will look similar to those presented in the previous chapter, although the calibration procedure here is more robust. In addition to this, we hypothesise that the PICo maps will broadly agree with those from an approximation to bootstrap tractography.

6.5.3.1 Methods

We run multi-fibre PICo tractography on human brain data using maximum-likelihood calibrations for PASMRI and QBall. The PICo connectivity maps obtained using the maximum-likelihood calibration should be similar to those from the previous chapter, although the maximum-likelihood approach is more robust and requires less parameter tuning and user intervention. For each reconstruction algorithm, we compare the results from the maximum-likelihood calibrations to those from a bootstrap approximation (described below), which we can use as a reference. As in chapter 5, we manually define seed regions at the base of the corticospinal/corticopontine tracts.

Bootstrap approximation PICo The bootstrap estimates of fibre orientation and uncertainty from section 6.5.2 provide us with a measure to which we can compare the calibration mapping. Ideally, we would like to be able to use the bootstrap method for probabilistic tractography. This would involve generating bootstrap data for every voxel encountered by the streamlines and then reconstructing to obtain fibre-orientation estimates. However, the method is too computationally heavy when using methods like PASMRI to reconstruct. We therefore propose using an approximation to the bootstrap for evaluation purposes. Instead of generating bootstrap data for a large number of voxels, we generate bootstrap data for a small subset of voxels and reconstruct. The Bingham distribution is then fitted to the fibre-orientation estimates from all bootstraps, which gives an estimate of uncertainty in the voxel. A linear calibration mapping is then fitted between the mean peak shapes and the corresponding uncertainty estimates. Although this method only approximates the full bootstrap, it is able to provide a measure against which we can qualitatively compare the other tractography results.

For each voxel in our bootstrap dataset we have two pieces of information: the Bingham parameter estimates, calculated from the 50 bootstrap samples, and the peak shapes for each bootstrap sample. By fitting a linear mapping between the uncertainty estimates for each peak direction and the mean peak shape we are able to approximate the bootstrap for computationally heavy reconstruction algorithms such as PASMRI. The approximation method assumes that any anisotropy in the uncertainty is aligned with the peak anisotropy of the reconstruction. As with multiple-fibre PICo, we calibrate for one-fibre and multi-fibre voxels separately. Each voxel of the brain data set in the ROI is classified as single-fibre if the mean number of peaks in the bootstrap reconstructions is less than 1.5, otherwise the voxel is classified as a multiple-fibre voxel.

6.5.3.2 Results

Figure 6.9 shows results of multiple-fibre PICo tractography using PASMRI (left) and QBall (right) with the maximum-likelihood calibration procedures. PICo maps using the bootstrap approximation calibration are also provided for comparison (bottom row). In all images, the connectivity maps are overlaid onto FA maps; the colour scheme used for the connectivity maps indicates high connectivity in yellow/orange regions and low connectivity in red/black regions. The PICo map from the bootstrap approximation using PASMRI (bottom left) has a high connectivity index that is even across the tract. The PAS-PICo tractography results using the ‘all’ dataset (top row) have a very low connectivity index when using either the *bm1* calibration (left) and *bm2* calibration (right). Using the ‘closer’ calibration dataset (second row) gives similar results. The PAS-PICo results using the ‘noFP’ calibration have much higher connectivity index when using both the *bm1* and *bm2* mappings. For both mappings (*bm1* and *bm2*), the connectivity indices are evenly spread across the tract. The PICo maps from the ‘noFP’

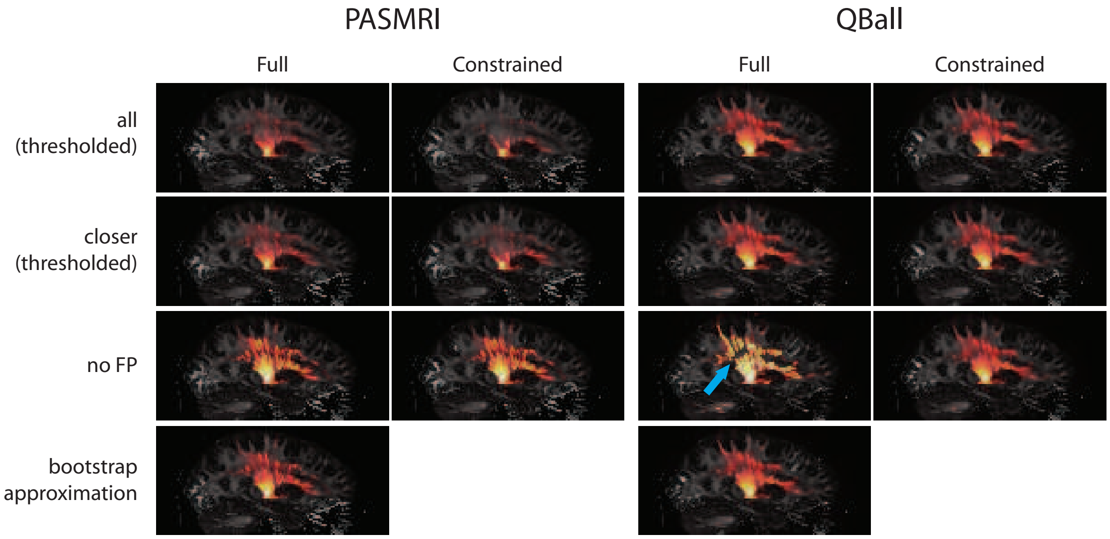

Figure 6.9: PICo tractography results using a PASMRI reconstruction (left) and QBall reconstruction (right) for several calibration variants. Bootstrap-derived PICo maps (bottom row) are included for reference. All calibrations use a separate mapping for one- and multi-fibre voxels. The connectivity maps are overlaid onto FA maps. The colour scheme used for the connectivity maps indicates high connectivity in yellow/orange regions and low connectivity in red/black regions. The blue arrow indicates a crossing-fibre region. Tractography is seeded using the same ROI used in figure 5.9.

dataset are in general agreement with the PICo map from the bootstrap approximation, although the connectivity indices are higher. This doesn't necessarily mean a difference in the quality of results, just that the streamlines are more dispersed in the bootstrap approximation.

The QBall-PICo results are very similar to each other regardless of the variant of the maximum-likelihood calibration procedure used, with the exception of the ‘noFP’ calibration with the ‘full’ mapping. When using the ‘noFP’ dataset with the full mapping, the connectivity indices are very high and the crossing fibre-region is clearly visible as a black hole half way up the tract. All of the other calibrations also have high connectivity indices, but the indices are more evenly spread over the tract and the crossing fibre region is less apparent. The PICo map from the bootstrap approximations using QBall (bottom right) has a very even connectivity index across the tract and is in general agreement with the calibration estimates (apart from the ‘noFP’ *bm1* calibration).

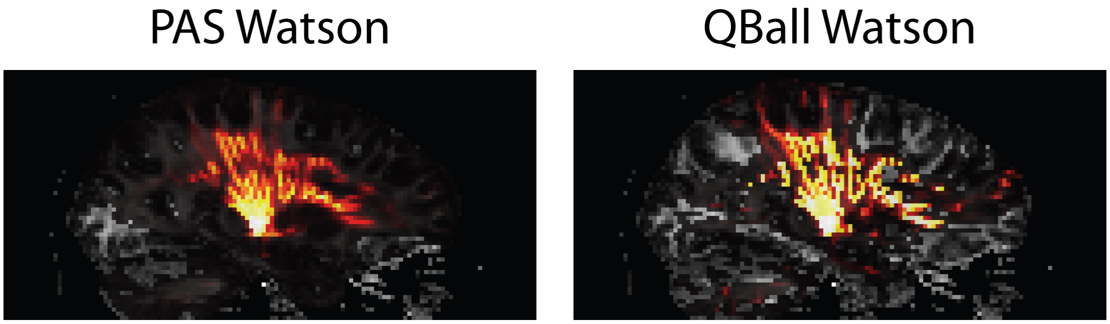

Figure 6.10: Connectivity maps from PAS-PICo (left) and QBall-PICo (right) overlaid onto an FA map. The colour scheme used for the connectivity maps indicates high connectivity in white/yellow regions and low connectivity in orange/red regions. The calibrations use peak sharpness to estimate uncertainty. Tractography is seeded using the same ROI used in figure 5.9.

For comparison, and to demonstrate the *wm1* mapping, figure 6.10 shows PAS-PICo and QBall-PICo maps from maximum-likelihood calibrations that estimate uncertainty from peak sharpness. As in figure 6.9, the connectivity maps are overlaid onto FA maps for visualisation and white/yellow regions on the overlaid connectivity maps indicate high connectivity For PASMRI, the Watson maximum-likelihood calibration provides similar estimates of uncertainty to the estimates from the Bingham calibration. However, the QBall PICo map gives very high connectivity indices. The streamlines have been channelled through several regions to the cortex and the crossing fibre region is clearly visible as a dark hole in the middle of the tract.

6.5.3.3 Conclusions

The PAS-PICo results show that even when outlier rejection is applied, the connectivity index is very low when using the ‘all’ and ’closer’ datasets to calibrate. The low connectivity suggests that the calibration mapping overestimates the uncertainty. The PICo maps using the ‘noFP’ dataset are similar to the PICo map from the bootstrap approximation.

The choice of calibration dataset has less of an impact when using QBall to reconstruct the data. This may be due to the limited range of peak shapes that can be represented by the spherical harmonic implementation of the dODF. In addition to this, SH-QBall is unable to model crossing fibres as accurately as PASMRI and, in many cases, models multiple fibre orientations with a single peak.

6.5.4 Conclusions and Discussion

In this chapter we have introduced a more robust procedure for calibrating multiple-fibre PICo tractography. The maximum-likelihood approach can exploit all of the calibration data to generate the mapping between the peak shape of multiple-fibre reconstructions and the parameters of the distributions that model fibre-orientation uncertainty. Furthermore, the new calibration procedure does not require the user to choose an appropriate bin size. Outlier rejection helps improve the calibration mappings for the complete and reduced datasets, although it does not remove enough of the outliers to provide a useable mapping. Alternative approaches, such as RANSAC [120], may be more efficient at removing outliers from the calibration dataset. We found that using a ‘noFP’ dataset with a constrained mapping gives tractography results that are comparable to those from the bootstrap approximation for both PASMRI and QBall.

We will improve the method in several ways. First, the Watson mapping parameterization *wm1* allows the distribution parameter κ to be both positive and negative (i.e. the mapping allows the full range of Watson distribution configurations). However, the girdle distribution that results when $\kappa < 0$ may not be representative of the uncertainty of fibre-orientation estimates in multiple-fibre methods. A better approach may be to constrain the mapping by taking the log of so that $\kappa \geq 0$. In addition to this, other alternative parameterizations of the calibration mapping may provide a more accurate fit between peak shape and the distribution parameters.

Secondly, we will look at other features of the ODF, such as the peak magnitude. Including additional information about the shape of the ODF may improve the calibration mapping’s ability to deal with spurious peaks.

Finally, it is still unclear how best to exploit these uncertainty estimates in tractography. Combining information about neighbouring voxels and uncertainty estimates when performing the streamline tractography step may improve tractography results.

6.6 Exploiting the True Fibre Distribution

In chapter 3, we highlighted a distinction between the uncertainty of fibre-orientation estimates and the distribution of white-matter orientations in a voxel. In some cases, the uncertainty of the fibre-orientation reflects the underlying distribution of white-matter fibres. However, this is not always the case. For example, for a fanning or bending configuration a reconstruction algorithm may provide a single fibre-orientation estimate orientated towards the mean of the distribution of fibres. In this case, the uncertainty of this fibre-orientation estimate will reflect the noise in the data rather than the actual distribution of fibre orientations. In this section we present some exploratory work where we attempt to predict the distribution of white-matter orientations using the FA and 2D FA orthogonal to λ_1 of the DT and the peak anisotropy of PASMRI. We show that features of the reconstruction algorithms reflect the underlying distribution of fibre orientations. Finally, we show some tractography results when using the true-distribution with DT-PICo and compare the results to those from standard DT-PICo.

6.6.1 Methods

In this section we present a new method for calibration that allows us to map directly between some feature of the reconstruction and the true distribution of fibre orientations. To achieve this we employ a sub-voxel model [17] to generate synthetic data (see figure 6.11). In contrast to the DT model we use in the previous sections, the sub-voxel model explicitly encodes the distribution of fibre-orientations. In the remainder of this section we introduce the synthetic data model and show how to exploit it using a new calibration procedure.

6.6.1.1 Sub-voxel model

The model for the synthetic data is a 3D grid of sub-voxels each containing an instance of Behrens ball and stick model [50] (see chapter 3). This 3D grid of subvoxels allows us to encode information about the spatial distribution of fibre-orientations for complex configurations such as bendings and fannings. In this work we limit the model to represent different fibre dispersions. An illustration of the sub-voxel model, configured to model fibre-dispersion, is shown in figure 6.11. The diagram on the right of this figure depicts a single slice through the centre of the model. The orientation of the anisotropic component for each ball and stick is along the radial line through the centre of the sub-voxel from a point at distance d from the centre of the grid. The parameter d controls the level of fibre divergence in the model. As d increases, the spread of fibre orientations decreases. We can introduce anisotropy into this spread of directions by removing the outer slices of the grid. To simplify the model, we fix the volume fraction and diffusivity so that they are constant over the grid. To obtain diffusion-weighted measurements for the voxel, we calculate the diffusion-weighted measurements for each sub-voxel and then average them together. We then add Rician noise to the measurements at a level comparable to the scanner data.

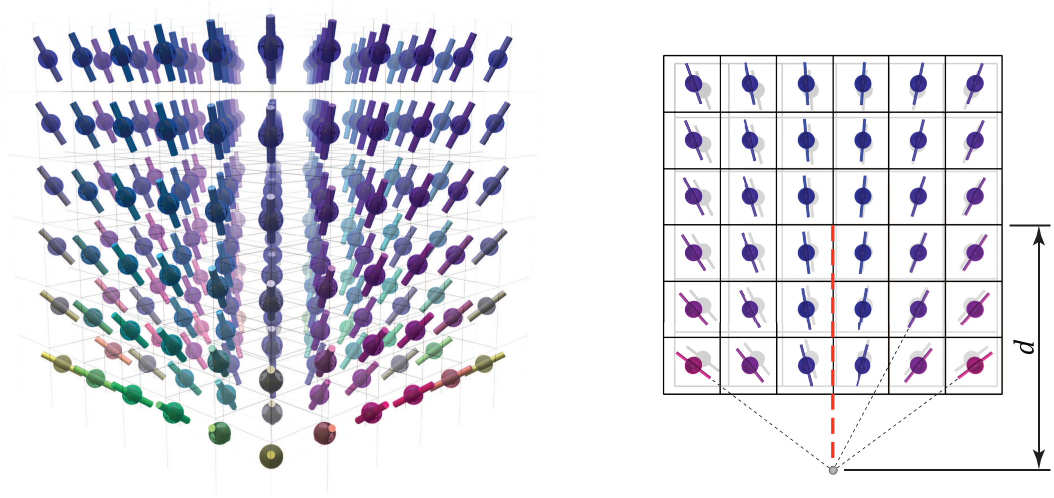

Figure 6.11: An illustration of the sub-voxel model showing a 3D representation (left) and a single slice through the centre of the grid (right). The 3D image on the left shows a sub-voxel model for an isotropic distribution of fibre orientations. Removing the outer slices in either the sagittal or coronal plane introduces anisotropy into the distribution. In the illustration of a single slice, right, the orientations are aligned to the line that passes through the centre of the sub-voxel from point at distance d from the centre of the grid. Increasing d results in a smaller distribution of fibre orientations; decreasing d produces a wider distribution.

6.6.1.2 Calibration procedure

The synthetic data model described above gives us two pieces of information: a set of diffusion-weighted signals from the whole voxel and the true distribution of fibre orientations. As with other versions of PICo, we reconstruct the synthetic data and extract some feature of the reconstruction, such as peak shape. However, we now have direct access to the true fibre distribution. We can model this distribution by collecting the ‘stick’ components from all of the sub-voxels and fitting the Bingham distribution.

Finally, we fit a linear model relating the peak shape (or some other feature) to the Bingham parameters, which we use during tractography to predict the true distribution of fibre orientations from the shape of the diffusion tensor. The complete algorithm is:

- For each set of synthetic data model parameters
    - create grid of sub-voxels.
    - estimate signal from each sub-voxel.
    - average signals from all sub-voxels to approximate signal from entire voxel.
    - add noise to voxel data.
    - reconstruct and calculate peak shapes/directions.
    - collect together stick components from all sub-voxels and fit distribution.
- Fit a linear surface that maps from the peak shape to the corresponding distribution parameters.

6.6.2 Experiments

In this section we test the hypothesis that there is a relationship between the shapes of the peaks of the reconstructions and the underlying distribution of fibre orientations. The fibre distribution provides useful information about the spread of the fibre-orientation estimates that should improve tractography.

We assess our new method using two experiments. First, we show that there is a relationship between shapes of the reconstruction and the true distribution of fibres. We then perform tractography using the new true-distribution DT-PICo and compare the results to the original DT-PICo.

6.6.2.1 Comparing estimates of anisotropy in the fibre distribution to the true anisotropy of the distribution

In this section we hypothesise that the anisotropy of the reconstructed peak(s) will reflect the anisotropy of the true fibre distribution.

We use the sub-voxel synthetic data model to compare the anisotropy of the true distribution of fibre orientations in a voxel of data to the peak shape of its corresponding reconstruction. For the synthetic data, we vary $d \in \{5, 8, 15, 200\}$. We generate data from grids with dimensions $15 \times 15 \times n$, where $n \in \{2, 3, 4, 5, 7, 10, 12, 15\}$ sets the amount of anisotropy in the fibre distribution. To calculate the anisotropy of the true fibre-distribution, we fit the Bingham distribution and calculate the anisotropy of the Bingham parameters, η. We reconstruct the resulting synthetic data using DTI and PASMRI and plot the 2D FA of the DT and peak anisotropy $\nu = FA(\text{diag}(\lambda_1, \lambda_2))$ of the PAS against the anisotropy of the Bingham parameters fitted to the true fibre-distribution (η_{true}).

Figure 6.12 shows anisotropy of the cross-section of the DT against the Bingham parameter FA of the fibre distribution for various settings of d and for various numbers of slices, n. For all settings of d, as the number of slices decreases, the 2DFA of the tensor increases. When $d \in \{5, 8\}$, there is good agreement between the cross-section anisotropy of the DT and the anisotropy of the fibre-distribution. However, as d increases, the peak cross-section of the DT is less anisotropic.

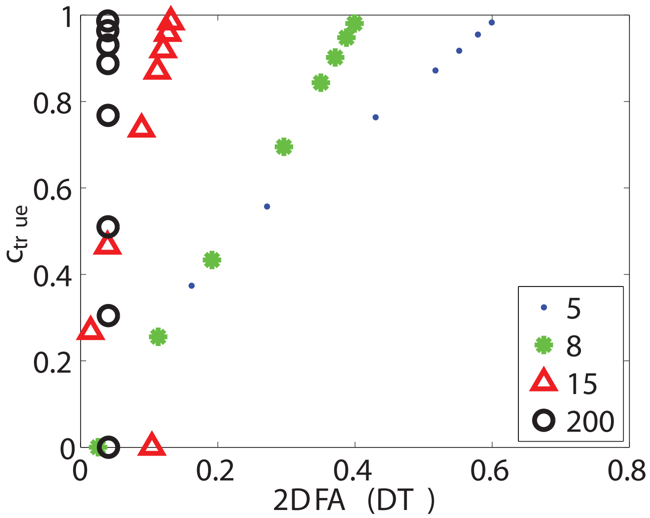

Figure 6.12: Plots the FA of the minor eigenvalues of the DT against the Bingham parameter anisotropy, η_{true}, of the distribution of fibre directions for fanning structures with $d \in \{5, 8, 15, 200\}$. For each setting of d, the number of sagittal slices is set to $n \in \{2, 3, 4, 5, 7, 10, 12, 15\}$.

Figure 6.13 shows a similar mapping for a PASMRI reconstruction. When $d \in \{5, 8\}$ there is a general agreement between the peak anisotropy of the dominant PAS peak and the anisotropy of the fibre distribution. However, when $d \in \{20, 200\}$, the PAS peak is isotropic.

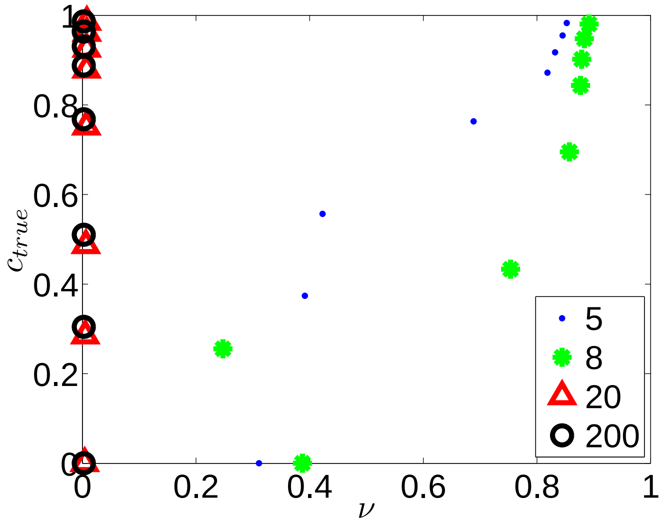

Figure 6.13: Plots the peak anisotropy of a PAS reconstruction, ν, against the Bingham parameter anisotropy, η_{true}, of the distribution of fibre directions for a range of fanning structures with $d \in \{5, 8, 15, 200\}$. For each setting of d, the number of sagittal slices is set to $n \in \{2, 3, 4, 5, 7, 10, 12, 15\}$.

There is general agreement between the 2DFA of the DT and the anisotropy of the fibre distribution at low settings of d. As d becomes large the agreement between the anisotropy in uncertainty and the secondary FA of the tensor decreases. Although there is still some agreement between the 2DFA and η_{true}, as d increases the fibre-distributions become tightly clustered around the mean orientation. This reduces the effect of anisotropy, since the spread of fibre orientations will be very small in relation to voxel size. For PASMRI, there is agreement between the anisotropy of the fibre distribution and peak shape when $d \in \{5, 8\}$ but no agreement outside of this range. Specifically, the dominant peak of the PAS is isotropic when d is outside of the grid.

6.6.2.2 Tractography

In this section we investigate the effect of using estimates of the fibre-orientation distribution in the PICo tractography algorithm. Since PICo is attempting to model the underlying fibre-orientations as opposed to the uncertainty, we would expect a larger range of fibre-orientations in each voxel. This would lead more even connectivity across fanning structures like the descending motor pathways. We compare results from true-distribution PICo to those from the original PICo algorithm.

We fit the DT in each voxel of the brain data, compute FA and secondary FA and use the mapping to predict the Bingham parameters of the fibre-orientation distribution. Tracts seeded at the base of the descending motor pathways are generated for 5000 iterations. The experiment was repeated using Cook et als extension to PICo [36], which estimates the fibre-orientation uncertainty.

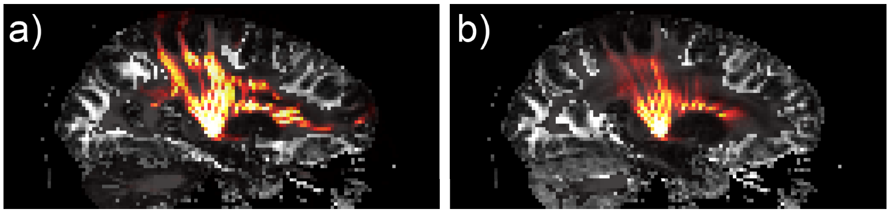

Figure 6.14: PICo connectivity maps from PICo using a) the fibre-orientation uncertainty and b) the fibre-orientation distribution. The connectivity maps are overlaid onto an FA map for visualisation. High connectivity is indicated by yellow/orange regions and low connectivity by red/black regions. Tractography is seeded using the same ROI used in figure 5.9.

Figure 6.14 shows results for standard DT-PICo (left) and true-distribution PICo (right). The original PICo algorithm (left) has very high connectivity indices, but there are dark holes in the tract where tractography has failed at crossing fibre regions. The PICo map from tractography using estimates of the fibre distribution (right) show a very even connectivity index across the tract and the crossing fibre region is far less apparent. However, most of the streamlines fail to reach the cortex.

True distribution PICo shows a much more consistent connectivity index over the entire motor pathway, although the connectivity drops-off rapidly. The connectivity index is far lower when using the fibre distribution. There are two reasons for this. Firstly, the DT fails in crossing fibre regions and will have misleading fibre-orientation estimates. Secondly, connectivity indices will get lower when streamlines go through fanning regions. This is a limitation of probabilistic tractography rather than the calibration.

6.6.3 Conclusions and Discussion

We have introduced a method that extends the PICo tractography algorithm to exploit the true fibre-orientation distribution in each voxel. Our results show that both DTI and

PASMRI are able to predict the true distribution of fibre orientations to some extent. When comparing the PICo map from our technique to the PICo map from the method described by Cook et al in [36], we see that there are structured differences between the maps. PICo tractography performed using knowledge of the fibre-orientation distribution gives significantly different results to those from using uncertainty alone; the connectivity map from our technique has a more even connectivity across the structure, although the connectivity index is a lot lower. The lack of a ground truth prevents us from making any conclusions. However, the concept is worth pursuing. Here we show only a simple application of the idea of using true fibre-orientation distributions in PICo instead of models of uncertainty on individual fibre directions. The diffusion tensor model is too simple to distinguish many kinds of complex fibre configurations. Multiple-fibre algorithms are able to encode the true fibre-distribution to some extent, although the relationship between peak shape and the fibre-distribution breaks down when d is outside the grid. This may be a limitation of the sub-voxel model used to generate the synthetic data. Switching to a simulation-based model, such as [121] may improve the mapping. In future work we will include other complex fibre configurations, such as bendings and crossings, in the calibration dataset and extend the mapping procedure to estimate a distribution of distribution parameters rather than the parameters themselves.

Chapter 7

Discussion and Conclusions

Multiple fibre reconstruction algorithms offer a great deal of useful information about microstructure that is not recovered by the standard DTI approach. However, their transfer to the clinical arena requires careful consideration of their performance and limitations as well as redesign of tractography algorithms to exploit their benefits.

This work makes the following contributions towards resolving the problems described above:

Taxonomy of multiple-fibre algorithms A significant contribution of this work is a classification of multiple-fibre reconstruction algorithms. This classification gives us insight into how the different algorithms are related as well as the likely performance and limitations of the different algorithms.

Comparison Framework The first algorithmic contribution is a standardised framework that aims to quantify the performance and limitations of the multiple-fibre reconstruction algorithms as well as the optimal parameter settings. The main limitation of this framework is that it only considers voxels that contain two fibre populations. The limitation can be resolved by generating one and three fibre configurations in addition to the two fibre configuration currently used. The framework provides a means by which researchers can compare algorithms and decide which methods are most suitable for their analysis.

Comparison of multiple-fibre algorithms We use the standardised framework to perform a rigorous comparison of some of the main multiple-fibre reconstruction algorithms. Optimal parameter settings are given for each multiple-fibre reconstruction algorithm. RBF-SD with a ‘spike’ response function gives the best performance of the linear algorithms, although SH-SD using the same response yields similar results and has far fewer parameters to set. Non-linear methods perform significantly better than the linear methods. CSD gives the best performance of the non-linear algorithms. The findings presented are only valid for the acquisition scheme used here. However, the acquisition scheme was chosen to be similar to those used clinically and the findings will therefore be applicable in a lot of cases.

Peak anisotropy Although multiple-fibre algorithms are increasingly being chosen to reconstruct diffusion-weighted data, the only features from the ODF that are generally exploited are the peak orientations. In this contribution, we investigate what other information is recovered by multiple-fibre reconstruction algorithms. We demonstrate that the peak shapes of multiple-fibre reconstructions contain useful information about the uncertainty of fibre-orientation estimates. Specifically, that peak shapes can be used to model anisotropy in uncertainty, which captures information about the underlying fibre configuration. The information captured by the peak shapes is missed when looking at the peak orientation alone.

multiple-fibre PICo We exploit the information encoded in the peak shape in the PICo tractography algorithm. We show that using the peak shape and sharpness to estimate uncertainty in tractography results in structured differences when compared to using peak sharpness alone. In particular, the connection indices in crossing-fibre regions are higher when using both peak shape and sharpness. A limitation of the calibration-based approach adopted by PICo is that it only approximates the relationship between the peak shape and uncertainty. However, comparisons with bootstrap estimates suggests some agreement between the approaches. An advantage of the calibration-based approach over the other algorithms is that the mapping procedure only has to be performed once and is valid for all data acquired using the same acquisition scheme. As a result PICo is noticably faster than probabilistic tractography using the bootstrap or MCMC approaches. The calibration procedure described is now a standard tool for multiple-fibre PICo tractography in the Camino toolkit.

Robust calibration of multiple-fibre PICo This contribution builds on the multiple-fibre PICo calibration by investigating an alternative, more robust, calibration algorithm. The method provides similar tractography results to the original algorithm but is more robust and requires less user intervention.

Estimating the fibre-distribution Finally, we present some exploratory work that aims to predict the distribution of fibre orientations from features of reconstructions. The ability to extract information about the distributions of fibre-orientations from the ODF can potentially offer significant improvements in the segmentation of white-matter tracts. Early results are promising and estimates of fibre dispersion from our method agree with those from the ground truth to some extent.

We aim to extend the contributions described in this work in several ways. The framework for comparing multiple-fibre algorithms currently uses the peak orientations of the multiple-fibre reconstructions. However, as we have shown, the multiple-fibre reconstruction algorithms not only recover discrete fibre orientations but also potentially provide a wealth of information about the distribution of fibre orientations. In future work we will adapt the framework so that we can compare methods based on this information. For example, we could combine more sophisticated methods for generating synthetic data (such as sub-voxel models of diffusion, physical phantoms, or simulation) with measures of peak anisotropy. This would give us insight into which multiple-fibre reconstruction algorithms recover the most information about the underlying microstructure and inform our choice of reconstruction algorithm when using multiple-fibre PICo.

An interesting question that remains is how the different techniques for estimating uncertainty affect tractography. Determining how well probabilistic tractography performs using a range of uncertainty estimators would be of great benefit when using these methods clinically. We will compare tractography results from our calibration approach to other approaches, such as MCMC and bootstrap.

The exploratory work on estimating the fibre distribution is encouraging but still requires development. For example, the peaks of the dODFs from PASMRI do not appear to capture all of the fibre-distribution information for many configurations of the sub-voxel model. This may not be a limitation of PASMRI but instead a limitation of the synthetic data model used. In future work we will investigate different approaches to generating data, such as the use of simulation of diffusing particles through a 3D mesh. We will also further develop the calibration procedure for predicting the distribution of fibre orientations by the method to include additional fibre configurations, such as bending and crossing fibres. Exploiting the distribution of fibre orientations in tractography will also require development of the tractography algorithm. In particular, the process of deciding how to choose the next fibre-orientation estimate will need to be refined to use the additional information in a more meaningful way. One approach would be to use information in the local neighbourhood when choosing which direction to follow at each step.

Diffusion MRI is a very active field of research. There remain many unanswered questions about distribution of fibre orientations within a voxel and how best to resolve the ambiguities in the reconstruction of complex microstructural configurations. The work presented in this thesis has attempted to address many of thesis shortcomings but several avenues exist for further work. For example, incorporating more detailed microstructural information, such as axon-diameter estimates, and models into fibre-tract reconstruction may help to address problems such as kissing vs crossing fibres. In conclusion, there is great potential for these methods both pre-clinically and clinically.

Appendix A

Spherical Harmonic Implementation

The spherical harmonic of order $l = 0, 1, 2, ...$ and index $m = -l, ..., 0, ..., l$ is

$$Y_{lm}(\theta, \phi) = \left(\frac{(2l+1)}{4\pi} \frac{(l-m)!}{(l+m)!} \right)^{\frac{1}{2}} P_{lm}(\cos(\theta) \exp(im\phi), \tag{A.1}$$

where θ is the angle of colatitude, i.e. the angle with the z-axis, ϕ is the angle of longitude and $P_{l,m}$ is the associated Legendre polynomial with order m and index l (we omit the definition of P here, but most mathematical programming languages, such as Mathematica or Matlab, have built in functions to compute the associated Legendre polynomials). The functions are waves on the sphere with frequency that increases with harmonic order l.

The spherical harmonics are the restriction to the sphere of a normalized set of solutions of Laplace's equation in three dimensions. Each harmonic is a function of the sphere and together they constitute an orthonormal basis for spherical functions. With the definition in equation A.1

$$\int_0^{\pi} \int_0^{2\pi} Y_{lm} Y_{l'm'} d\theta d\phi = \delta_{ll'} \delta_{mm'}, \tag{A.2}$$

where δ_{ab} is the Kronecker delta, which is one if $a = b$ and zero otherwise. We can write any complex-valued function f of the sphere as a sum of spherical harmonic functions:

$$f(\theta, \phi) = \sum_{l=0}^{\infty} \sum_{m=-l}^{l} c_{lm} Y_{lm} \tag{A.3}$$

where c_{lm} is a complex number. Truncations of the series at finite order give low frequency approximations of f in a similar way to truncations of the Fourier series for rectilinear functions.

For real-valued functions, $c^*_{lm} = (-1)^m c_{l-m}$, where * indicates the complex conjugate, so the number of scalar parameters that need to be estimated for spherical harmonic orders up to l is $(l+1)^2$ rather than $2(l+1)^2$ for complex-values functions. Spherical functions in diffusion MRI, such as the fODF and dODF, are often both real-valued and antipodally symmetric, i.e. $f(\hat{\mathbf{x}}) = -f(\hat{\mathbf{x}})$. Functions with antipodal symmetry require only even-order spherical harmonics, i.e. $c_{lm} = 0$ for odd l, so the total number of scalars for an order-l approximation reduces still further to $\frac{1}{2}(l+1)(l-1)$. With these observations it is simple to construct a linear mapping to obtain the best fit spherical harmonic coefficients for a real-valued antipodally symmetric function from samples of that function, for example, to fit a real-valued antipodally symmetric spherical harmonic series to diffusion MRI measurements from a spherical acquisition scheme [55]. A similar representation underlies spherical harmonic QBall [70, 71, 72] and spherical deconvolution [77]. Descoteaux [122] gives a nice overview of spherical harmonics within the context of diffusion MRI.

Appendix B

QBall Implementation

First, the measurements $A(\mathbf{q})$ must be interpolated in order to obtain the equator points. The interpolation is implemented as a sum of linear basis functions $\psi(\mathbf{q})$,

$$A(\mathbf{q}) = \sum_{j=1}^{J} \xi_j \psi_j(q) \tag{B.1}$$

where ξ_j is a basis function weight. In matrix form this becomes

$$\mathbf{A} = \mathbf{Y\Xi} \tag{B.2}$$

where $\mathbf{A} = (A(\mathbf{q}_1), ..., A(\mathbf{q}_N))^T$, $\mathbf{\Xi} = (\xi_1, ..., \xi_J)^T$ and $\mathbf{Y}_{ij} = \psi_j(\mathbf{q}_i)$. The dODF can then be calculated at a set of points over a sphere. The dODF is represented using a second sum of linear basis functions, i.e.

$$\phi(\hat{\mathbf{x}}) = \sum_{k=1}^{K} \beta_k \theta_k(\hat{\mathbf{x}}) \tag{B.3}$$

Substituting the basis function implementations back in Eqns B.1 and B.3 in Eqn 3.5 gives

$$\mathbf{\Theta C} = \mathbf{\Psi\Xi} = \mathbf{\Psi Y' A} \tag{B.4}$$

where $\mathbf{\Theta}_{lk} = \theta_k(\hat{\mathbf{x}}_l)$, $\mathbf{\Psi}_{kj} = \int_{\mathcal{C}(\hat{\mathbf{x}}_k)} \psi_j(\mathbf{q}) \mathrm{d}\hat{\mathbf{q}}$ and $\mathbf{C} = (\beta_1, ..., \beta_K)^T$. The matrix $\mathbf{\Theta' \Psi Y'}$ is not dependent on the measurements $(A(\mathbf{q}_1), ..., A(\mathbf{q}_N))$ and therefore only has to be computed once.

A range of basis functions can be used in the implementation of this method. Tuch uses the radial basis function

$$\theta_k(\hat{\mathbf{x}}) = \exp(-\cos^{-1}(|\hat{\mathbf{x}} \cdot \hat{\mathbf{y}}_k|)/\sigma^2) \tag{B.5}$$

where σ is a scaling parameter and the $\hat{\mathbf{y}}_k, k = 1, ..., K$, are unit vectors evenly distributed on the sphere. Others [70, 71, 72] use spherical harmonics.

Appendix C

Spherical Deconvolution Implementation

If we represent the FOD using a linear basis so that

$$f(\hat{\mathbf{x}}) = \sum_{i=1}^{K} \beta_i \theta_i(\hat{\mathbf{x}}) \tag{C.1}$$

and substitute into Eqn.(3.7), we see that

$$A(\mathbf{q}_i) = \sum_{i=1}^{K} \beta_k \int \theta_k(\hat{\mathbf{x}}) R(\mathbf{q}_i; \hat{\mathbf{x}}) \mathrm{d}\hat{\mathbf{x}} \tag{C.2}$$

Deconvolution is then linear since $\mathbf{B} = \mathbf{X}'\mathbf{A}$, where $\mathbf{A} = (A(\mathbf{q}_1), ..., A(\mathbf{q}_N))^T$ is the set of diffusion weighted measurements in a voxel, $\mathbf{B} = (\beta_1, ..., \beta_K)^T$ is the weights of the basis functions that define the FOD and $\mathbf{X}'$ is the pseudo inverse of the matrix $\mathbf{X}$ with elements $\mathbf{X}_{ik} = \int \theta_k(\hat{\mathbf{x}}) R(\mathbf{q}_i; \hat{\mathbf{x}}) d\hat{\mathbf{x}}$. Since the $\mathbf{q}_i$, $i = 1, ..., N$ are the same for each voxel, we need to compute $\mathbf{X}$ and $\mathbf{X}'$ only once.

Appendix D

Constrained Spherical Deconvolution Implementation

Constrained spherical deconvolution [78] is an iterative procedure that uses Tikhinov regularisation [79] to reduce or eliminate neagtive lobes in the fODF. Tikhinov regularisation minimises the function

$$||\mathbf{XB} - A||^2 + \lambda^2||\mathbf{L}(\mathbf{B} - \mathbf{B}_0)||^2 \tag{D.1}$$

where $\mathbf{L}$ is the constraint matrix and $\mathbf{B}_0$ is the initial estimate of the coefficients. To calculate $\mathbf{L}$, the fODF is first evaluated in a number of directions

$$u = \mathbf{PB}_i, \tag{D.2}$$

where $\mathbf{P}$ maps the basis function coefficients to amplitudes in a discrete set of directions. The elements of the constraint matrix, $\mathbf{L}$, are then

$$\mathbf{L}_{m,n} \begin{cases} \mathbf{P}_{m,n} & \text{if } u_m > \tau, \\ 0 & \text{if } u_m \leq \tau, \end{cases} \tag{D.3}$$

where τ is a threshold defined as a fraction of the mean fODF magnitude. Thus, the fODF is constrained to zero in directions where $u_m \leq \tau$. The estimates of the coefficients at the next iteration are

$$\mathbf{B}_{i+1} = \text{arg min}\{||\mathbf{XB}_i - A||^2 + \lambda^2||\mathbf{LB}_i||^2\}. \tag{D.4}$$

After each iteration, $\mathbf{L}$ is re-calculated. The algorithm terminates when there is no further change in $\mathbf{L}$.

Appendix E

Threshold Plots

This appendix shows the effect of varying the threshold parameters g and h on $\bar{c}$ for all reconstruction algorithms used in Experiment 1. For each tile, the point at which $\bar{c}$ is maximised is highlighted with a red marker.

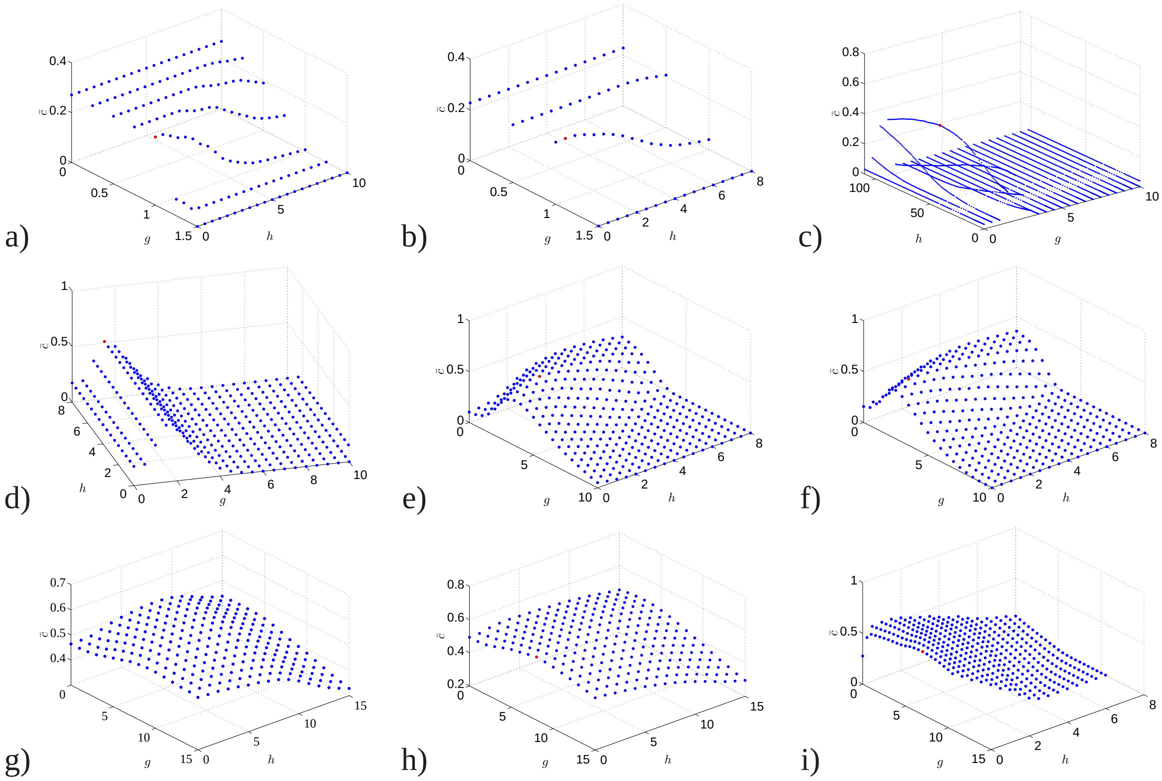

Figure E.1: Effect of changing threshold settings on $\bar{c}$ for a) SH-QBall, b) RBF-QBall, c) RBF-PASMRI, d) RBF-SD, SH-SD using e) the ‘DT’ response and f) ‘spike’ reponse (right), g) MESD, h) PASMRI and i) CSD.

Appendix F

Details of Reconstruction Algorithm Performance at Optimal Settings

Here, we show the numerical data used to generate the tile maps in Experiment 1. Measures that have been estimated from a very small number of samples are in grey.

F.1 Results for SH-QBall

		$\lambda_1 = 1.9 \times 10^{-9}$ m^2 s^{-1}			$\lambda_1 = 1.5 \times 10^{-9}$ m^2 s^{-1}			$\lambda_1 = 1.1 \times 10^{-9}$ m^2 s^{-1}		
a	θ (deg)	c	$\gamma(\kappa_1)$	α (deg)	c	$\gamma(\kappa_1)$	α (deg)	c	$\gamma(\kappa_1)$	α (deg)
0.5	0°	1	5.4	0.16	0.92	3.7	0.47	0.24	1.9	1.3
	10°	1	5.4	2.8	0.84	3.9	4.6	0.21	1.7	10
	20°	0.83	5.5	5.3	0.31	4.3	5.8	0.15	1	22
	30°	0	-0	90	0	0	59	0.063	0.98	61
	40°	0	-0	90	0	-0	90	0.0069	1.6	66
0.6	0°	1	4.7	0.19	0.82	3.1	0.69	0.23	1.8	2
	10°	0.95	4.7	4.8	0.6	3.3	4.5	0.26	1.6	4.8
	20°	0.34	5.2	7.3	0.13	3.1	4.2	0.1	1.4	14
	30°	0	-0	90	0	-0	90	0.035	1.2	42
	40°	0	-0	90	0	-0	90	0.0069	1.8	56
0.7	0°	0.85	3.9	0.75	0.49	3.1	0.23	0.2	1.8	1.8
	10°	0.36	4.5	3.8	0.15	3.2	3	0.15	1.7	8
	20°	0.014	5.5	4.6	0.014	4.6	7.4	0.042	1.5	20
	30°	0	-0	90	0	-0	90	0.014	1.8	42
	40°	0	-0	90	0	-0	90	0	1.6	59

F.2 Results for RBF-QBall

		$\lambda_1 = 1.9 \times 10^{-9}$ m^2 s^{-1}			$\lambda_1 = 1.5 \times 10^{-9}$ m^2 s^{-1}			$\lambda_1 = 1.1 \times 10^{-9}$ m^2 s^{-1}		
a	θ (deg)	c	$\gamma(\kappa_1)$	α (deg)	c	$\gamma(\kappa_1)$	α (deg)	c	$\gamma(\kappa_1)$	α (deg)
0.5	0°	0.92	3.4	1.1	0.59	2.8	2.6	0.14	1.7	8.9
	10°	0.79	3.3	4.1	0.48	2.7	6	0.15	1.6	12
	20°	0.51	3.5	3.7	0.24	2.2	4.6	0.097	1.1	20
	30°	0.13	3.6	2.1	0.09	2	5.2	0.069	0.85	61
	40°	0	-0	90	0.021	0.76	35	0.042	0.88	63
0.6	0°	0.85	3.1	1.3	0.59	2.5	1	0.13	1.7	3.4
	10°	0.78	3.2	3.5	0.48	2.4	5.1	0.17	1.7	7.7
	20°	0.32	3.1	3.1	0.23	1.9	7.4	0.14	1.3	14
	30°	0.056	3.6	2.1	0.069	1.8	14	0.076	1	35
	40°	0	-0	90	0.014	2	24	0.035	0.93	42
0.7	0°	0.72	2.9	1.5	0.5	2.3	1.5	0.15	1.4	2.6
	10°	0.52	2.8	1.6	0.35	2.2	2.7	0.13	1.4	8.4
	20°	0.15	3.1	4.2	0.13	2.2	10	0.1	1.4	11
	30°	0.021	3.1	7.4	0.035	2.4	17	0.042	1	37
	40°	0	-0	90	0	2.5	41	0.028	0.96	42

F.3 Results for RBF-PASMRI

		$\lambda_1 = 1.9 \times 10^{-9}$ m^2 s^{-1}			$\lambda_1 = 1.5 \times 10^{-9}$ m^2 s^{-1}			$\lambda_1 = 1.1 \times 10^{-9}$ m^2 s^{-1}		
a	θ (deg)	c	$\gamma(\kappa_1)$	α (deg)	c	$\gamma(\kappa_1)$	α (deg)	c	$\gamma(\kappa_1)$	α (deg)
0.5	0°	0.99	4.8	0.16	0.91	3.7	0.36	0.17	1.6	2.8
	10°	0.99	5	4	0.9	3.5	3.5	0.16	1.4	7.1
	20°	0.95	4.8	6.5	0.79	3.3	6.2	0.1	1.3	12
	30°	0.88	4.4	7.4	0.51	2.9	7.6	0.049	1.1	19
	40°	0.15	0.87	8	0.15	1.4	8.1	0.035	0.73	36
0.6	0°	0.99	4.7	0.14	0.89	3.4	0.39	0.18	1.3	3
	10°	0.99	4.7	4.9	0.85	3.4	4.3	0.17	1.4	5.2
	20°	0.94	4.5	9	0.7	3.3	8.2	0.13	1.3	12
	30°	0.67	3.7	13	0.37	2.3	12	0.042	1.2	18
	40°	0.063	0.84	79	0.11	1	14	0.035	0.65	47
0.7	0°	0.97	4.3	0.3	0.7	2.9	0.66	0.18	1.2	2.9
	10°	0.97	4.2	5.6	0.65	2.9	5.2	0.15	1.3	3.8
	20°	0.75	4.2	12	0.43	2.5	10	0.1	1.2	13
	30°	0.15	2.2	18	0.15	1.6	15	0.042	1	21
	40°	0.0069	1.9	88	0.028	0.76	28	0.007	0.79	34

F.4 Results for RBF-SD

		$\lambda_1 = 1.9 \times 10^{-9}$ m^2 s^{-1}			$\lambda_1 = 1.5 \times 10^{-9}$ m^2 s^{-1}			$\lambda_1 = 1.1 \times 10^{-9}$ m^2 s^{-1}		
a	θ (deg)	c	$\gamma(\kappa_1)$	α (deg)	c	$\gamma(\kappa_1)$	α (deg)	c	$\gamma(\kappa_1)$	α (deg)
0.5	0°	1	4.9	0.1	0.99	4	0.4	0.37	1.9	1
	10°	1	5.1	2.8	0.98	4	1.9	0.35	1.9	1.6
	20°	1	5	4.3	0.9	4	3	0.31	1.8	3.5
	30°	0.83	4.7	2.7	0.49	3.5	3.2	0.17	1.4	12
	40°	0	-0	90	0.021	1.4	6	0.063	0.66	53
0.6	0°	1	4.8	0.1	0.97	3.7	0.24	0.35	1.8	1.9
	10°	1	4.8	3.7	0.94	3.6	2.8	0.33	1.8	3.2
	20°	1	4.7	6.1	0.83	3.5	4.9	0.29	1.6	7.3
	30°	0.64	4.5	6	0.4	2.9	6.3	0.19	1.5	12
	40°	0	0	82	0.014	1.6	28	0.049	0.91	25
0.7	0°	1	4.4	0.13	0.89	3.3	0.16	0.28	1.5	2.1
	10°	1	4.4	4.5	0.84	3.1	4	0.25	1.5	2.4
	20°	0.97	4.2	8.6	0.65	3	8.2	0.2	1.4	7.5
	30°	0.43	3.7	14	0.2	2.3	13	0.13	1.2	13
	40°	0	1.4	32	0	1.5	29	0.035	0.97	22

F.5 Results for SH-SD (DT response)

		$\lambda_1 = 1.9 \times 10^{-9}$ m^2 s^{-1}			$\lambda_1 = 1.5 \times 10^{-9}$ m^2 s^{-1}			$\lambda_1 = 1.1 \times 10^{-9}$ m^2 s^{-1}		
a	θ (deg)	c	$\gamma(\kappa_1)$	α (deg)	c	$\gamma(\kappa_1)$	α (deg)	c	$\gamma(\kappa_1)$	α (deg)
0.5	0°	1	5.3	0.19	0.95	3.9	0.41	0.24	1.7	2.1
	10°	1	5.3	3	0.92	3.8	2.5	0.26	1.8	4.7
	20°	0.99	5.1	5.2	0.85	3.6	4.3	0.21	1.6	8.4
	30°	0.86	4.8	4.8	0.61	2.9	5.5	0.15	1.5	9.5
	40°	0.021	0.89	23	0.097	1.4	10	0.042	0.86	28
0.6	0°	1	4.9	0.16	0.9	3.5	0.31	0.24	1.6	3.2
	10°	1	4.8	4	0.88	3.3	3.4	0.24	1.6	6
	20°	0.99	4.6	7.5	0.73	3.2	6.6	0.19	1.5	8.7
	30°	0.77	4.1	9.4	0.48	2.4	9	0.13	1.3	13
	40°	0.021	1.2	17	0.049	0.99	20	0.028	0.98	20
0.7	0°	0.99	4.3	0.12	0.74	3	0.86	0.2	1.3	3.8
	10°	0.95	4	5.3	0.72	3	4.7	0.21	1.2	6.3
	20°	0.78	3.8	10	0.51	2.7	9.2	0.15	1.2	11
	30°	0.31	3.2	15	0.19	2.1	14	0.12	1.1	14
	40°	0.0069	1.2	23	0.021	1.1	37	0.035	0.93	22

F.6 Results for SH-SD (‘spike’ response)

		$\lambda_1 = 1.9 \times 10^{-9}$ m^2 s^{-1}			$\lambda_1 = 1.5 \times 10^{-9}$ m^2 s^{-1}			$\lambda_1 = 1.1 \times 10^{-9}$ m^2 s^{-1}		
a	θ (deg)	c	$\gamma(\kappa_1)$	α (deg)	c	$\gamma(\kappa_1)$	α (deg)	c	$\gamma(\kappa_1)$	α (deg)
0.5	0°	1	5.4	0.16	0.98	4.1	0.35	0.27	1.8	2.2
	10°	1	5.3	2.6	0.95	3.9	1.8	0.28	1.9	3.6
	20°	0.99	5.1	4.1	0.84	3.8	3.3	0.25	1.7	2.8
	30°	0.78	4.9	2.9	0.53	3.6	3.1	0.17	0.75	26
	40°	0.014	1.2	16	0.028	1.1	11	0.063	1.1	17
0.6	0°	1	4.9	0.14	0.92	3.5	0.49	0.26	1.8	3
	10°	1	4.8	3.5	0.9	3.4	2.8	0.26	1.7	5.7
	20°	0.99	4.6	6.1	0.78	3.3	5.2	0.24	1.5	6.8
	30°	0.63	3.7	7.2	0.34	2.6	7.7	0.14	1.3	10
	40°	0	1	50	0.028	1.4	19	0.049	1.1	17
0.7	0°	1	4.3	0.14	0.75	3.1	0.76	0.18	1.4	2.4
	10°	0.99	4.1	4.7	0.71	3	3.7	0.19	1.4	4.5
	20°	0.88	3.8	9	0.52	2.9	8.1	0.15	1.2	9.3
	30°	0.4	3.1	13	0.21	2.3	12	0.083	1.2	13
	40°	0	1.1	37	0.0069	0.98	29	0.035	0.86	20

F.7 Results for CSD

		$\lambda_1 = 1.9 \times 10^{-9}$ m^2 s^{-1}			$\lambda_1 = 1.5 \times 10^{-9}$ m^2 s^{-1}			$\lambda_1 = 1.1 \times 10^{-9}$ m^2 s^{-1}		
a	θ (deg)	c	$\gamma(\kappa_1)$	α (deg)	c	$\gamma(\kappa_1)$	α (deg)	c	$\gamma(\kappa_1)$	α (deg)
0.5	0°	1	6.1	0.16	1	4.9	0.26	0.3	2	3.1
	10°	1	5.9	0.41	0.99	4.7	0.51	0.28	2	3
	20°	1	5.9	2.1	0.99	4.5	1.5	0.29	1.8	4.8
	30°	0.82	5.8	2.1	0.87	4.3	1.3	0.29	1.8	7.1
	40°	0	-0	90	0.11	3.2	3.5	0.2	0.95	14
0.6	0°	1	5.7	0.15	0.99	4.4	0.3	0.31	1.9	2.3
	10°	1	5.4	1.4	0.98	4.2	0.96	0.27	1.9	3.6
	20°	1	5.3	2.4	0.96	4	1.5	0.28	1.8	3.7
	30°	0.91	5.3	3.8	0.88	3.9	2.5	0.27	1.6	8.7
	40°	0.014	5.2	14	0.18	3.6	11	0.21	1.4	13
0.7	0°	1	5.3	0.15	0.96	4	0.18	0.26	1.5	1.4
	10°	0.99	4.9	3.2	0.9	3.6	1.9	0.21	1.5	0.87
	20°	0.96	4.5	2.6	0.82	3.5	1.5	0.21	1.6	4.5
	30°	0.87	4.8	4.2	0.74	3.8	2.1	0.24	1.5	5.9
	40°	0.085	4.6	11	0.19	3.7	11	0.19	1.3	9.1

F.8 Results for PASMRI

		$\lambda_1 = 1.9 \times 10^{-9}$ m^2 s^{-1}			$\lambda_1 = 1.5 \times 10^{-9}$ m^2 s^{-1}			$\lambda_1 = 1.1 \times 10^{-9}$ m^2 s^{-1}		
a	θ (deg)	c	$\gamma(\kappa_1)$	α (deg)	c	$\gamma(\kappa_1)$	α (deg)	c	$\gamma(\kappa_1)$	α (deg)
0.5	0°	1	6.2	0.17	1	5	0.36	0.35	2.2	1.5
	10°	1	6.1	1.1	1	5	0.7	0.31	2	4
	20°	0.98	5.9	2.3	0.99	4.5	1.6	0.27	2	4.8
	30°	0.49	5.2	3	0.83	3.4	2.8	0.18	1.8	8
	40°	0	1.6	62	0.34	1.9	9.6	0.1	1.2	25
0.6	0°	0.98	5.8	0.13	0.99	4.6	0.37	0.33	2.1	1.8
	10°	0.97	5.8	1.7	1	4.6	1.6	0.31	2	3.9
	20°	0.97	5.6	3.8	0.97	4.1	4.2	0.25	1.9	8
	30°	0.78	5	6.8	0.79	3.4	7.9	0.18	1.5	16
	40°	0.056	3.7	24	0.29	2.3	17	0.09	1.4	19
0.7	0°	0.97	5.4	0.15	0.97	4.2	0.48	0.27	1.9	2.1
	10°	0.97	5.4	2	0.97	4.1	3.1	0.24	1.9	3.3
	20°	0.99	5.1	4.4	0.89	3.9	6.8	0.22	1.7	9
	30°	0.87	4.6	9.9	0.59	3.3	13	0.16	1.5	17
	40°	0.049	4	25	0.083	2.7	28	0.083	1.4	18

F.9 Results for MESD

		$\lambda_1 = 1.9 \times 10^{-9}$ m^2 s^{-1}			$\lambda_1 = 1.5 \times 10^{-9}$ m^2 s^{-1}			$\lambda_1 = 1.1 \times 10^{-9}$ m^2 s^{-1}		
a	θ (deg)	c	$\gamma(\kappa_1)$	α (deg)	c	$\gamma(\kappa_1)$	α (deg)	c	$\gamma(\kappa_1)$	α (deg)
0.5	0°	1	6.3	0.12	0.92	4	0.54	0.09	1.8	2.3
	10°	1	6.3	0.84	0.92	3.9	0.67	0.11	1.8	4.6
	20°	1	6.1	1.8	0.9	3.9	0.93	0.076	1.8	5.8
	30°	0.7	6.1	2.3	0.83	3.1	2.1	0.035	1.8	8
	40°	0	-0	90	0.54	2.4	7.3	0.042	1.2	20
0.6	0°	1	5.9	0.1	0.93	3.7	0.14	0.11	1.9	2.6
	10°	1	5.9	0.94	0.91	3.6	0.69	0.13	1.9	5.9
	20°	1	5.7	2.1	0.89	3.7	1.7	0.1	1.8	6.4
	30°	0.72	5.7	3.3	0.83	3.3	3.7	0.1	1.6	12
	40°	0	-0	90	0.49	2.4	9.5	0.063	1.3	22
0.7	0°	1	5.3	0.14	0.85	3.4	0.63	0.097	1.6	3.6
	10°	0.96	5.3	1	0.81	3.2	0.51	0.076	1.7	6.1
	20°	0.99	5.1	2.2	0.81	3.3	1.7	0.09	1.6	6.7
	30°	0.74	5.2	3.7	0.74	3	4.4	0.09	1.5	14
	40°	0.021	5.4	12	0.32	2.3	12	0.056	1.3	22

Bibliography

[1] M. E. Moseley, J. Kucharczyk, J. Mintorovitch, Y. Cohen, J. Kurhanewicz, N. Derugin, H. Asgari, and D. Norman. Diffusion-weighted MR imaging of acute stroke: correlation with T2-weighted and magnetic susceptibility-enhanced MR imaging in cats. *AJNR American Journal of Neuroradiology*, 11:423–429, 1990.

[2] S. Warach, D. Chien, W. Li, M. Ronthal, and R. Edelman. Fast magnetic resonance diffusion-weighted imaging of acute human stroke. *Neurology*, 42:1717–1723, 1992.

[3] P. J. Basser, J. Matiello, and D. Le Bihan. MR diffusion spectroscopy and imaging. *Biophysical Journal*, 66:259–267, 1994.

[4] T Klingberg, M. Hedehus, E. Temple, T. Salz, J. D. E. Gabriele, M. E. Moseley, and R. A. Poldrack. Microstructure of temporo-parietal white matter as a basis for reading ability. *Neuron*, 25:493–500, 2000.

[5] G. Douaud, T. E. Behrens, C. Poupon, Y. Cointepas, S. Jbabdi, V. Gaura, N. Golestani, P. Krystkowiak, C. Verny, P. Damier, A. C. Bachous-Lévi, P. Hantraye, and P. Remy. In vivo evidence for the selective subcorical degeneration in huntington's disease. *NeuroImage*, 46:958–966, 2009.

[6] B. Draganski, F. Kherif, S. Klöppel, P. A. Cook, D. C. Alexander, G. J. M Parker, R. Deichmann, and R. J. S. Ashburner, J. annd Frackowiak. Evidence for segregated and integrative connectivity patterns in the human basal ganglia. *Journal of Neuroscience*, 28:7143–7152, 2008.

[7] C. A. Clark, T. R. Barrick, M. M. Murphy, and B. A. Bell. White matter fiber

tracking in patients with space-occupying lesions of the brain: a new technique for neurosurgical planning? *NeuroImage*, 20:1601–1608, 2003.

[8] M. Lazar, P. J. Thottakara, A. S. Field, B. Laundre, B. Badie, B. Jellison, and A. L. Alexander. A white matter tractography study of white matter reorganization after surgical resection of brain neoplasms. In *Proc. 12th Annual Meeting of the ISMRM*, page 1259, Kyoto, 2004.

[9] T. E. J. Behrens, H. Johansen Berg, S. Jbabdi, M. F. S. Rushworth, and M. W. Woolrich. Probabilistic diffusion tractography with multiple fibre orientations: What can we gain? *NeuroImage*, 34:144–155, 2007.

[10] G. J. M. Parker and D. C. Alexander. Probabilistic anatomic connectivity derived from the microscopic persistent angular structure of cerebral tissue. *Philosophical Transactions of the Royal Society B*, 360:893–902, 2005.

[11] S. Wiebe, W. T. Blume, J. P. Girvin, and M. Eliasziw. A randomized controlled trial of surgery for temporal-lobe epilepsy. *New England Journal of Medicine*, 345:311–318, 2001.

[12] R. Marino Jr. and T. Rasmussen. Visual field changes after temporal lobectomy in man. *Neurology*, 18:825–835, 1968.

[13] T. Yamamoto, K. Yamada, T. Nishimura, and S. Kinoshita. Tractography to depict three layers of visual field trajectories to the calcarine gyri. *American Journal of Ophthalmology*, 140:781–785, 2005.

[14] D. Nilsson, G. Stark, M. Ljungberg, S. Ribbelin, L. Jösson, K. Malmgren, and B. Rydenhag. Intersubject variability in the anterior extent of the optic radiation assessed by tractography. *Epilepsy Research*, 77:11.16, 2007.

[15] K. M. Jansons and D. C. Alexander. Persistent angular structure: new insights from diffusion MRI data. *Inverse Problems*, 19:1031–1046, 2003.

[16] D. C. Alexander. Maximum entropy spherical deconvolution for diffusion MRI. In *Proc. Information Processing in Medical Imaging*, pages 76–87, 2005.

[17] S. Nedjati-Gilani, G. J. Parker, and D. C. Alexander. Sub-voxel reconstruction of fibre orientations in diffusion mri. In *Medical Image Understanding and Analysis*, Aberystwyth, 2007.

[18] K. K. Seunarine and D. C. Alexander. Multiple fibers: beyond the diffusion tensor. In H. Johansen-Berg and T. E. J. Behrens, editors, *Diffusion MRI: from quantitative measurement to in vivo neuroanatomy*, pages 55–72. Academic Press, 2009.

[19] K. K. Seunarine and D. C. Alexander. Linear persistent angular structure MRI and non-linear spherical deconvolution for diffusion MRI. In *Proc. 14th Annual Meeting of the ISMRM*, page 2726, Seattle, 2006.

[20] K. K. Seunarine, P. A. Cook, M. G. Hall, K. V. Embleton, G. J. M. Parker, , and D. C. Alexander. Exploiting peak anisotropy for tracking through complex structures. In *Proc. 11th IEEE International Conference on Computer Vision Workshop on MMBIA*, Rio de Janeiro, 2007.

[21] K. K. Seunarine, P. A. Nedjati-Gilani, S. Cook, M. G. Hall, and D. C. Alexander. Exploiting the true fibre distribution for probabilistic tractography. In *Proc. 16th Annual Meeting of the ISMRM*, page 1831, Toronto, 2008.

[22] A. D. Elster and J. H. Burdette. *Questions and Answers in Magnetic Resonance Imaging*. Mosby, second edition, 2001. pages 20-22.

[23] P. T. Callaghan. *Principles of Nuclear Magnetic Resonance Microscopy*. Oxford University Press, 1993.

[24] Stejskal E. O. and Tanner T. E. Spin diffusion measurements: spin echoes in the presence of a time-dependent field gradient. *The Journal of Chemical Physics*, 42:288–292, 1965.

[25] A. Einstein. Über die von der molekularkinetischen theorie der wärme gefordete bewegung von in ruhenden flüssigkeiten suspendierten teilchen. *Ann Physik*, 4:549–590, 1905.

[26] D. Le Bihan, E. Breton, D. Lallemand, P. Grenier, E. Cabanis, and M. Laval-Jeantet. MR imaging of intravoxel incoherent motions: application to diffusion and perfusion in neurologic disorders. *Radiology*, 161:401–407, 1986.

[27] W. S. Price. Pulsed-gradient nuclear magnetic resonance as a tool for studying translational diffusion: Part 1. basic theory. *Magnetic Resonance in Medicine*, 9:299–336, 1997.

[28] C. H. Neuman. Spin echo of spins diffusion in a bounded medium. *Journal of Chemical Physics*, 60:4508–4511, 1974.

[29] S. L. Codd and P. T. Callaghan. Spin echo analysis of restricted diffusion under generalized gradient waveforms: Planar, cylindrical, and spherical pores with wall relaxivity. *Journal of Magnetic Resonance*, 137:358–372, 1999.

[30] S. Pajevic and C. Pierpaoli. Color schemes to represent the orientation of anisotropic tissues from diffusion tensor data: Application to white matter fiber tract mapping in the human brain. *Magnetic Resonance in Medicine*, 42:526–540, 1999.

[31] Z. Wang, B. C. Vemuri, Y. Chen, and T. Mareci. A constrained variational principle for direct estimation and smoothing of the diffusion tensor field from DWI. In *Proc. of 18th International Conference on Information Processing in Medical Imaging*, volume 2732 of *Lecture Notes in Computer Science*, pages 660–671, Ambleside, 2003. Springer–Verlag.

[32] D. C. Alexander. An introduction to computational diffusion MRI: the diffusion tensor and beyond. In J. Weichert and H. Hagen, editors, *Visualization and Image Processing of Tensor Fields*. Springer, 2005.

[33] D. K. Jones, M. A. Horsfield, and A Simmons. Optimal strategies for measuring diffusion in anisotropic systems by magnetic resonance imaging. *Magnetic Resonance in Medicine*, 42:515–525, 1999.

[34] G. J. M. Parker and D. C. Alexander. Probabilistic monte carlo based mapping of cerebral connections utilising crossing fibre information. In *Proc. 11th Annual Meeting of the ISMRM*, page 2162, Toronto, 2003.

[35] T. E. J. Behrens, H. Johansen-Berg, W. M. Woolrich, S. M. Smith, C. A. M. Wheeler-Kingshott, P. A. Boulby, G. J. Barker, E. L. Sillery, O. Ciccarelli, A. J. Thompson, J. M. Brady, and P. M. Matthews. Non-invasive mapping of connections between human thalamus and cortex using diffusion imaging. *Nature Neuroscience*, 6:750–757, 2003.

[36] P. A. Cook, D. C. Alexander, and G. J. M. Parker. Modelling noise-induced fibre-orientation error in diffusion tensor MRI. In *Proc. IEEE International Symposium on Biomedical Imaging*, pages 332–336, Arlington, 2004.

[37] P. J. Basser, S. Pajevic, C. Pierpaoli, J. Duda, and A. Aldroubi. In vivo fiber tractography using DT-MRI data. *Magnetic Resonance in Medicine*, 44:625–632, 2000.

[38] S. Mori, B. J. Crain, V. P. Chacko, and P. C. M Van Zijl. Three-dimensional tracking of axonal projections in the brain by magnetic resonance imaging. *Annals of Neurology*, 45:265–269, 1999.

[39] D. M. Weinstein, G. L. Kindlmann, and E. C. Lundberg. Tensorlines: advection-diffusion based propagation through diffusion tensor fields. pages 249–253, San Francisco, 1999.

[40] G. J. M. Parker, H. A. Haroon, and C. A. M. Wheeler-Kingshott. A framework for a streamline-based probabilistic index of connectivity (PICo) using a structural interpretation of MRI diffusion measurements. *Journal of Magnetic Resonance Imaging*, 18:242–254, 2003.

[41] M. Lazar and A. L. Alexander. White matter tractography using random vector (RAVE) perturbation. In *Proc. 10th Annual Meeting of the ISMRM*, page 523, Hawai'i, 2002.

[42] L.-W. Koch, V. J. Weeden, J.-C. Weng, T. G. Reese, J.-H. Chen, and W. T. I. Tseng. An investigation of functional and anatomical connectivity using magnetic resonance imaging. *NeuroImage*, 16:241–250, 2002.

[43] G. J. M. Parker and D. C. Alexander. Probabilistic monte-carlo based mapping of

cerebral connections utilizing whole-brain crossing fibre information. In *Proc. Image Processing in Medical Imaging*, pages 684–695, 2003.

[44] K. V. Mardia and P. E. Jupp. *Directional Statistics*. Wiley, 2000.

[45] D. K. Jones and C. Pierpaoli. Confidence mapping in diffusion tensor magnetic resonance imaging tractography using a bootstrap approach. *Magnetic Resonance in Medicine*, 53:1143–1149, 2005.

[46] D. K. Jones. Tractography gone wild: Probabilistic tracking using the wild bootstrap. In *Proc. 14th Annual Meeting of the ISMRM*, page 435, Seattle, 2006.

[47] M. Lazar and A. L. Alexander. Bootstrap white matter tractography (boot-trac). *NeuroImage*, 24:524–532, 2005.

[48] H. A. Haroon and G. J. M. Parker. Using the wild bootstrap to quantify uncertainty in fibre orientations from Q-Ball analysis. In *Proc. Joint Annual Meeting ISMRM-ESMRMB*, page 903, Berlin, 2007.

[49] B. Whitcher, D. S. Tuch, and L. Wang. The wild bootstrap to quantify variability in Diffusion Tensor MRI. In *Proc. 13th Annual Meeting of the ISMRM*, page 1335, Florida, 2005.

[50] T. E. J. Behrens, M. W. Woolrich, M. Jenkinson, H. Johansen-Berg, R. G. Nunes, S. Clare, P. M. Matthews, J. M. Brady, and S. M. Smith. Characterization and propagation of uncertainty in diffusion-weighted MR imaging. *Magnetic Resonance in Medicine*, 50:1077–1088, 2003.

[51] T. Hosey, G. Williams, and R. Ansorge. Inference of multiple fiber orientations in high angular resolution diffusion imaging. *Magnetic Resonance in Medicine*, 54:1480–1489, 2005.

[52] O. Friman and C-F Westin. Uncertainty in fiber tractography. Volume 3749 of Lecture Notes in Computer Science, pages 107–114. Edited by James S. Duncan and Guido Gerig. Springer, 2005.

[53] D. K. Jones. Gaussian modelling of the diffusion signal. In H. Johansen-Berg and T. E. J. Behrens, editors, *Diffusion MRI: from quantitative measurement to in vivo neuroanatomy*, pages 37–54. Academic Press, 2009.

[54] L. R. Frank. Characterization of anisotropy in high angular resolution diffusion-weighted MRI. *Magnetic Resonance in Medicine*, 47:1083–1099, 2002.

[55] D. C. Alexander, G. J. Barker, and S. R. Arridge. Detection and modeling of non-Gaussian apparent diffusion coefficient profiles in human brain data. *Magnetic Resonance in Medicine*, 48:331–340, 2002.

[56] Y. Chen, W. Guo, Q. Zeng, G. He, B. C. Vemuri, and W. Liu. Recovery of intra-voxel structure from HARD DWI. In *Proc. IEEE International Symposium on Biomedical Imaging*, pages 1028–1031, Arlington, 2004. IEEE.

[57] D. C. Alexander and G. J. Barker. Optimal imaging parameters for fibre-orientation estimation in diffusion MRI. *NeuroImage*, 27:357–367, 2005.

[58] D. S. Tuch, T. G. Reese, M. R. Wiegell, N. Makris, J. W. Belliveau, and V. J. Wedeen. High angular resolution diffusion imaging reveals intravoxel white matter fiber heterogeneity. *Magnetic Resonance in Medicine*, 48:577–582, 2002.

[59] O. Pasternak, N. Sochen, and Y. Assaf. PDE based estimation and regularization of multiple diffusion tensor fields. In J. Weickert and H. Hagen, editors, *Visualization and Image Processing of Tensor Fields*. Springer, 2005.

[60] E. Kaden, T. R. Knosche, and A. Anwander. Parametric spherical deconvolution: Inferring anatomical connectivity using diffusion MR imaging. *NeuroImage*, 37:474–488, 2007.

[61] Y. Assaf, R. Z. Freidlin, G. K. Rohde, and P. J. Basser. New modelling and experimental framework to characterize hindered and restricted water diffusion in brain white matter. *Magnetic Resonance in Medicine*, 52:965–978, 2004.

[62] C. H. Neuman. Spin echo of spins diffusion in a bounded medium. *Journal of Chemical Physics*, 60:4508–4511, 1974.

[63] V. J. Wedeen, T. G. Reese, D. S. Tuch, J.-G. Dou, R. M. Weiskoff, and D. Chessler. Mapping fiber orientation spectra in cerebral white matter with Fourier-transform diffusion MRI. In *Proc. 7th Annual Meeting of the ISMRM*, page 321, Philadelphia, 1999. Berkeley, USA: ISMRM.

[64] D. S. Tuch. *Diffusion MRI of complex tissue structure*. Doctor of Philosophy in Biomedical Imaging at the Massachusetts Institute of Technology, 2002.

[65] J. Pipe. Pulse sequences for diffusion-weighted mri. In H. Johansen-Berg and T. E. J. Behrens, editors, *Diffusion MRI: from quantitative measurement to in vivo neuroanatomy*, pages 11–36. Academic Press, 2009.

[66] L-W. Kuo, J-H. Chen, V. J. Weeden, and W-Y. I. Tseng. Optimization of diffusion spectrum imaging and q-ball imaging on clinical MRI system. *NeuroImage*, 41:7–18, 2008.

[67] D. S. Tuch. Q-Ball Imaging. *Magnetic Resonance in Medicine*, 52:1358–1372, 2004.

[68] D. S. Tuch, T. G. Reese, M. R. Wiegell, and V. J. Wedeen. Diffusion MRI of complex neural architecture. *Neuron*, 40:885–895, 2003.

[69] D. C. Alexander. Multiple-fibre reconstruction algorithms for diffusion MRI. *Annals of the New York Academy of Sciences*, 1046:113–133, 2005.

[70] C. P. Hess, P. Mukherjee, E. T. Han, D. Xu, and D. B. Vigneron. A spherical harmonic approach to q-ball imaging. In *Proc. 13th Annual Meeting of the ISMRM*, page 389, Florida, 2005.

[71] M. Descoteaux, E. Angelino, S. Fitzgibbons, and R. Deriche. Regularized, fast and robust analytical Q-Ball Imaging. *Magnetic Resonance in Medicine*, 58:497–510, 2007.

[72] A. W. Anderson. Measurement of fiber orientation distributions using high angular resolution diffusion imaging. *Magnetic Resonance in Medicine*, 54:1194–1206, 2005.

[73] E. Özarslan, T. M. Shepherd, B. C. Vemuri, S. J. Blackband, and T. H. Mareci. Resolution of complex tissue microarchitecture using the diffusion orientation transform (DOT). *NeuroImage*, 31:1086–1103, 2006.

[74] J-D. Tournier, C-H. Yeh, F. Calamante, and K-H. Cho. Resolving crossing fibres using constrained spherical deconvolution: Validation using diffusion-weighted imaging phantom data. *NeuroImage*, 42:617–625, 2008.

[75] C. P. Lin, W. Y. I. Tseng, L. Kuo, V. J. Wedeen, and J. H. Chen. Mapping orientation distribution function with spherical encoding. In *Proc. 11th Annual Meeting of the ISMRM*, page 2120, Toronto, 2003. Berkeley, USA: ISMRM.

[76] A. Anderson and Z. Ding. Sub-voxel measurement of fiber orientation using high angular resolution diffusion tensor imaging. In *Proc. 10th Annual Meeting of the ISMRM*, page 440, Honolulu, 2002. Berkeley, USA: ISMRM.

[77] J.-D. Tournier, F. Calamante, D. G. Gadian, and A. Connelly. Direct estimation of the fiber orientation density function from diffusion-weighted MRI data using spherical deconvolution. *NeuroImage*, 23:1176–1185, 2004.

[78] J.-D. Tournier, F. Calamante, and A. Connelly. Robust determination of the fibre orientation distribution in diffusion MRI: Non-negativity constrained super-resolved spherical deconvolution. *NeuroImage*, 35:1459–1472, 2007.

[79] P. C. Hansen. Regularization tools; a MATLAB package for analysis and solution of ill-posed problems. volume 6, pages 1–35, 1994.

[80] H-K. Jeong and A. W. Anderson. Measurement of intrinsic fiber diffusivity using spherical deconvolution of high angular diffusion MRI data. In *Proc. 15th Annual Meeting of the ISMRM*, page 905, Berlin, 2007.

[81] K. E. Sakaie. How fast can PAS go? In *Proc. 13th Annual Meeting of the ISMRM*, page 3323, Toronto, 2008.

[82] L. Bloy and R. Verma. On computing the underlying fiber directions from the diffusion orientation distribution function. In *Proc. Medical Image Computing and Computer-Assisted Intervention*, New York, 2008.

[83] P. A. Cook, Y. Bai, S. Nedjati-Gilani, K. K. Seunarine, M. G. Hall, G. J. Parker, and D. C. Alexander. Camino: Open-source diffusion-MRI reconstruction and processing. In *Proc. 14th Annual Meeting of the ISMRM*, Berlin, 2006.

[84] G. J. Stanisz, A. Szafer, G. A. Wright, and R. M. HenkelMan. An analytical model of restricted diffusion in bovine optic nerve. *Magnetic Resonance in Medicine*, 37:103–111, 1997.

[85] G. J. Stanisz and R. M. HenkelMan. Diffusion anisotropy of t_2 components in bovine optic nerve. *Magnetic Resonance in Medicine*, 40:405–410, 1998.

[86] J. C. Ford and D.B. Hackney. Numerical model for calculation of apparent diffusion coefficients (ADC) in permeable cylinders comparison with measured ADC in spinal cord white matter. *Magnetic Resonance in Medicine*, 37:387–394, 1997.

[87] M. G. Hall and D. C. Alexander. Finite pulse widths improve fibre orientation estimates in diffusion mri. In *Proc. 13th Annual Meeting of the ISMRM*, Seattle, 2006.

[88] A. Szafer, J. Zhong, and J. C. Gore. Theoretical model for water diffusion in tissues. *Magnetic Resonance in Medicine*, 33:697–712, 1995.

[89] D. K. Jones. Determining and visualizing uncertainty in estimates of fiber orientation from diffusion tensor mri. *Magnetic Resonance in Medicine*, 49:7–12, 2003.

[90] W. H. Press, S. A. Teukolsky, W. T. Vettering, and B. P. Flannery. *Numerical Recipes in C*. New York, USA: Press Syndicate of the University of Cambridge, 1988.

[91] J.-D. Tournier, F. Calamante, and A. Connelly. Multiple fibre orientations estimated by spherical deconvolution: Assessment of precision using the ‘bootstrap’ method. In *13th Annual Meeting of the ISMRM*, page 223, Florida, 2005.

[92] B. Effron and R. Tibshirani. *An introduction to the bootstrap*. Chapman & Hall, 1993.

[93] A.C. Davison and D.V. Hinkley. *Bootstrap Methods and their Application*. Cambridge University Press, 1997.

[94] J.-D. Tournier, F. Calamante, and A. Connelly. Improved characterisation of crossing fibres: Optimization of spherical deconvolution using a minimum entropy principle. In *Proc. 13th Annual Meeting of the ISMRM*, page 384, Florida, 2005.

[95] J.-D. Tournier, F. Calamante, and A. Connelly. Improved characterisation of crossing fibres: spherical deconvolution combined with tikhonov regularization. In *Proc. 14th Annual Meeting of the ISMRM*, Seattle, 2006.

[96] J.-D. Tournier, F. Calamante, and A. Connelly. Resolving crossing fibres using constrained spherical deconvolution: validation using DWI phantom data. In *Proc. 15th Annual Meeting of the ISMRM*, page 902, Berlin, 2007.

[97] F. Dell'Acqua, G. Rizzo, P. Scifo, R. A. Clarke, G. Scotti, S. Cerutti, and F. Fazio. A deconvolution approach based on multi-tensor model to solve fiber crossing in diffusion-MRI. In *Proc. 27th Annual Conference of IEEE Engineering in Medicine and Biology*, pages 1415–1418, Shanghai, 2005.

[98] K. E. Sakaie and M. J. Lowe. An objective method for regularization of fiber orientation distributions derived from diffusion-weighted MRI. *NeuroImage*, 34:169–176, 2007.

[99] D. C. Alexander. A comparison of q-ball and PASMRI on sparse diffusion MRI data. In *Proc. 12th Annual Meeting of the ISMRM*, page 90, Kyoto, 2004.

[100] L-W. Kuo, V. J. Weeden, J-C. Weng, T. G. Reese, J-H. Chen, and W-Y. I. Tseng. Using track similarity to determine optimum sequence parameters for diffusion spectrum imaging. In *Proc. 13th Annual Meeting of the ISMRM*, page 39, Florida, 2005.

[101] E. Özarslan, B. C. Vemuri, and T. H. Mareci. Fiber orientation mapping using generalized diffusion tensor imaging. In *Proc. IEEE International Symposium on Biomedical Imaging*, pages 1036–1038, Arlington, 2004. IEEE.

[102] C. Liu, R. Bammer, B. Acar, and M. E. Moseley. Characterizing non-gaussian diffusion by using generalized diffusion tensor. *Magnetic Resonance in Medicine*, 51:924–937, 2004.

[103] R. Blyth, P. A. Cook, and D. C. Alexander. Tractography with multiple fibre orientations. In *Proc. 11th Annual Meeting of the ISMRM*, page 240, Toronto, 2003. Berkeley, USA: ISMRM.

[104] P Hagmann, M. Kurant, X. Gigandet, P. Thiran, V. J. Wedeen, R. Meuli, and Thiran J.-P. Mapping human whole-brain structural networks with diffusion MRI. *PLoS ONE*, 2(7):e597, 2007.

[105] M. Perrin, C. Poupon, Y. Cointepas, B. Rieul, N. Golestani, C. Pallier, D. Rivire, A Constantinesco, D. Le Bihan, and J.-F. Mangin. Fiber tracking in q-ball fields using regularized particle trajectories. In *Proc. Information Processing in Medical Imaging*, pages 52–63, Spring Valley, 2005.

[106] P. A. Cook, H. Zhang, B. B. Avants, P. A. Yushkevich, D. C. Alexander, J. C Gee, O. Ciccarelli, and A. J. Thompson. An automated approach to connectivity-based partitioning of brain structures. In *Proc. Medical Image Computing and Computer-Assisted Intervention*, pages 164–171, Palm Springs, 2005.

[107] P. A. Cook and D. C. Alexander. Modelling uncertainty in two fibre-orientation estimates within a voxel. In *Proc. 14th Annual Meeting of the ISMRM*, page 1629, Seattle, 2006.

[108] J. I. Berman, S. Chung, P. Mukherjee, C. P. Hess, E. T. Han, and R. G. Henry. Probabilistic streamline q-ball tractography using the residual bootstrap. *NeuroImage*, 39:215–222, 2008.

[109] M. J. Fonteijn, F. A. J. Verstraten, and D. G. Norris. Probabilistic inference on Q-Ball imaging data. *IEEE Transactions on Medical Imaging*, 26:1515–1524, 2007.

[110] P. Savadjiev, J. S. W. Campbell, M. Descoteaux, R. Deriche, G. B. Pike, and K. Siddiqi. Labelling of ambiguous subvoxel fibre bundle configurations in high angular resolution diffusion MRI. *NeuroImage*, 41:58–68, 2008.

[111] H. Gudbjartsson and S. Patz. The rician distribution of noisy MRI data. *Magnetic Resonance in Medicine*, 34:910–914, 1995.

[112] P. J. Basser and C. Pierpaoli. Microstructural and physiological features of tissues elucidated by quantitative diffusion tensor MRI. *Journal of Magnetic Resonance Series B*, 111:209–19, 1996.

[113] H. Grey. Greys anatomy (figure 684). http://www.bartleby.com/107/187.html.

[114] B. Efron. Bootstrap methods: another look at the jackknife. *Annuals of Statistics*, 1046:113–133, 2005.

[115] E. Fix and J.L. Hodges. Discriminatory analysis, nonparametric discrimination: Consistency properties. Technical Report 4, USAF School of Aviation Medicine, Randolph Field, Texas, 1951.

[116] C. G. Broyden. The convergence of a class of double-rank minimization algorithms. *Journal of the Institute of Mathematics*, 6:76–90, 1970.

[117] R. Fletcher. A new approach to variable metric algorithms. *Computer Journal*, 13:317–322, 1970.

[118] D. Goldfarb. A family of variable metric updates derived by variational means. *Mathematics of Computing*, 24:23–26, 1970.

[119] D. F. Shanno. Conditioning of quasi-newton methods for function minimization. *Mathematics of Computing*, 24:647–656, 1970.

[120] M. A. Fischler and R. C. Bolles. Random sample consensus: A paradigm for model fitting with applications to image analysis and automated cartography. *Communications of the ACM*, 24:381–395, 1981.

[121] M. G. Hall and D. C. Alexander. Convergence and parameter choice for montecarlo simulations of diffusion MRI. *IEEE Transactions in Medical Imaging*, 28:1354–1365, 2009.

[122] M. Descoteaux. *High angular resolution diffusion MRI: from local estimation to segmentation and tractography*. PhD thesis, INRIA Sophia Antipolis, 2008.